Helsinki University of Technology Control Engineering Laboratory

Espoo 2004 Report 143

MODELLING AND EVALUATION OF VALVE-REGULATED LEAD-ACID BATTERIES

Ander Tenno

TEKNILLINEN KORKEAKOULU
TEKNISKA HÖGSKOLAN
HELSINKI UNIVERSITY OF TECHNOLOGY
TECHNISCHE UNIVERSITÄT HELSINKI
UNIVERSITE DE TECHNOLOGIE D´HELSINKI

Helsinki University of Technology Control Engineering Laboratory

Espoo September 2004 Report 143

MODELLING AND EVALUATION OF VALVE-REGULATED LEAD-ACID BATTERIES

Ander Tenno

Dissertation for the degree of Doctor of Science in Technology to be presented with due permission of the Department of Automation and Systems Technology, for public examination and debate in Auditorium AS1 at Helsinki University of Technology (Espoo, Finland) on the 3rd of December, 2004, at 12 noon.

Helsinki University of Technology

Department of Automation and Systems Technology

Control Engineering Laboratory

Distribution:
Helsinki University of Technology
Control Engineering Laboratory
P.O. Box 5500
FIN-02015 HUT, Finland
Tel. +358-9-451 5201
Fax. +358-9-451 5208
E-mail: control.engineering@hut.fi
http://www.control.hut.fi/

ISBN 951-22-7325-X (printed)
ISBN 951-22-7326-8 (pdf)
ISSN 0356-0872

Picaset Oy
Helsinki 2004

Available on net at http://lib.hut.fi/Diss/2004/isbn9512273268

HELSINKI UNIVERSITY OF TECHNOLOGY P.O. BOX 1000, FIN-02015 HUT http://www.hut.fi	ABSTRACT OF DOCTORAL DISSERTATION

Author Ander Tenno

Name of the dissertation

Modelling and Evaluation of Valve-Regulated Lead-Acid Batteries

Date of manuscript September 20, 2004	Date of the dissertation December 3, 2004
☐ Monograph	☑ Article dissertation (summary + original articles)

Department	Automation and Systems Technology
Laboratory	Control Engineering Laboratory
Field of research	Control Engineering
Opponent(s)	PhD Eckhard Karden
Supervisor (Instructor)	Prof. Teuvo Suntio, Tampere University of Technology

Abstract

The thesis deals with modelling of valve-regulated lead-acid (VRLA) batteries to answer the two biggest questions of 'will they work' and 'when will they need to be replaced' without resorting to full discharge. Despite the strong efforts undertaken by numerous researchers in search of simple and reliable indicators of the state-of-health (SOH) of a battery they were never found. Originally, it was expected that resistance, conductance and impedance measurements could be such indicators, but they have turned out to be unreliable.

This dissertation attempts to solve the problem by proposing a complex approach utilising fast calculation model for electrochemical processes to predict the behaviour of VRLA batteries under charge-discharge conditions and applying this model to a fast analysis of backup batteries in uninterruptible power supply (UPS) systems and detection of weak batteries in telecommunication networks.

This model can predict the behaviour of VRLA batteries in full range of charge-discharge processes, including deep discharge and overcharge of batteries, using direct current, voltage and temperature measurements. The SOH of batteries can be detected by this method in terms of natural electrochemical processes.

Keywords Batteries, VRLA, lead acid, modelling, identification

UDC	Number of pages 95+85
ISBN (printed) 951-22-7325-X	ISBN (pdf) 951-22-7326-8
ISBN (others)	ISSN 0356-0872

Publisher Helsinki University of Technology, Control Engineering Laboratory

Print distribution Helsinki University of Technology, Control Engineering Laboratory

☑ The dissertation can be read at http://lib.hut.fi/Diss/

Preface

This work originally started at the Control Engineering Laboratory of Helsinki University of Technology, in a TEKES-funded project focusing on optimal use and monitoring of batteries, back in 1999. Since the beginning of 2001 I have carried out my studies, still at Control Engineering Laboratory, with the help of the Graduate School in Electronics, Telecommunications, and Automation (GETA).

The results reported here would not have been achieved without the support of many people. The author wishes to thank Prof. Teuvo Suntio from Tampere University of Technology, and Prof. Heikki Koivo and Dr. Sc. Robert Tenno from Helsinki University of Technology. Without their support, in various forms, the problems encountered during the process of writing this dissertation might never have been solved.

I am also grateful to Mr. Pekka Waltari from ABB Oy for providing the experimental data used when developing and verifying the models.

Espoo, September 2004
Ander Tenno

List of Publications

This thesis consists of an introductory part and the following publications.

[P1] A. Tenno, R. Tenno and T. Suntio. Charge-discharge behaviour of VRLA batteries: Model calibration and application in state estimation and failure detection. *J. Power Sources*, vol. 103, 2001, pp. 42-53.

[P2] A. Tenno, R. Tenno and T. Suntio. Soft-sensor approach in characterization of VRLA batteries. in *Proc. 23rd INTELEC Conf.*, 2001, pp. 554-562.

[P3] A. Tenno. Software for evaluation of VRLA batteries. in *Proc. EuroPES 2002*, 2002, pp. 461-466.

[P4] A. Tenno, R. Tenno and T. Suntio. Fast model for monitoring of backup batteries in telecommunications networks. in *Proc. PES 2002*, 2002, pp. 458-463.

[P5] A. Tenno, R. Tenno and T. Suntio. Battery impedance and its relation to battery characteristics. in *Proc. 24th INTELEC Conf.*, 2002, pp. 176-183.

[P6] A. Tenno, R. Tenno and T. Suntio. Evaluation of VRLA batteries under overcharging: Model for battery testing. *J. Power Sources*, vol. 111, 2002, pp. 65-82.

[P7] T. Suntio, A. Tenno and R. Tenno. Impedance characterization of VRLA batteries. in *Proc. 9th Power Quality Conf.*, 2003, pp. 325-330.

[P8] A. Tenno, R. Tenno and T. Suntio. Method for battery impedance analysis. *J. Electrochem. Soc.*, vol. 151, no 6, 2004, pp. A806-A824.

Nomenclature

Symbols

A - active surface area per unit volume of porous electrode, cm^2/cm^3,
A_M - active surface area for primary reaction, cm^2/cm^3,
A_{O2} - active surface area for oxygen reaction, cm^2/cm^3,
A_{H2} - active surface area for hydrogen reaction, cm^2/cm^3,
A_{max} - maximum active surface area, cm^2/cm^3,
a_n - power series coefficients in the battery ohmic resistance model, sec^{-n},
C_e - electrode capacitance, F,
C_1 - double-layer capacitance of positive electrode, F,
C_2 - double-layer capacitance of negative electrode, F,
C/I - discharge rate, h,
c - acid concentration, mol/cm^3,
c_{ref} - reference initial concentration, mol/cm^3,
c_{dl} - double-layer specific capacitance, F/cm^3,
c_{Pb2} - concentration of lead ions, mol/cm^3,
c_{Pb2}^* - saturation constant of lead ions, mol/cm^3,
D - electrolyte diffusion constant, cm^2/s,
D^{eff} - diffusion in porous electrode, cm^2/s,
E_A - activation energy, kJ/mole,
F - Faraday's constant, 96,487 C/mol,
F - Fourier transform (operator),
f - molar activity coefficient, no unit,
h - thickness of porous electrode, cm,
I_{app} - applied current, A,
$I_{ap.0}$ - amplitude of current pulse, A,
I_{PbSO4} - limit current density for cathodic reaction, A/cm^2,
i - current density in electrolyte, A/cm^2,
i_M - current density generated by primary reaction, A/cm^2,
i_{O2} - current density generated by oxygen reaction A/cm^2,
i_{H2} - current density generated by hydrogen reaction, A/cm^2,
i_k - current density generated by grid corrosion reaction, A/cm^2,
i_0^M - exchange current density for primary reaction, A/cm^2,
i_0^{O2} - exchange current density for oxygen reaction A/cm^2,
i_0^{H2} - exchange current density for hydrogen reaction, A/cm^2,
i_0^k - exchange current density for grid corrosion reaction, A/cm^2,
i_l - current density in electrolyte, A/cm^2,
i_s - current density in solid matrix of electrode, A/cm^2,
i_{app} - applied current density, A/cm^2,
i_0 - exchange current density, A/cm^2,

j - transfer current density, A/cm^3; also imaginary unit in Chapter VI,
j_M - transfer current density for primary reaction, A/cm^2,
j_{O2} - transfer current density for oxygen reaction A/cm^2,
j_{H2} - transfer current density for hydrogen reaction, A/cm^2,
K_1 - equivalent volume to charge constant, cm^3/C,
K_2 - equivalent molarity to charge constant, mol/C,
K_3 - equivalent molarity to charge absolute constant, mol/C,
k - constant: 1/k - temperature voltage, V,
k_{ore} - oxygen recombination efficiency, no unit,
k_{PbSO4} - mass-transfer coefficient for lead ions, cm/s,
M - molecular weight of species: Pb, PbO_2, $PbSO_4$, g/mol,
n_{O2} - number of moles of oxygen generated n_{O2}^{evl} or reduced n_{O2}^{rec} on electrode, mol,
n_{H2}^{evl} - number of moles of hydrogen generated on negative electrode, mol,
n_{O2}^{g} - number of oxygen gas moles accumulated in free space of battery, mol,
n_{H2}^{g} - number of hydrogen gas moles accumulated in free space of battery, mol,
n_{H2O} - number of water moles, mol,
p_{O2} - oxygen partial pressure, Pa,
p_{H2} - hydrogen partial pressure, Pa,
p_{O2}^{ref} - reference partial pressure of oxygen, Pa,
p_{H2}^{ref} - reference partial pressure of hydrogen, Pa,
Q_0 - oxygen flow velocity through separator, cm/s,
Q_{max} - theoretical (reference) capacity of electrode, C/cm^3,
R - universal gas constant, 8.3145 J/mol-K,
R_0 - conducting elements resistance, Ω,
R_1 - charge-transfer resistance of positive electrode, Ω,
R_2 - charge-transfer resistance of negative electrode, Ω,
R_{ct} - charge-transfer resistance of single electrode, Ω,
r_{ct} - charge-transfer local resistance, Ωcm^3,
r_0 - conducting elements local resistance, Ωcm^3,
S_p - plate area, cm^2,
T - temperature, K,
T_0 - standard temperature, 298.2^o K (25^o C), also forecast period in in Chapter VI, sec,
t - elapsed time, sec,
t_0 - initial moment, sec,
t^o_+ - transference number, no unit,
U - thermodynamic equilibrium potential for primary reaction, V,
U_{O2} - thermodynamic equilibrium potential for oxygen reaction V,
U_{H2} - thermodynamic equilibrium potential for hydrogen reaction, V,
V_o - partial molar volume of acid in electrolyte, cm^3/mol,
V_e - partial molar volume of water in electrolyte, cm^3/mol,
w - applied volumetric current density, A/cm^3,
w_M - primary reaction volumetric current density, A/cm^3,
w_{byp} - capacitive volumetric current density, A/cm^3,
x - depth of porous electrode, cm,
Z - overall battery impedance, Ω,
Z_{AC} - double-layer impedance, Ω,
Z_{EC} - electrochemical impedance, Ω,

Greek Symbols

α_a - anodic apparent transfer coefficient for primary reaction, no unit,
α_c - cathodic apparent transfer coefficient for primary reaction, no unit,
α_{O2} - apparent transfer coefficient for oxygen reaction, no unit,
α_{H2} - apparent transfer coefficient for hydrogen reaction, no unit,
α_k - apparent transfer coefficient for grid corrosion reaction, no unit,
α_{Ah} - charging efficiency, no unit,
β - tortuosity exponent, no unit,
ε - porosity of electrode, fraction of electrode saturated with acid, no unit,
η - surface overpotential for primary reaction, V,
η_{O2} - surface overpotential for oxygen reaction V,
η_{H2} - surface overpotential for hydrogen reaction, V,
θ - state of charge, no unit,
κ - acid conductivity, S/cm,
κ^{eff} - conductivity of porous electrodes or separator, S/cm,
μ - dimensionless acid concentration, no unit,
ρ - electrode morphology coefficients, no unit,
ρ - density of species (index): Pb, PbO_2 or $PbSO_4$, g/cm^3,
σ^{eff} - conductivity of porous electrode, S/cm,
σ - conductivity of bulk electrode: Pb or PbO_2, S/cm,
ϕ^s - solid matrix potential, V,
ϕ^l - electrolyte potential, V,
ω - angular velocity, rad/s.

Abbreviations

AGM	Absorbent Glass Mat
ORE	Oxygen Recombination Efficiency
SOC	State-Of-Charge
SOH	State-Of-Health
UPS	Uninterruptible Power Supply
VPC	Voltage Per Cell
VRLA	Valve-Regulated Lead-Acid
SHE	Standard Hydrogen Electrode

Table of Contents

List of Figures

Chapter I

1. Introduction

1.1. Battery Failure Problem

The blackouts of 2003 in the eastern parts of the United States and Canada as well as in the areas of Europe including major cities like London and Helsinki forced the citizens and businesses of those areas to face the consequences of interrupted energy supply in daily life. Even if the nationwide grid systems are built using several levels of redundancy, a disaster may take place. On a smaller scale, the crucial services and emergency control systems such as telecommunications, intensive care in hospitals, data communications in banks, etc, are commonly secured using uninterruptible power supply (UPS) systems. The uninterruptibility of the energy flow in the UPS systems is most often secured using lead acid storage batteries [56], [57], which are automatically connected to supply energy in the case of interruption in the main energy source.

Since late 1980s the valve-regulated lead-acid (VRLA) batteries have gradually replaced their flooded counterparts in most of the applications. The VRLA batteries were originally marketed as maintenance free batteries suitable for installations in uncontrolled environmental conditions, subjecting the batteries to elevated ambient temperatures and no monitoring. It turned out later that the expected life of the VRLA batteries was far inferior to the expected life of the flooded cells, causing deep disappointments among the users of these items [20], [60]. As a consequence, the batteries have to be replaced significantly earlier than their rated life would otherwise necessitate. In addition to the early replacement, the batteries have to be monitored or supervised in order to ensure even a satisfactory integrity of the UPS system. The supervising may be accomplished either manually or using electronic equipment tailored for the particular use. Naturally, the required cost savings necessitate the use of automatic supervisory equipment if available.

The only way to fully check the actual state-of-health (SOH) and state-of-charge (SOC) of a battery is a full capacity test where the battery is disconnected from the system and connected to load providing the discharge current stated by its nominal capacity. The full capacity test causes extra costs, requires skilled staff, can endanger the system integrity, etc. Therefore, other methods, preferably based on non-intrusive test techniques, have been searched for years [60]. When the flooded batteries were in use, the float charge voltage reliably reflected the SOH of the individual cells. Unfortunately, this is not true in VRLA batteries due to naturally high voltage scattering [14]. In mid 1990s, impedance-based methods started gaining attraction, in which ei-

ther a current or voltage signal is injected into a cell or a group of cells and the response is measured. Based on injection and the corresponding response, the battery impedance or conductance may be extracted [18], [26], [27]. The high scattering of readings [38], especially in the region of SOC that is most important from the user's point of view (i.e., 80 - 100 %), can make the impedance method almost useless in practical applications, where the typical number of six-cell blocks is four. Therefore, the SOH or SOC of the individual blocks is difficult or even impossible to determine using the impedance based measuring equipment available. The reason for this may be due to the used excitation frequencies that are too high to measure anything but the dynamics of the double layer capacitor in the negative electrode. Consequently, the readings are small, and prone to variations in measurement practices.

1.2. Model-based Approach

As stated earlier, the only reliable method for assessing the SOH and SOC of a battery is a full capacity test. Based on these measurements, the trends in the battery behaviour may be deduced using the history.

The approach taken in this thesis is to develop a monitoring model, which is adjusted to the behaviour of the actual battery based on the measured cell or block voltage, the current flowing through it and its ambient temperature. The measurements may be taken from a short discharge and subsequent recharge. After the model is calibrated, the battery voltage may be predicted accurately for any load level or load profiles in a similar way to a full capacity test, only this time *simulating* the full discharge. The best accuracy is obtained if the data used for the calibration is a full discharge cycle but the naturally occurring short duration discharge and subsequent recharge can usually give satisfactory accuracy as well.

The modelling approach is based on the previously presented works of other researchers as explained in Section 1.5. The fast calculation model and the use of feedback control make the approach unique in giving fairly accurate predictions of the internal processes as well as enabling the automatic processing of the model calibration and predictions in a reasonable time.

The possible application of the developed method in telecom usage is sketched in Fig. 1.1. The monitoring system reads the recorded data from the base stations e.g. once a month, and predicts the SOH and SOC of the associated batteries against the actual load or using some other predefined load profiles. If violations in respect to the predefined requirements are encountered, a request for replacing the associated battery can be automatically generated. If the recorded data is saved, the trends in the battery behavior may be given or even the future behavior predicted with some accuracy using properly scaled trend information. The number of sites connected to this kind of centralised monitoring system may be large. The monitoring system may be also installed at each site (distributed system), and can predict, for example, the remaining discharge time during the mains outage in addition to the SOH and SOC predictions.

The core elements (i.e., the prototype battery analysis software) of the system shown in Fig. 1.1 already exist (with parts of the technology patented in Finland (FI 114048) and in the United States), and are presented in more detail in Chapters II-IV (models) and Chapter V (software). The rest (i.e., data transfer, automation, hardware, long

term prediction) would need to be designed and implemented, but that has not been the subject of this thesis.

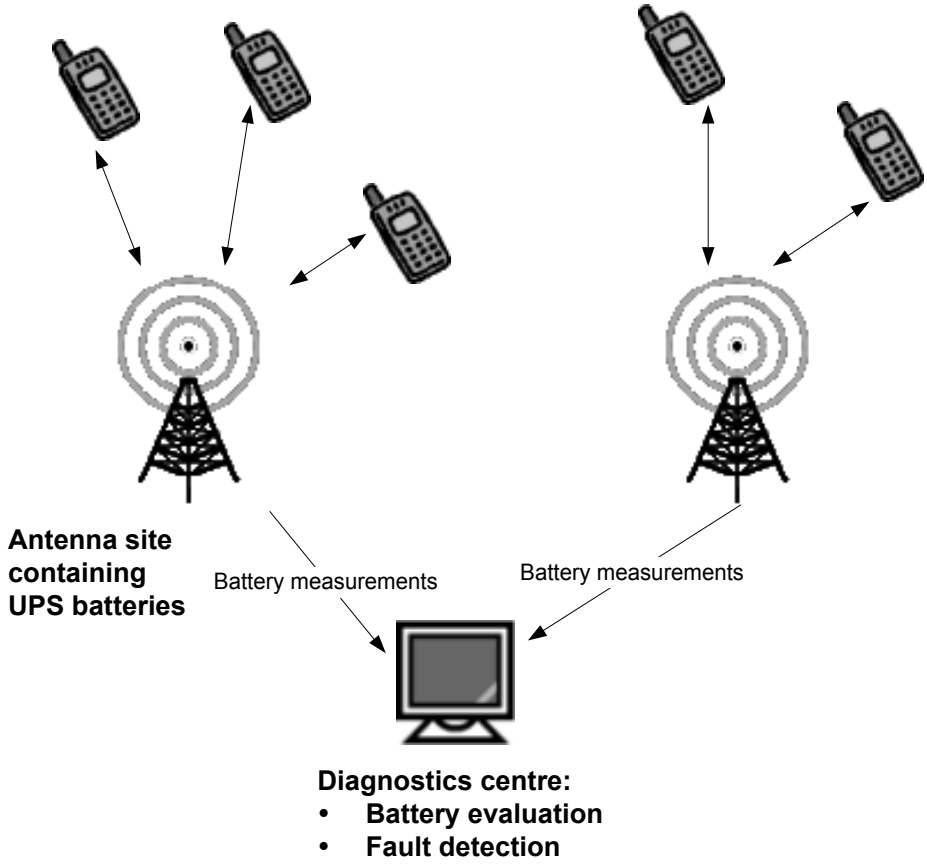

Fig. 1.1. Monitoring of backup batteries. Weak battery for replacement can be detected in time and located in a large telecommunications network.

In addition to the prediction of the battery discharge times, the model presented in this dissertation may be also used for characterisation of the internal functionality of the associated batteries in more detail. These processes (see next section for a list) are usually unobservable without using special electrochemical analysis to visualise them.

1.3. Model Calibration, Fault Detection, and Analysis

Calibration. In battery analysis (Fig. 1.2), the model is calibrated on the basis of measured data (current, voltage, temperature), using the last calibration setup as initial set point for new calibration for every battery. The new model parameters are chosen according to best fit with large sample of measured data.

Fault detection. Battery failure is detected by simulation of the discharge process with respect to expected or measured load (C/I-ratio). The backup time and cut-off voltage are evaluated and compared with the required values. If they exceed them, the battery is considered as suitable for service; otherwise, it is replaced with a new one.

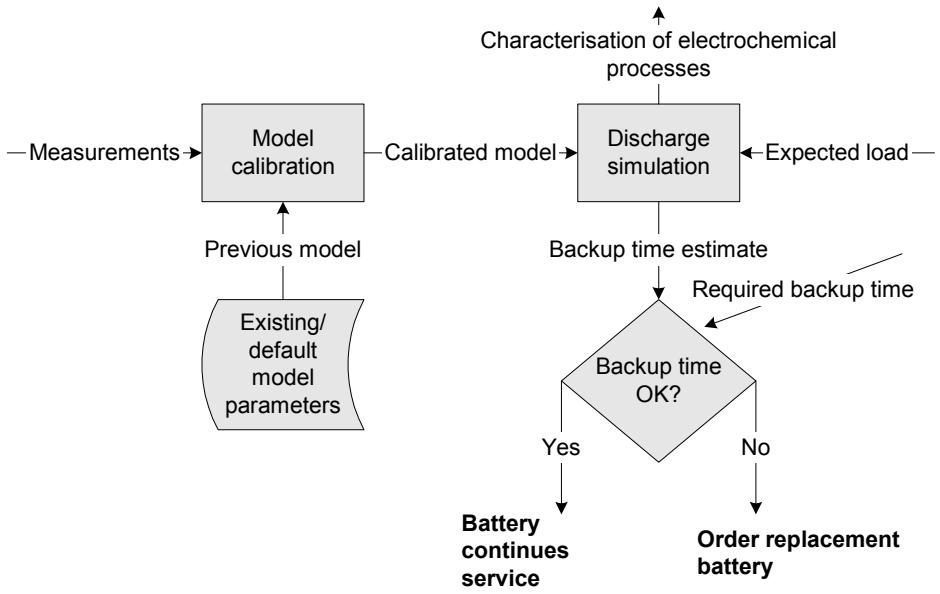

Fig. 1.2. Battery fault detection and diagnostics.

Analysis. The unobservable processes are visualised by the model. The reason for failure is detected by analysis of electrochemical processes in battery electrodes.

Profile in both electrodes can be evaluated for the following characteristics:

- Volumetric reaction rate of main reaction, oxygen and hydrogen reactions
- Acid molarity
- Porosity
- Current density
- Electrolyte potential
- Charge
- Gas current
- Charge-transfer resistance
- Acid conductivity

These processes can be evaluated in a single point per electrode by lumped parameter model, or zoomed in two or more points for some batteries under special interest, using reduced order or low-dimension distributed parameter model for this purpose.

Special characteristics:

- Tafel curve.
- Double-layer impedance and electrochemical impedance on positive and negative electrodes and other frequency response characteristics.

The evolution history can be traced with respect to the last record of measurements for the following processes:

- Current, voltage and capacity
- Open-circuit voltage
- Acid density
- Charge-transfer resistance

- Acid conductivity
- Diffusion rate
- Current share between main reaction and gassing
- Gas escape and water dry-out
- Oxygen and hydrogen reaction rates
- Porosity

1.4. Overview of Dissertation Contents

The main content of the dissertation, explaining how to build a system described in previous section, is presented in Chapters II-V.

Chapter II describes the basic process (main reaction) model and its application for battery state estimation and failure detection. Gassing processes are ignored. Includes experiments.

Chapter III extends the model presented in Chapter II with support for gassing processes and hence supports more accurate deep discharge and overcharge modelling.

Chapter IV explores the usability of impedance modelling for battery evaluation, presenting a way to calculate impedance values from the main model. Both fast double-layer and slow faradic processes are covered.

Chapter V describes the (optimised) calculation algorithms and the modelling software built on the model. This software was used for obtaining all the results presented in this dissertation.

In addition to the above, summary of the publications (with author's contribution outlined) is presented in Chapter VI.

1.5. Used Literature

The approach considered in this dissertation is based on the models developed starting from late 50s by Newman, Tiedemann ([35], [36]) and their successors Gu, Nguyen, White ([13], [22], [23], [24], [37]), Bernardi ([3], [4]) Berndt ([5], [6], [7], [8]), Ekdunge, Simonsson ([15], [16], [55]), and many other battery researchers. Author's contribution to battery modelling and estimation is outlined in the next section. More detailed contribution is given in the beginning of each chapter.

1.6. Author's Contribution

The most significant result of this work is the electrochemical cell model built (and modified) from different models published in literature and the software implementing this model. This model can predict the behaviour of VRLA batteries in full range of charge-discharge processes, including deep discharge and overcharge of batteries, using direct current, voltage and temperature measurements only. The SOH of batteries can be visualised by this method in terms of natural electrochemical processes and impedance spectra that are often unobservable by other means.

The following was carried out:

1. The theoretical cell model screened out from large number of alternative models ([35], [13], [22], [23], [24], [37], [5], [6], [7], [8], etc.) based on calculation and critical analysis is modified for primary processes as follows. A new function is introduced for description of the active surface area: different morphology of porous electrode is introduced, both functionally and in terms of parameters: essentially smaller values for tortuosity exponent is tested to be relevant to VRLA batteries. Charging factor is introduced in the state-of-charge (SOC) model.
2. To improve accuracy and reliability of the models for overcharging, the literature model (proposed by Bernardi, Carpenter [3] and developed by Newman, Tiedemann [36]) is modified with respect to the electrode morphology and charging factor as stated above. In addition, the charging factor is applied in the electrode porosity and acid concentration models. Mass transport of oxygen through separator is modelled as convection. The recombination of oxygen is modelled as a mass-transport limited evolution process.
3. It is stated that the literature model [3], [36] can be simplified when applied to battery testing. The single-step reaction model has the same prediction accuracy as the two-step reaction model (proposed by Ekdunge, Simonsson [15], [16], [55] and applied for overcharging by Newman, Tiedemann [36]). The partial pressure of gases can be eliminated from the electrode reaction equation using preset pressure window for valve.
4. The proposed model is calibrated experimentally on VRLA batteries of two technologies: gel and absorbent glass mat (AGM); it is also calibrated in respect to gas formation processes using experimental data of overcharging.
5. High prediction accuracy of the proposed model is demonstrated in a wide range of charge-discharge processes, including deep discharge and overcharge. It is shown that different behaviour of individual batteries in series during the overcharge can be predicted with higher accuracy than obtained by former authors in [3], [36], [24], [25].
6. The calibrated model is applied to evaluate the unobservable primary and gas formation processes in the test batteries. Oxygen evolution and recombination processes and water dry-out are evaluated during discharge, recharge and overcharge. The model is applied in failure detection to distinguish between seemingly equal batteries with different backup and cut-off time. It is demonstrated that the source for differences is in the electrode morphology (tortuosity exponent) or more likely in the amount of active material of electrodes.
7. Based on the battery model, a method is developed by means of which the battery impedance spectra may be quite accurately predicted at low frequencies. Along with the calibrated model, current, voltage and temperature data is used for impedance analysis. The method allows for analysing both double-layer and faradic processes, visualising the entire spectra including and attempting to distinguish batteries based on impedance. It allows batteries to be modelled at extremely low frequencies, while being free of the limiting assumptions of stationarity of earlier analysis ([14], [26], [27], [41], [42], etc). The method ties together the electrochemical battery model and impedance spectra (this is a new approach), allowing the latter to be interpreted as the non-stationary changing of electrochemical processes. Double-layer impedance is also derived from basic processes.
8. A relatively simple calculation model is proposed for online estimation of the unobservable processes in a battery by float voltage, applied current, and tempera-

ture measurements. The following unobservable processes can be estimated online: current density, potentials, porosity, acid concentration, SOC and gas formation processes. The volumetric reaction rate and other characteristics can be calculated by these parameters, as well as the backup time and cut-off time of a battery. Seemingly similar batteries can be distinguished by calibrated models and source for differences found.

9. Fast calculation algorithm was developed based on model, utilising its structure along with advanced calculation techniques. As a result, the required calculation time was reduced drastically in prototype battery testing software. The calculation speed of one physical second per one hour of battery time (so, for example, modelling of 12-hour process takes just 12 seconds) was achieved for lumped parameter model and one minute per one hour for distributed parameter model. Single battery or several batteries in a string can be analysed with nearly equal speed. This improvement makes application of the theoretical cell model in battery testing practical.
10. Based on the algorithm, modelling software was developed. A good fit was found between data measured in experiment and data predicted by the software for full range of charge-discharge processes including overcharge. High prediction obtained is a strong evidence for applicability of the model and its implementation in software for battery characterization. The software can evaluate unobservable processes like overpotential, reaction rate, porosity, acid concentration and other electrode parameters including impedance spectra from measured float voltage, applied current and temperature of surrounding atmosphere. Also, outwardly equal batteries with different backup time and cut-off time can be distinguished in practice.

Chapter II

2. Basic Process Model and Its Application for State Estimation and Failure Detection

2.1. Introduction

In spite of strong attempt made in study of fast dynamic processes in battery, it was found [30] that the charge-discharge properties and partially service lifetime cannot be predicted with a single parameter like conductivity or impedance. It seemed that fast dynamics of battery contain relatively little information on charge-discharge behaviour. More complex parameters based on physical model should be used to solve the monitoring and failure prediction problems of a battery.

In this chapter, a fast calculation method for prediction of the dynamic behaviour of VRLA batteries under charging-discharging conditions is described. This method is based on (literature) electrochemical cell model and used here for visualising different processes in battery, utilising current, voltage, and temperature measurements. After being calibrated against experimental data, it is applied to detect the original source of differences between seemingly equal batteries. Not all the fine details are included; for those, the reader is referred to [P1].

The method was developed for analysis of backup batteries in telecommunications UPS system. The parameters of prime interest are backup time (when x percent of battery capacity is used up) and cut-off time (time to voltage dropping below predetermined level). The telecommunications UPS system is designed for nominal battery capacity (with some reserve) and if real backup time is lower than the nominal requirement for the UPS system, it is considered as battery failure.

2.2. Contribution

The following contributions are covered in this chapter:

1. The literature cell model is modified slightly. A new function is introduced for description of the active surface area. Different morphology of porous electrode is considered, both functionally and in terms of essentially smaller values for tortuosity exponent.
2. The model is calibrated experimentally for eight VRLA batteries of two technologies: gel and AGM.
3. The calibrated model is applied in failure detection to distinguish between seemingly equal batteries with different backup and cut-off time. The failure source is

demonstrated as differences in the electrode morphology (tortousity exponent) or, more likely, in the amount of active material of electrodes.

4. A relatively simple calculation model is proposed for online estimation of the unobservable processes in battery by float voltage, applied current, and temperature measurements. The following unobservable processes can be estimated online: current density, potential, porosity and acid concentration. The volumetric reaction rate and SOC can be calculated by these parameters, as well as backup time and cut-off time of the battery.

This chapter briefly covers history of lead-acid battery model development, before moving on to describing cell model and calculation method, followed by model calibration and experiments. It should be noted that only main battery reaction is considered. For treatment including oxygen and hydrogen reactions, as well as study of battery behaviour during overcharge, see Chapter III.

2.3. Modelling History

The model development history of lead-acid batteries starts from late fifties. Newman and Tiedemann [35] have provided a good review of the development in the theory of flooded porous electrodes prior to 1975. The further development was made along the following lines:

1. *Cell model.* Tiedemann and Newman [59] applied flooded electrode theory to the development of a complete cell model, describing the discharge behaviour of the lead acid battery system. Gu, Nguyen and White [22] proposed a model for discharge, rest and charge. Nguyen, White and Gu [37] applied similar model to VRLA-batteries. They introduced SOC as a dynamic parameter in the model.
2. *Two-dimensional model.* Dimpault-Dracy, Nguyen and White [13] proposed a 2D-model. Bernardi and Gu [4] made further development. The model proposed by Gu, Wang and Liaw [23] is the most complete: acid stratification due to convection is accounted for in that model. The Darcy's law is used for description of the fluid dynamics in porous media. The concentration profiles and flow velocities are compared with measured data.
3. *Two-step reaction.* Simonsson, Ekdunge and Lindgren [55] and Ekdunge and Simonsson [15] found that the dissolution process (charge transfer) is the rate-limiting step at higher overvoltage. The diffusion is rate-limiting at lower overvoltage. They proposed a new electrode reaction model. SOC was accounted for in their model. Landfors, Simonsson and Sokirko [32] applied this model in cell prediction and demonstrated a good fit of model against experimental data. The porosity and acid concentration distribution in the cell were measured and predicted by the model.
4. *Overcharging.* The latest progress has been made in description of the behaviour of battery under float charging. For details, see Chapter III.
5. *Impedance.* For details on battery evaluation in frequency domain, see Chapter IV.

2.4. Model

A basic model developed for lead-acid cell by White, Newman, and other authors is considered in this section. In later sections, it is solved numerically, calibrated and

tested on experimental data, and then applied for evaluation of the state and backup time of batteries.

The charge-discharge behaviour of a battery depends on electrode kinetics, which in turn is affected by variation of the electrode potential (especially in electrolyte), variation of the electrode porosity, and variation of the acid density in the pores of electrode.

2.4.1. Electrode Kinetics

The electrode reaction current is related with material of electrode as follows [4], [23]

$$\frac{\partial i_l}{\partial x} = Aj, \tag{2.1}$$

where
i_l - current density in the liquid phase in pores of electrode, A/cm^2,
A - active surface area per unit volume of porous electrode, cm^2/cm^3,
j - transfer current density from electrolyte to solid matrix, A/cm^2,
Aj - volumetric reaction rate, A/cm^3,
x - depth of porous electrode (zero at interface with bulk electrode), cm.

Surface area. The active surface area between solid and liquid phases depends on the utilisation of the electrode. The surface area in discharge and recharge reactions can be estimated as

$$A = A_{max}\theta^{\beta 1} - \text{discharge}, \tag{2.2}$$

$$A = A_{max}\frac{\rho}{\exp(\gamma\theta)} - \text{recharge}. \tag{2.3}$$

where
A_{max} - maximum active surface area, cm^2/cm^3,
ρ, γ - electrode morphology coefficients, no unit,
β_1 - tortuosity exponent, no unit,
θ - SOC, no unit.

The function for discharge (2.2) has been proposed in the literature [4], [15], [23], [37] and was found to work rather well in our experiments if tortuosity exponent with value of 0.5 is used (other proposed values were also tested and found to not work as well).

The exponential function for charge (2.3), by author, can also predict the surface area rather precisely as shown in [P1] where the simplified (2.3) and exact formulas were introduced and compared. It was indirectly verified to work better than the charge functions proposed in the literature.

It should be noted that representing surface area in modelling is a rather complex problem and it is not guaranteed that one model will work with all charge/discharge rates. The models (2.2) and (2.3) work well at least in the 0.5-10 h range used in this work.

Charge. The SOC is a fraction of theoretical (reference) capacity that can be evaluated by variation of the current density from the relationship [4], [23]

$$\frac{\partial\theta}{\partial t} = \frac{\alpha_{Ah}}{Q_{max}} \frac{\partial i_l}{\partial x}, \tag{2.4}$$

where
θ - SOC, no unit.
Q_{max} - theoretical (reference) capacity, C/cm^3,
α_{Ah} - charging efficiency, no unit,
t - time, sec.

The charging efficiency is defined for charging process as the ratio between required charge (Ah) and available capacity (Ah). It improves the model accuracy. A local loss of accuracy is small (3-6 %) per single step but it accumulates during recharge process if this parameter is ignored (total loss is large). This simple fact has not been recognised properly in the literature.

The SOC is always lower than the one calculated based on pure current due to heat generation and dissipation, current losses through isolation and battery gassing.

Reaction rate. The transfer current density depends on overpotential; it is limited by acid concentration. The exchange current density and apparent transfer coefficients are specific parameters of this process [4], [13], [23], [37]

$$j = i_0\left(\frac{c}{c_{ref}}\right)^{\beta 2}\left[\exp\{\alpha_a \frac{F}{RT}\eta\} - \exp\{-\alpha_c \frac{F}{RT}\eta\}\right], \tag{2.5}$$

where
i_0 - exchange current density for standard temperature of 25^o C, A/cm^2,
c - acid concentration, mol/cm^3,
c_{ref} - reference (initial) concentration, mol/dm^3,
β_2 - tortuosity exponent, no unit,
η - surface overpotential, $\eta = \phi^s - \phi^l - U$,
$\phi^s - \phi^l$ - electrode polarisation, V,
ϕ^s - solid matrix potential, V,
ϕ^l - electrolyte potential, V,
U - thermodynamic equilibrium potential, V,
α_a - anodic apparent transfer coefficient,
α_c - cathodic apparent transfer coefficient, $\alpha_c = 2 - \alpha_a$,
T - temperature, K,
R - universal gas constant, 8.3145 J/mol-K,
F - Faraday's constant, 96487 C/mol.

The exchange current density depends on temperature. The following formula [8] is used for correction of the exchange current density in wide temperature range

$$i_0(T) = i_0 \exp\{\frac{E_A(T - T_0)}{RT_0T}\},$$

where
E_A - activation energy, 50 kJ/mole,
T_0 - standard temperature, 298.2^o K (i.e. 25^o C).

The thermodynamic equilibrium potential depends on acid concentration and (weakly) on temperature. It is equal to reference potential U_{ref} at reference concentration c_{ref} = 4.9 mol/dm^3; in general, empirical formula U(c,T) or tabulated data [5] is used for approximation.

2.4.2. Potential in Solid Matrix

Ohm's law relates the current and potential in the solid matrix of electrode [4], [13], [23], [37]

$$i_s = -\sigma^{eff} \frac{\partial \phi^s}{\partial x}, \tag{2.6}$$

where
i_s - current density in solid matrix of electrode, $i_s = i_{app} - i_l$, A/cm^2,
i_{app} - applied current, A/cm^2,
ϕ^s - potential in solid matrix of electrode, V,
σ^{eff} - conductivity of porous electrode, $\sigma^{eff} = \sigma\varepsilon^{\beta 3}$,
σ - conductivity of bulk electrode: Pb or PbO_2, S/cm,
ε - porosity of electrode, fraction of electrode saturated with acid, no unit,
β_3 - tortuosity exponent, no unit,
x - depth of electrochemical cell (zero in the centre of positive electrode and maximum in the centre of negative electrode), cm.

The conductivity of the bulk electrode is high (0.5 kS/cm) for positive electrode and especially high (48 kS/cm) for negative electrode. The voltage drop is nearly zero for lead acid battery. It can be neglected in most applications without loss of accuracy.

2.4.3. Potential in Electrolyte

Ohm's law for solution relates the current and potential in electrolyte [3], [4], [23], [37]

$$\frac{i_l}{\kappa^{eff}} = -\frac{\partial \phi^l}{\partial x} + \frac{RT}{F}(1 - 2t^o_+)\frac{\partial \ln fc}{\partial x}, \tag{2.7}$$

where
i_l - current density in electrolyte, A/cm^2,
ϕ^l - potential in electrolyte, V,
κ^{eff} - conductivity of porous electrodes or separator, $\kappa^{eff} = \kappa\varepsilon^{\beta 4}$, S/cm,
κ - acid conductivity, S/cm,
$\kappa = \kappa_{ref}$ at room temperature 25^o C and acid concentration 4.9 mol/dm^3; in general, empirical formula [36] can be used for approximation, as done in this work.
ε - porosity, volume fraction filled with acid, no unit,
β_4 - tortuosity exponent, no unit,
t^o_+ - transference number, share of total current carried by ions of hydrogen, no unit,
f - molar activity coefficient.

This relationship in a more explicit form for molar activity can be represented [13] as

$$\frac{i_l}{\kappa^{eff}} = -\frac{\partial \phi^l}{\partial x} + \frac{RT}{F}[(3 - 2t^o_+)/c + 2V_o/(1 - cV_e)]\frac{\partial c}{\partial x}, \qquad (2.8)$$

where
V_o - partial molar volume of acid in electrolyte, cm^3/mol,
V_e - partial molar volume of water in electrolyte, cm^3/mol.

This formula (2.8) is applied for evaluation of batteries in this work.

2.4.4. Electrode Porosity

The porosity of electrode is a volume fraction filled with acid that can be evaluated by history of the variation of the current density from the relationship [4], [13], [23], [37]

$$\frac{\partial \varepsilon}{\partial t} = K_1 \frac{\partial i_l}{\partial x}, \qquad (2.9)$$

where
ε - porosity: volume fraction filled with acid, no unit,
i_l - current density in electrolyte, A/cm^2,
K_1 - equivalent volume to charge constant, cm^3/As,

$$K_1^+ = \frac{1}{2F}\left(\frac{M_{PbSO4}}{\rho_{PbSO4}} - \frac{M_{PbO2}}{\rho_{PbO2}}\right) \text{ - pos. electrode,}$$

$$K_1^- = -\frac{1}{2F}\left(\frac{M_{PbSO4}}{\rho_{PbSO4}} - \frac{M_{Pb}}{\rho_{Pb}}\right) \text{ - neg. electrode,}$$

M - molecular weight of species, g/mol,
ρ - density of species, g/cm^3.

2.4.5. Acid Concentration

The acid concentration is related with current of reaction rate and diffusion (migration) of ions as follows [4], [13], [23], [37]

$$\varepsilon \frac{\partial c}{\partial t} = \frac{\partial}{\partial x} D^{eff} \frac{\partial c}{\partial x} + (K_2 - cK_1)\frac{\partial i_l}{\partial x}, \qquad (2.10)$$

where
c - acid concentration, mol/cm^3,
D^{eff} - diffusion in porous media, $D^{eff} = D\varepsilon^{\beta 5}$,
D - diffusion constant of electrolyte, cm^2/s,
ε - porosity, no unit,
β_5 - tortuosity exponent, no unit,
$K_2 \frac{\partial i}{\partial x}$ - volumetric production rate of ions, mol/cm^3s,
K_2 - equivalent molarity to charge constant, mol/As,

$$K_2^+ = (3 - 2t^o_+)/2F \text{ - pos. electrode}, \quad K_2^- = (1 - 2t^o_+)/2F \text{ - neg. electrode},$$

t^o_+ - transference number, no unit.

Diffusion depends on acid concentration and temperature. The diffusion constant is equal to reference value D_{ref} at standard temperature of 25^o C and acid concentration of 4.9 mol/dm^3; in general, empirical formula [36] can be used for approximation, as done in this work.

2.5. Calculation Method

The battery model can be represented as the following large-scale system

$$dz = [A_3 z - b(z)]dt, \quad z_t = z_0, \tag{2.11}$$

where
z - electrochemical state of battery, containing the following processes: current density, liquid potential, solid potential, porosity, acid concentration and SOC. Every process is represented in number of layers.
A_3 - three-diagonal matrix,
b - nonlinear function: combination of power function, hyperbolic function and exponential function, depending on co-ordinate.

The model is dynamic for porosity, acid concentration and SOC; it is static for other components, i.e. current and potential ($dx = 0$, $x = [i_l, \phi^l]^T$).

The system (2.11) can be solved using time-iterative calculation procedure ($t = 0, \Delta t, 2\Delta t, ...$).

$$z_{t+1} = z_t + [A_3 z_t - b(z_t)]\Delta t, \quad z_t = z_0. \tag{2.12}$$

Note that only an overview of calculation model was given in this section. For details of the calculation method, and description of real-time simulation software utilising this method, see Chapter V.

2.6. Battery Testing

The model prediction accuracy was evaluated against measured data in the following experiment [58]. Four batteries, connected in a string and placed into a chamber (container) (Fig. 2.1), were charged and discharged periodically at elevated temperature of $40\text{-}48^o$ C. A relatively low overcharging voltage of 2.20 voltage per cell (VPC) was used to prevent increased water decomposition in the experiment. The float voltage, applied current and temperature in container were measured and recorded continuously.

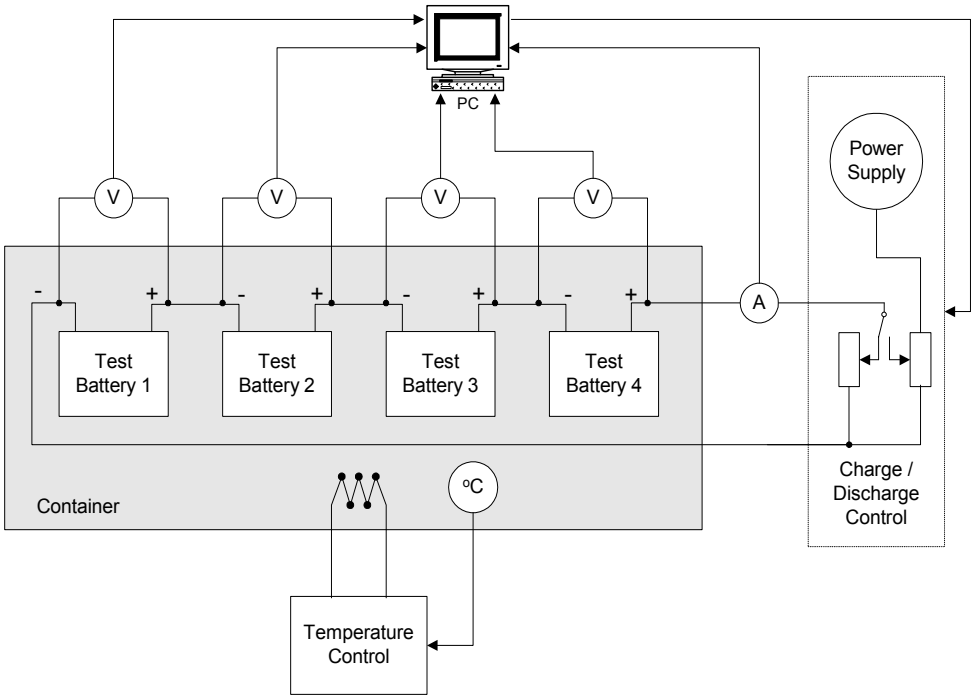

Fig. 2.1. Battery testing system.

Two types of VRLA batteries: A - gelled (gel technology) and B - absorbed (AGM technology) were tested on exploitation lifetime. These batteries, produced by different manufacturers, are similar by electrical parameters, but different by design.

Type A. Number of sections: 6. Number of positive plates: 4, negative plates: 3. Plate height: 11.3, width: 15.4 cm. Thickness of positive plate: 0.23 cm, negative plate: 0.22 cm. Thickness of separator: 0.36 cm.

Type B. Number of sections: 6. Number of positive plates: 3, negative plates: 4. Plate height: 13 cm, width: 11.6 cm. Thickness of positive plate: 0.32 cm, negative plate: 0.18 cm. Thickness of separator: 0.105 cm.

2.7. Model Calibration

Before the evaluation of a given battery string can be carried out, the model parameters need to be matched to the physical properties of the string. Although many parameters are known from literature and some beforehand, such as the number of batteries in a string, number of sections per battery, and dimensions of electrodes, many are unknown and cannot be directly measured. For these parameters, an automatic calibration procedure exists that runs each battery repeatedly against the measured data for the same string, each time with different model parameters, trying to match simulated total current and terminal voltage readings to the ones actually measured. The sum of least square errors of the model is used as the criterion for minimization. The following parameters are usually configured:

- Equivalent volume thickness of porous plates for both electrodes and separator.
- Tortuosity exponents for SOC-related reaction rate limitation.
- Maximum active surface area and electrode morphology coefficients.

- Exchange current density for both electrodes.

In software, the calibration process is reasonably quick (often less than one hour). Fast lumped parameter model can be used in the case of low discharging rates (C/I > 2 hours) and slower distributed parameter model in the case of high discharging rates (C/I < 2 hours).

It was observed on tested batteries that the above parameters affect model performance the most. However, if the need arises, other parameters can be chosen for calibration. Overall, the model currently has over 50 parameters common for all batteries in a string, plus 25 battery-related parameters. For details, see [P1].

After calibration, a good fit of model with measured data is usually obtained in a wide range of charge-discharge process (for example, see Fig. 2.2). The model is rather accurate in general but not everywhere, because the following processes are ignored (some of these are handled in later chapters):

- Non-faradic double-layer capacitance.
- Crystallisation effect (*coup de fouet*).
- Gassing.

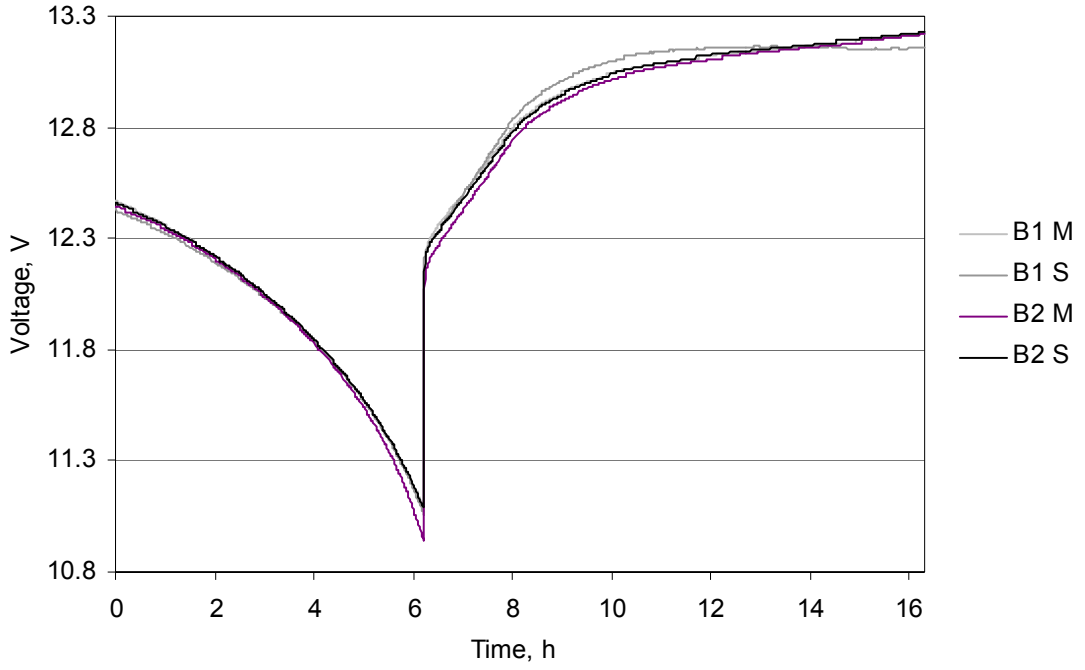

Fig. 2.2. Comparison of measured (M) and simulated (S) voltage for test batteries: B1, B2 of type A. The model predicted and measure voltages are close to each other during discharge, some more difference is observable during recharge.

The model is unable to predict these processes. It takes 5 minutes for a battery to come into steady-state condition after a long period of rest; it takes 1 minute if the battery was in use lately (this is not shown in Fig. 2.2). The model is relatively inaccurate during this relaxation time (beginning of discharge) and during switching from deep discharge to charge.

The model accuracy is rather high for most part of the charge-discharge curve. On average the least square error does not differ more than 0.1 mV and maximum error more than 120 mV from measured values in the range 10.5-13.5 V.

2.8. Battery Analysis

The main difference between outwardly equal batteries can be seen by model. It has different values (often by as much as 25%) for the following parameters:

- Thickness of electrodes.
- Thickness of separator.
- Tortuosity of electrodes.

Active mass of electrodes and electrolyte volume in the test batteries evaluated by thickness of planar electrodes and separator is shown in Table 2.1 and Table 2.2. Some material (up to 40-75%) is unreachable in real battery: lead or lead dioxide buried under insulating lead sulphate is not reachable for electron transfer because of low conductivity. This material is passive in electrochemical system, and is not shown in Table 2.1 and Table 2.2.

Table 2.1. Active mass and electrolyte volume of test batteries of type A.

	Positive Electrode, kg	Electrolyte dm^3	Negative Electrode, kg	Total kg
Battery 1	1.79	0.83	1.43	4.28
Battery 2	1.52	0.77	1.23	3.74
Battery 3	1.68	0.82	1.37	4.10
Battery 4	1.64	0.81	1.36	4.05

Table 2.2. Active mass and electrolyte volume of test batteries of type B.

	Positive Electrode, kg	Electrolyte dm^3	Negative Electrode, kg	Total kg
Battery 1	1.55	0.73	0.96	3.45
Battery 2	2.11	0.80	1.35	4.50
Battery 3	2.12	0.81	1.36	4.53
Battery 4	2.10	0.79	1.35	4.47

The battery capacity evaluated by model is different for every battery (Fig. 2.3). The active mass and battery capacity are strongly related. For example, battery number 2 is the weakest by charge and by total mass of active material in batteries of type A. The battery number 1 is the weakest by both parameters in batteries of type B.

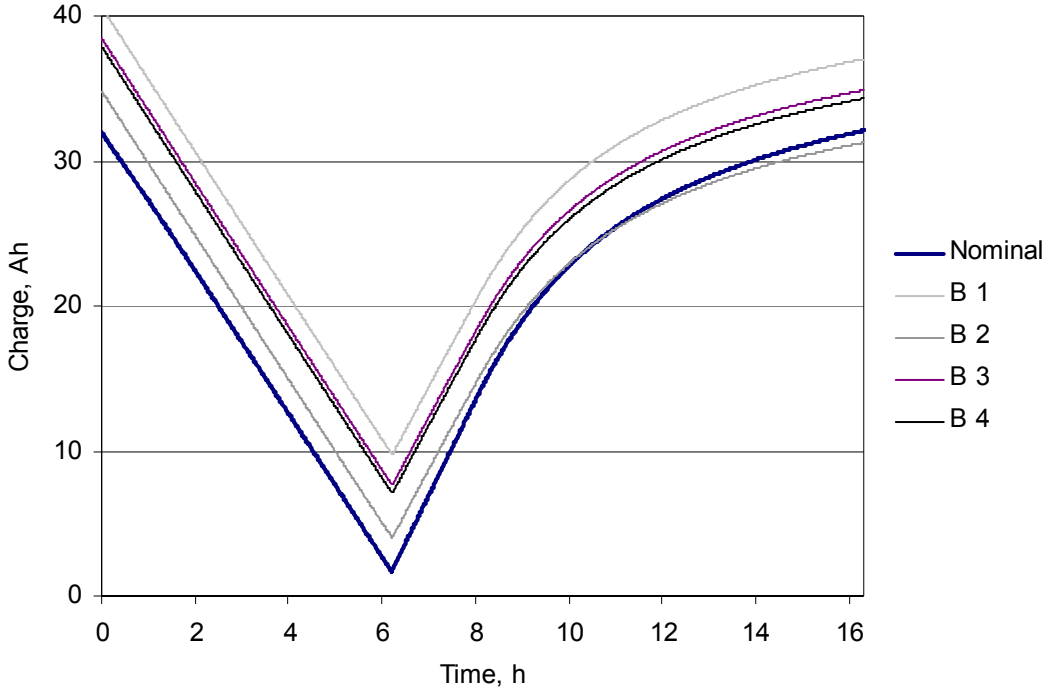

Fig. 2.3. Comparison of nominal and simulated capacities.

Thickness of electrodes and separator and morphology of electrodes is different for every battery. Similarly, the charging-discharging curves in Fig. 2.2 (compare the end part of discharge curve) and the backup times and cut-off times in Table 2.1 and Table 2.2, respectively, are different.

Thickness of electrodes and separator and morphology of electrodes can change during lifetime of a battery. This means that the model should be recalibrated from time to time, but also allows the changes during lifetime to be observed.

2.9. State Estimation

The electrochemical processes in a battery can be evaluated online by current-voltage measurements, as shown in figures in this section. Measured data (applied current, voltage and temperature in container) was used to evaluate unobservable processes on test battery 1. A full cycle from fully charged battery to deep discharge and back is shown.

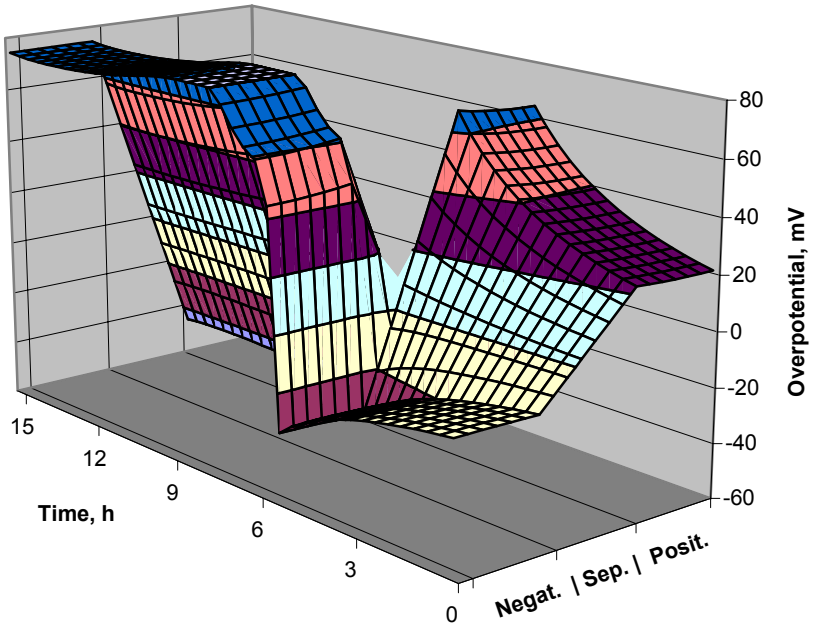

Fig. 2.4. Electrolyte overpotential (vs. SHE).

Electrolyte overpotential depends weakly on location and strongly on discharge time. It has highest (absolute) values in the end of discharge and at the beginning of charge.

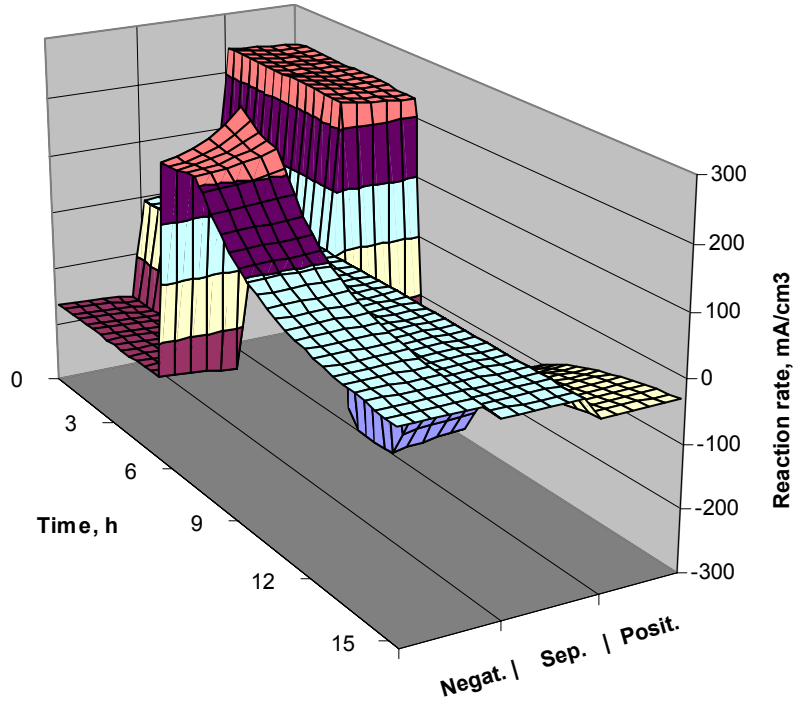

Fig. 2.5. Volumetric reaction rate.

The volumetric reaction rate depends weakly on location in electrode and strongly on discharge time. Reaction is well balanced if battery is normally charged. It is less stable in the end of discharge and at the beginning of charging process.

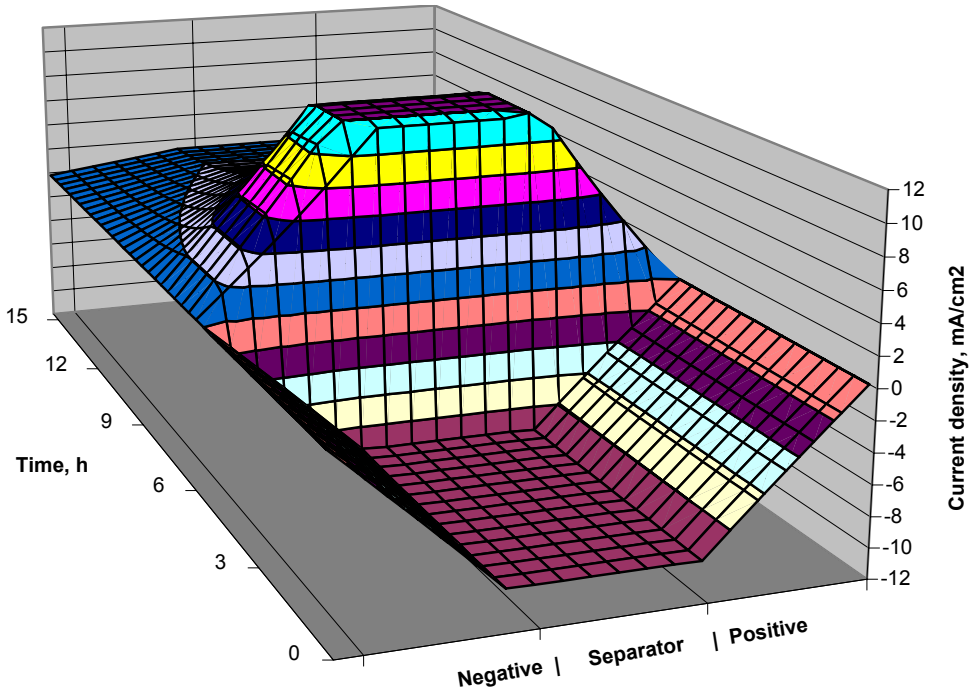

Fig. 2.6. Current density in electrode.

Because part of the current is transferred to solid matrix, current density in liquid phase depends on location in electrode almost linearly; it is constant in separator.

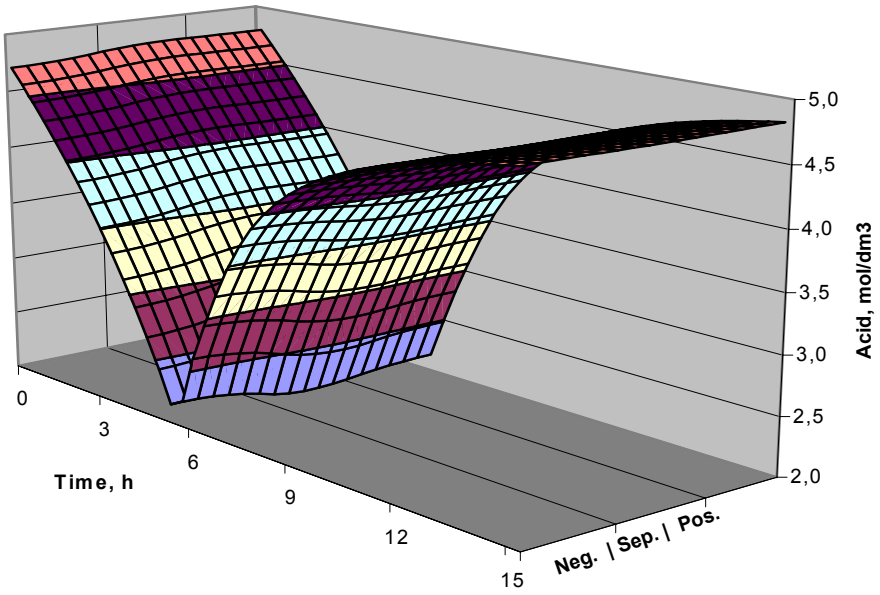

Fig. 2.7. Acid concentration in electrode (5 A).

Acid concentration depends weakly on location in electrode and strongly on discharge time. Because of diffusion, acid concentrations in positive electrode, negative electrode, and separator are nearly equal. There is no indication that acid depletion is limiting factor for the current applied in Fig. 2.6; however, at higher current (> 50 A), it does become limiting [P1].

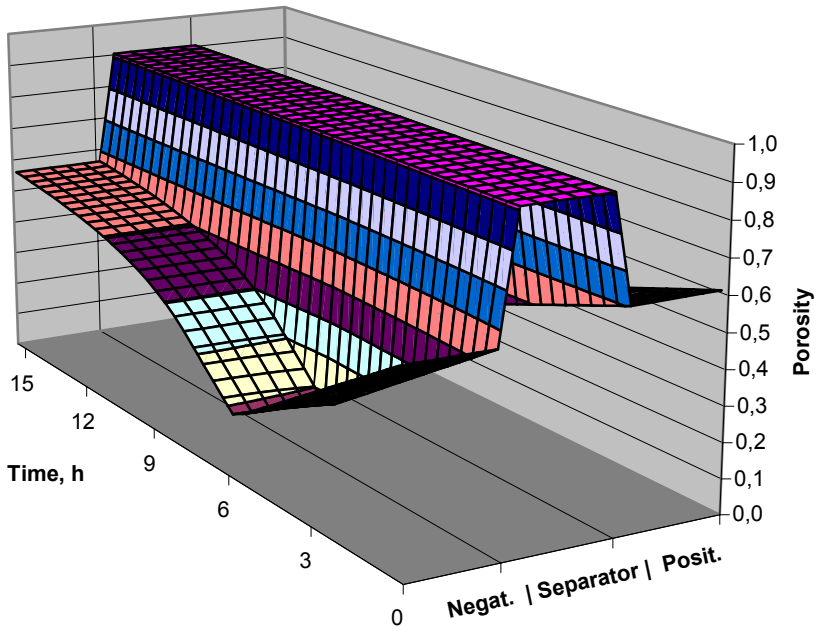

Fig. 2.8. Porosity of electrode.

Porosity depends weakly on location in electrode and strongly on discharge time. It is lower in negative electrode in comparison with positive electrode and in the end of discharge. Porosity is highest in a fully charged battery.

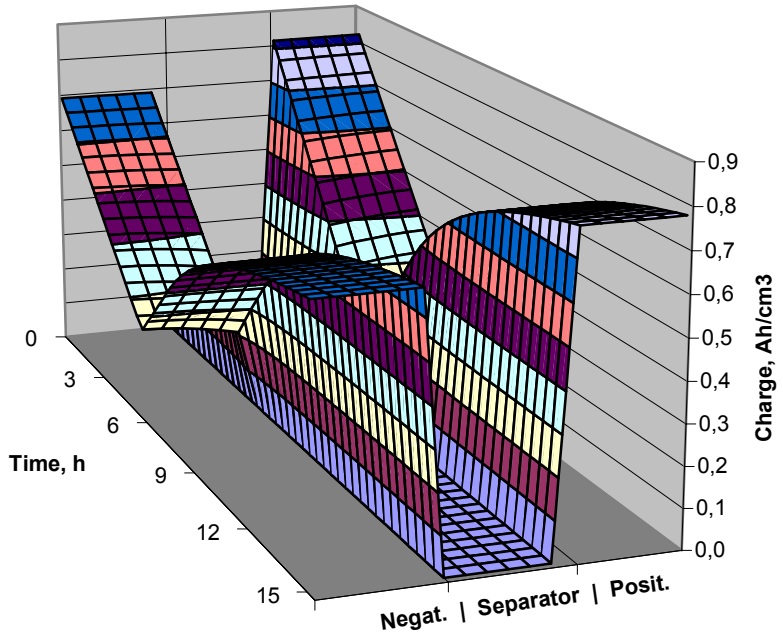

Fig. 2.9. Electrode capacity.

Electrode-specific capacity depends weakly on location in electrode and strongly on discharge time.

There is good evidence in above figures that a much faster lumped parameter model can be used for evaluation of the processes in battery if the discharging rate is relatively low. The electrochemical processes observed are nearly independent of their location in electrode. A discharging rate of C/I = 5 h was used in the experiment. To some extent, higher discharging rates C/I < 1-2 h can be expected in a telecommunications UPS system. In this case, a distributed parameter model should be used. However, in most cases, batteries can be approximated with lumped parameter model or low-dimension model.

2.10. Evaluation of Backup and Cut-off Times

In the following simulation, backup times and cut-off times of test batteries were evaluated with calibrated model.

Backup time is defined at level where 90 % of battery capacity is used up.

Cut-off time is defined at level where battery voltage drops below 9.3 V. This corresponds to cell voltage of 1.55 VPC, a standard cut-off level for high-rate discharge used by battery manufacturers.

The backup time and cut-off time of test batteries 1-4 of type A on discharge current of 5-50 A at temperature of 40° C is shown in Table 2.3 and Table 2.4, respectively.

Table 2.3. Backup time in minutes for test batteries 1-4 in dependence on load.

	Load 5 A	Load 10 A	Load 20 A	Load 35 A	Load 50 A
Battery 1	404	202	100	57	40
Battery 2	365	182	91	52	36
Battery 3	400	200	99	57	39
Battery 4	398	199	99	56	39

Table 2.4. Cut-off time in minutes for test batteries 1-4 in dependence on load.

	Load 5 A	Load 10 A	Load 20 A	Load 35 A	Load 50 A
Battery 1	455	226	111	60	38
Battery 2	412	206	103	57	37
Battery 3	451	224	110	59	38
Battery 4	448	222	110	59	38

The effect of acid depletion can be seen at 50 A load. On higher loads, acid depletion becomes the limiting factor of fully utilizing the battery capacity.

It can be seen from the results that Battery 2 is weaker than the others. Actually, its capacity is 35 Ah at 42° C against other batteries' 41 Ah (Bat. 1), 39 Ah (Bat. 3), and 38 Ah (Bat. 4).

Telecommunications UPS system is designed for nominal battery capacity and load with some reserve. Real backup time being lower than nominal is considered as a battery failure. The nominal capacity of the above batteries is 30 Ah, so there were no problems with them.

2.11. Conclusion

As shown in this chapter, the theoretical cell model can be calibrated to match with the measured data rather accurately. This allows model-based evaluation of unobservable electrochemical processes in battery, or even fully automatic battery monitoring. This is important, because significantly more information on SOH of battery can be withdrawn from applied model and direct current-voltage measurements than from conductivity or impedance measurements. Among others, backup time and cut-off time – important parameters for telecommunications UPS system – can be tested quite easily. However, battery model should be calibrated from time to time for every battery since active material diminish and morphology changes with age.

A common loading range C/I > 2-5 h for telecommunications UPS system allows using a really fast (10^5+ times faster than physical process) lumped parameter model or low-dimension model for system monitoring as the electrochemical processes are in weak dependence of location in electrode at lower discharge rates.

It should be noted that the model accuracy is limited due to some ignored processes. The following two improvements are important for monitoring of batteries in an UPS system:

1. More accurate models should be developed to predict gas formation processes for battery in overcharging conditions. Chapter III covers this.
2. Dynamics of the double-layer should be accounted for in the calculation model. As a result, battery switched from charge to discharge frequently can be evaluated more precisely. Double-layer dynamics are explored in Chapter IV.

Chapter III

3. Evaluation of Battery under Overcharging

3.1. Introduction

In UPS systems, the condition monitoring of a battery cannot be based on extensive discharging due to increased risk of down time. However, it has turned out that a short discharge, and the subsequent recharging, including overcharge, may provide the information needed for the accurate prediction of discharge behaviour of a battery and its SOH. The key is the overcharge process.

In the model covered in Chapter II, gas formation processes in a battery were ignored. These processes are not very active under normal charging/discharging conditions and can, for the most part, be ignored. However, when overcharging a battery, they become rather important and consequently, ignoring gas formation processes causes significant loss of accuracy of the model.

The purpose of this chapter is to propose a model for overcharging of a battery. The model covers the full discharge-recharge cycle including deep discharge and overcharge. It is an extension of the model presented in Chapter II. This model is modified by developing a new formula for electrode morphology, applying charging factor to SOC, electrode porosity and acid concentration as well as considering the recombination of oxygen as mass-transport limited evolution process and introducing other, smaller modifications.

The material in this chapter is mainly based on [P6]. The following conventional reaction scheme of a VRLA battery [5] is considered in this chapter.

Positive electrode

Primary reaction: charge or discharge

$$PbSO_4 + 2H_2O \Leftrightarrow PbO_2 + HSO_4^- + 3H^+ + 2e^-$$

Oxygen evolution

$$2H_2O \rightarrow O_2 + 4H^+ + 4e^-$$

Grid corrosion

$$Pb + 2H_2O \rightarrow PbO_2 + 4H^+ + 4e^-$$

Negative electrode

Primary reaction: charge or discharge

$$PbSO_4 + H^+ + 2e^- \Leftrightarrow Pb + HSO_4^-$$

Oxygen reduction

$$O_2 + 4H^+ + 4e^- \rightarrow 2H_2O$$

Hydrogen evolution

$$2H^+ + 2e^- \rightarrow H_2$$

3.2. Modelling History

The history of modelling of a lead-acid battery dates back to the late 50-s and is briefly covered in Chapter II. From the overcharging point of view the following two improvements are significant.

1. *Two-step reaction.* In [16], [55] it is shown that the dissolution process is the rate limiting factor at higher overvoltage and the diffusion rate is the limiting factor at lower overvoltage. A new dissolution-electrode reaction model was proposed including the effect of SOC. This model was applied to the prediction of cell behaviour in [32] demonstrating a good fit of model and experiment for acid concentration and porosity of electrodes.
2. *Overcharging.* The latest progress has been made in describing the behaviour of a battery under float charging. The gas formation processes in VRLA batteries have been analysed in [5], [6], [7], [8], [9] using simple lumped parameter model. This model was thoroughly tested experimentally. The gas formation processes were also analysed in [3] with a distributed parameter model and in [29] with a 2D-model. In [35], it is suggested that the dissolution-limited electrode reaction model, proposed in [55], could improve the accuracy of the model. They show somewhat better accuracy of model against measured data provided in [3]. However, even better accuracy is shown in [24], [25] on the same set of data using simple single-step reaction model with different function for electrode morphology. The latter model is tested on a new set of data in [33], showing less agreement of the model with measured data during overcharging. This chapter attempts to clarify the somewhat fuzzy picture presented in the literature.
3. *Scattering.* VRLA battery voltage scattering has been under continued interest from characterisation [3], [36], [51], [52] and optimal charging [47] viewpoints.

3.3. Contribution

Accuracy and reliability of the models covered in previous section is not high for overcharging. They have only been tested in a few experiments. This work is continued in this chapter with improved model on a new set of experimental data. The following changes are introduced to the models proposed in [3], [36].

1. The battery model is modified with respect to electrode morphology. In addition to SOC, the charging factor is applied in electrode porosity and acid concentration models. Mass transport of oxygen through separator is considered in more detail.

The recombination of oxygen is considered as a mass-transport limited evolution process.

2. It is stated that the theoretical cell model can be simplified when applied to battery testing. The single-step reaction model has the same prediction accuracy as the two-step reaction model. The partial pressure of gases can be eliminated from the electrode reaction equation using preset pressure window for valve.
3. The model is calibrated using experimental data in respect to gas formation processes.
4. High prediction accuracy of the model is demonstrated in a wide range of charge-discharge processes, including deep discharge and overcharge. It is shown that different behaviour of individual batteries in series during the overcharge can be predicted.
5. The model is applied to the unobservable gas formation processes in the battery. Oxygen evolution and recombination processes and water dry-out are evaluated during discharge, recharge and overcharge.

3.4. Model

The charge-discharge behaviour of a battery depends on electrode kinetics affected by the electrode potential in solid matrix and electrolyte, electrode porosity, and the acid density in pores of electrode.

Chapter II introduced the (slightly modified) basic model developed for lead-acid cell by White, Newman, Simonsson and other authors. In this section, this model is modified again to take into account gassing processes.

3.4.1. Electrode Kinetics

The electrode reaction current is related to the material of the electrode (lead or lead dioxide) and electrolyte (water and sulphuric acid) as follows

$$\frac{\partial i}{\partial x} = \frac{\partial i_M}{\partial x} + \frac{\partial i_{O2}}{\partial x} + \frac{\partial i_{H2}}{\partial x} + \frac{\partial i_K}{\partial x}, \tag{3.1}$$

where
i - current density in the liquid phase in pores of electrode, A/cm^2,
i_M - current density (2.1) generated by primary reaction with lead or lead dioxide,

$$\frac{\partial i_M}{\partial x} = A_M j_M,$$

A_M - active surface area per unit volume of porous electrode, cm^2/cm^3,
j_M - transfer current density for primary reaction, A/cm^2,
$A_M j_M$ - volumetric reaction rate, A/cm^3,

i_{O2} - current density generated by oxygen reaction, A/cm^2,

$$\frac{\partial i_{O2}}{\partial x} = A_{O2} j_{O2}, \tag{3.1b}$$

A_{O2} - active surface area for oxygen reaction, A/cm^2,
j_{O2} - transfer current density for oxygen reaction, A/cm^2,

i_{H2} - current density generated by hydrogen reaction, A/cm^2,

$$\frac{\partial i_{H2}}{\partial x} = A_{H2} j_{H2},$$

A_{H2} - active surface area for hydrogen reaction, A/cm^2,
j_{H2} - transfer current density for hydrogen reaction, A/cm^2,

i_k - current density generated by corrosion reaction, A/cm^2,

$$\frac{\partial i_k}{\partial x} = A_k j_k,$$

A_k - active surface area for corrosion reaction, A/cm^2,
j_k - transfer current density for corrosion reaction, A/cm^2.

Observant reader might notice the similarity of Eq. (3.1) to Eq. (2.1). Due to the fact that the electrode kinetics are different for the primary reaction and gassing reactions, gassing-specific parts are simply added to equations wherever possible, leaving the main reaction part, introduced in Chapter II and now denoted with index $_M$, intact.

Surface area. The active surface area between solid and liquid phases depends on the utilisation of the electrode. The surface area in discharge and recharge reactions can be estimated as

1. Primary reaction

$$A_M = A_{max}\theta^{\beta 1} \text{ - discharge,} \tag{3.2}$$

$$A_M = A_{max}\frac{\rho}{\exp(\gamma\theta)} \text{ - recharge.} \tag{3.3}$$

2. Oxygen and hydrogen reactions (for both discharge and recharge)

$$A_{O2} = A_{H2} = A_k = A_{max}\theta^{\beta 1},$$

A_{max} - maximum active surface area, cm^2/cm^3,
ρ, γ - electrode morphology coefficients, no unit,
β_1 - tortuosity exponent, no unit,
θ - SOC, no unit.

The SOC is defined as a charge fraction from theoretical (reference) capacity (2.4)

$$\frac{\partial\theta}{\partial t} = \frac{\alpha_{Ah}}{Q_{max}}\frac{\partial i}{\partial x}.$$

This equation is identical to Eq. (2.4), but here i designates total current density, not just the main reaction.

Single-step reaction. The volumetric reaction rate for the main reaction can be calculated from Eq. (2.5). This simplest reaction rate equation is adequate description of the charge-discharge behaviour of a battery under high or medium charging rates. A more complex two-step reaction model was suggested in [55], [15] and later in [36] for the batteries under low charging rate. This option is explored below.

Two-step reaction. The dissolution of sulphate crystals and formation of lead ions in solution is limited by solubility. The dissolution transfer current density is equal to [36]

$$j_M = 2F\, k_{PbSO4}(c_{Pb2} - c_{Pb2}^{*}), \tag{3.4}$$

where

c_{Pb2} - concentration of lead ions, mol/cm^3,

c_{Pb2}^{*} - saturation concentration, mol/cm^3,

k_{PbSO4} - mass-transfer coefficient for lead ions, cm/s.

The diffusion of lead ions from solution into the lead is limited by ions concentration. The diffusion transfer current density (2.5) is equal to

$$j_M = i_0^{M}\left(\frac{c}{c_{ref}}\right)^{\beta 2}\left[\exp\left(\alpha_a \frac{F}{RT}\eta\right) - \frac{c_{Pb2}}{c_{Pb2}^{*}}\exp\left(-\alpha_c \frac{F}{RT}\eta\right)\right]. \tag{3.5}$$

This is similar to the single-step reaction model but the cathodic reaction is dissolution-limited.

Two-step reaction model. Dependence on the lead ions can be eliminated from Eq. (3.5) using equality between dissolution (3.4) and diffusion (3.5) current densities. The two-step reaction model can be expressed [36] as

$$j_M = \frac{i_0^{M}\left(\frac{c}{c_{ref}}\right)^{\beta 2} I_{PbSO4}\left\{\exp\left[(\alpha_a + \alpha_c)\frac{F}{RT}\eta\right] - 1\right\}}{i_0^{M}\left(\frac{c}{c_{ref}}\right)^{\beta 2} + I_{PbSO4}\exp\left(\alpha_c \frac{F}{RT}\eta\right)}, \tag{3.6}$$

where I_{PbSO4} - limit current density for cathodic reaction, A/cm^2,

$$I_{PbSO4} = 2F\, k_{PbSO4}\, c_{Pb2}^{*}.$$

Its value is higher by an order of magnitude for positive electrode. The mass-transfer of lead ions into solution is much faster at positive electrode than at negative electrode. The two-step reaction model is assumed, as in [36], to be suitable model for negative electrode and single-step reaction model for positive electrode. However, this was not confirmed based in our experiments. Nearly equal accuracy was achieved experimentally for both reaction models, so a simpler single-step reaction model is used in this chapter.

Oxygen reaction. The transfer current density for oxygen reaction depends on overpotential as a two-directional process. Both processes, anodic and cathodic, are limited by acid concentration. The cathodic reaction is limited by the partial pressure of oxygen [36]

$$j_{O2} = i_0^{O2}\left(\frac{c}{c_{ref}}\right)^{\beta 3}\left[\exp\left(\alpha_{O2}\frac{F}{RT}\eta_{O2}\right) - \left(\frac{p_{O2}}{p_{O2}^{ref}}\right)^{\beta 4}\exp\left(-\alpha_{O2}\frac{F}{RT}\eta_{O2}\right)\right], \qquad (3.7)$$

where
i_0^{O2} - exchange current density for oxygen reaction, A/cm^2,
β_3, β_4 - tortuosity exponents, no unit,
η_{O2} - surface overpotential for oxygen reaction, $\eta_{O2} = \phi^l - \phi^s - U_{O2}$,
ϕ^s - solid matrix potential, V,
ϕ^l - electrolyte potential, V,
U_{O2} - thermodynamic equilibrium potential for oxygen, V,
α_{O2} - apparent transfer coefficient for oxygen, no unit,
p_{O2} - oxygen partial pressure, Pa,
p_{O2}^{ref} - reference pressure, Pa.

This model is close to the model presented in [3] and obtained by eliminating the partial pressure from the anodic reaction.

Thermal relationship. When the temperature deviates from the standard temperature, the exchange current density can be corrected by the equation given after Eq. (2.5). The activation energy is higher (E_A = 69 kJ/mole) for oxygen reaction than for primary reaction [8].

Oxygen evolution. The electrode potential U = 1.75 V on positive electrode is shifted far over the equilibrium potential (U_{O2} = 1.23 V) for oxygen, causing oxygen evolution on positive electrode. Because of this shifted potential, the current density for cathodic reaction is much lower than for anodic reaction, to the point where the cathodic reaction can be ignored on positive electrode. The oxygen evolution can be predicted as a single-directional anodic reaction on positive electrode that is not limited by partial pressure of oxygen [3]

$$j_{O2} = i_0^{O2}\left(\frac{c}{c_{ref}}\right)^{\beta 3}\exp\left(\alpha_{O2}\frac{F}{RT}\eta_{O2}\right). \qquad (3.8)$$

Oxygen reduction. On negative electrode, the reduction rate depends on oxygen transfer through separator and on oxygen recombination rate. The electrode potential of U = -0.32 V on negative electrode is shifted far below the equilibrium potential for oxygen (U_{O2} = 1.23 V), causing oxygen reduction on negative electrode. In this case, the recombination process is a single-directional cathodic reaction of (3.7) [3]

$$j_{O2} = -i_0^{O2}\left(\frac{c}{c_{ref}}\right)^{\beta 3}\left(\frac{p_{O2}}{p_{O2}^{ref}}\right)^{\beta 4}\exp\left(-\alpha_{O2}\frac{F}{RT}\eta_{O2}\right). \qquad (3.9)$$

This is a very fast process because the potential is shifted extensively (by 1.55 V). It is mainly limited by oxygen transport through separator and slightly by oxygen partial

pressure. The latter limitation is insignificant and can be ignored. The oxygen partial pressure is close to reference pressure p_{O2}^{ref} under correctly operating valves.

It is much more practical to evaluate the recombination rate proportionally to evolution rate and mass transport rate through separator than to do it by partial pressure of oxygen. The following mass-transfer and recombination model is proposed and verified in this chapter.

Oxygen transfer. The oxygen transfer through separator is evaluated by a simple mass-transfer model

$$\frac{\partial i_{O2}}{\partial t} = Q\frac{\partial i_{O2}}{\partial x}, \quad i_{O2}(x_{p/s}) = i_{O2}(x_{p/s}), \tag{3.10}$$

where
Q - oxygen flow velocity through separator, cm/s,
$i_{O2}(x_{p/s})$ - current density at the boundary between positive electrode and separator.

In general, the flow velocity depends on partial pressure, but approximation with constant flow velocity $Q = Q_0$ is a practical approach used in this work that works well, assuming normal operating conditions of valves.

The current density at the boundary between positive electrode and separator can be calculated as a boundary value solution of Eq. (3.8).

The oxygen transfer in separator can be the rate-limiting step in case of rapid changes in the evolution of oxygen on positive electrode. A transport-delay through separator is observable as a shock wave is the consequence of rapid change of oxygen evolution. This wave can be predicted by the model (3.10).

Oxygen recombination. The oxygen mass-transfer and reduction on negative electrode is proposed to be evaluated as follows

$$\frac{\partial i_{O2}}{\partial t} = Q_0\frac{\partial i_{O2}}{\partial x} + k_{ore}A_{O2}j_{O2}, \quad i_{O2}(x_{s/n}) = i_{O2}(x_{s/n}), \tag{3.11}$$

where
k_{ore} - oxygen recombination efficiency (ORE), no unit,
j_{O2} - transfer current density on negative electrode for oxygen reaction, calculated by single-directional (3.9), using reference pressure $p_{O2} = p_{O2}^{ref}$,
A_{O2} - active surface area of negative electrode, cm^2/cm^3,
$i_{O2}(x_{s/n})$ - current density at boundary between separator and negative electrode, calculated as a solution of Eq. (3.10) at boundary.

Penetration of oxygen is not deep in negative electrode. The reduction rate is fast because of shifted potential; there is not much oxygen penetrated under the surface layer of negative electrode.

Hydrogen reaction. The transfer current density for hydrogen reaction depends on overpotential as a two-directional process. Both processes, anodic and cathodic, are

limited by acid concentration. The anodic reaction is limited by the partial pressure of hydrogen [3]

$$j_{H2} = i_0^{H2}\left(\frac{c}{c_{ref}}\right)^{\beta 5}\left[\left(\frac{p_{H2}}{p_{H2}^{ref}}\right)^{\beta 6}\exp\left(\alpha_{H2}\frac{F}{RT}\eta_{H2}\right) - \exp\left(-\alpha_{H2}\frac{F}{RT}\eta_{H2}\right)\right], \qquad (3.12)$$

where
i_0^{H2} - exchange current density for hydrogen reaction, A/cm^2,
β_5, β_6 - tortuosity exponent, no unit,
η_{H2} - surface overpotential for hydrogen reaction, $\eta_{H2} = \phi^l - \phi^s - U_{H2}$,
U_{H2} - thermodynamic equilibrium potential for hydrogen, V,
α_{H2} - apparent transfer coefficient for hydrogen, no unit,
p_{H2} - hydrogen partial pressure, Pa,
p_{H2}^{ref} - reference pressure, Pa.

This model is similar to the oxygen reaction model of (3.7), modified for the hydrogen reaction.

Hydrogen pressure. The hydrogen partial pressure is close to reference pressure $p_{H2} = p_{H2}^{ref}$ under correctly operating valves.

Thermal relationship. The exchange current density can be corrected using equation given after Eq. (2.5) when the temperature deviates from the standard temperature. The activation energy is lower (E_A = 54 kJ/mole) for hydrogen reaction than for oxygen reaction [8].

Hydrogen evolution. The electrode potential U = -0.35 V on negative electrode is shifted significantly below equilibrium potential (U_{H2} = 0 V) for hydrogen. The hydrogen evolution can be predicted as a single-directional cathodic process on negative electrode [36]

$$j_{H2} = -i_0^{H2}\left(\frac{c}{c_{ref}}\right)^{\beta 5}\exp\left(-\alpha_{H2}\frac{F}{RT}\eta_{H2}\right). \qquad (3.13)$$

The hydrogen evolution is much smaller than oxygen evolution. Its effect on overall current (3.1) is insignificant if compared with oxygen evolution or recombination current.

Hydrogen reduction. Hydrogen reduction, as the reversal of hydrogen evolution, is possible at positive electrode, but is hindered at the PbO_2 surface so much that it can be neglected. Consequently, zero recombination process at positive electrode is assumed in this thesis.

Grid corrosion. The corrosion current can be approximated as suggested in [8]

$$j_k = -i_0^k \exp\left(-\alpha_k\frac{F}{RT}\eta_k\right),$$

where
i_0^k - excange current density for corrosion reaction, specified in [8] as 2.1 mA/100 Ah for domain I and 0.74 mA/100 Ah for domain II,

α_k - apparent transfer coefficient for corrosion, specified in [8] through Tafel slopes -240 mV/dec for domain I and +230 mV/dec for domain II.

The exchange current density i_0^k can be corrected using equation given after (2.5) when the temperature deviates from the standard temperature. The activation energy is specified as E_A = 69 kJ/mole in [8].

Simplification used. As explained in [8], hydrogen evolution, oxygen evolution/reduction and corrosion occur independently according to their individual current/potential curves. However, equal currents must flow through positive and negative electrode. Thus, the oxygen evolution current plus grid corrosion current at the positive electrode must be equal the hydrogen evolution current plus oxygen reduction current at the negative electrode. Oxygen evolution is almost completely (>98%) compensated by oxygen reduction in VRLA batteries. In the case of 100% recombination, the grid corrosion current is exactly equal to the hydrogen evolution current. With <100% recombination, the latter current is slightly larger.

Therefore one can reduce the order of the model at the expense of unobservable corrosion current, setting it to equal the hydrogen evolution current. In practice this is a good estimate if the recombination efficiency is over 98%. Note that this estimate is not valid for battery at rest and less good (but still usable) at elevated temperatures where the recombination efficency is lower. Also, batteries that come with very unbalanced hydrogen evolution/grid corrosion rates from the vendor (enough to cause 'discharged negative electrodes' syndrome and hence not really usable at the field), cannot be studied with this model.

3.4.2. Potential in Electrolyte

Ohm's law for solution relates the current and potential in electrolyte

$$\frac{i}{\kappa^{eff}} = -\frac{\partial \phi^l}{\partial x} + \frac{RT}{F}(1 - 2t^o_+)\frac{\partial \ln fc}{\partial x}.$$

This equation is identical to (2.7) presented in Chapter II, but here i designates total current density, not just the main reaction.

3.4.3. Electrode Porosity

The electrode volume fraction filled with electrolyte can be evaluated as

$$\frac{\partial \varepsilon}{\partial t} = K_1 \alpha_{Ah} \frac{\partial i}{\partial x}, \qquad (3.14)$$

where
ε - porosity, no unit,
α_{Ah} - charging efficiency, no unit,
K_1 - equivalent volume to charge constant, cm^3/C.

The electrode porosity is not affected by current for heat generation and dissipation. This current is eliminated from (3.14) by using charging efficiency factor (new in this chapter; compare with Eq. (2.9)).

3.4.4. Acid Concentration

The acid concentration depends on migration and diffusion of species. The migration is induced as ion current by primary reaction and oxygen and hydrogen reactions. The diffusion is induced by concentration gradient which is largest between positive electrode and separator

$$\varepsilon \frac{\partial c}{\partial t} = \frac{\partial}{\partial x} D^{eff} \frac{\partial c}{\partial x} + (K_2 - cK_1)\alpha_{Ah} \frac{\partial i}{\partial x} + K_3\left(\frac{\partial i_{O2}}{\partial x} + \frac{\partial i_{H2}}{\partial x}\right), \qquad (3.15)$$

where
c - acid concentration, mol/cm^3,
D^{eff} - diffusion in porous electrodes or separator, $D^{eff} = D\varepsilon^{\beta 8}$,
D - electrolyte diffusion constant, cm^2/s,
ε - porosity, no unit,
β_8 - tortuosity exponent, no unit,
α_{Ah} - charging efficiency, no unit,
K_2 - equivalent molarity to charge constant, mol/C,

$$K_2^+ = (3 - 2t^o_+)/2F \text{ - pos. electrode, } K_2^- = (1 - 2t^o_-)/2F \text{ - neg. electrode,}$$

K_3 - absolute constant, mol/C, $K_3^+ = -K_3^- = 1/2F$.

The ion migration due to water decomposition is accounted for in (3.15). The acid concentration is not affected by current for heat generation and dissipation. This current is eliminated from (3.15) using charging efficiency factor (new in this chapter; compare with Eq. (2.10)).

3.4.5. Gassing and Water Loss

Battery gassing is a result of incomplete recombination of oxygen and/or hydrogen evolution. Water dry-out is a consequence of extensive gassing.

Oxygen evolution and reduction. The local oxygen evolution rate in electrode is proportional to the oxygen reaction current on positive electrode (in advanced model, the grid corrosion could also be accounted for)

$$\frac{\partial m_{O2}^{evl}}{\partial t} = \frac{1}{4F} \frac{\partial i_{O2}^{+}}{\partial x}$$

and the reduction rate is proportional to the oxygen reaction current on negative electrode (in advanced model, the oxygen transfer through separator (3.10) could also be accounted for)

$$\frac{\partial m_{O2}^{red}}{\partial t} = -\frac{1}{4F} \frac{\partial i_{O2}^{-}}{\partial x},$$

where
m_{O2} - number of moles of oxygen generated or reduced locally in a single electrode, mol/cm^3,
i_{O2} - oxygen reaction current density for positive i_{O2}^+ or negative i_{O2}^- electrode, A/cm^2.

This model can be simplified if calculated for the whole electrode as a lumped parameter model. Equations (3.1b) and (3.7) solved for single layer gives the oxygen reaction current $i_{02}S_p = I_{02}$ for positive I_{02}^+ or negative I_{02}^- electrode in ampers. The total number of moles of oxygen generated or reduced on a single electrode can be calculated by integration of m_{O2} over volme of electrode, approximately $n_{O2} = S_p\Delta x\, m_{O2}$. Here S_p - plate area, cm^2 and Δx - plate thickness, cm.

This simplifies calculations of the oxygen evolution and reduction as well as calculation of the hydrogen evolution up to the differential system [36] explained below.

The oxygen evolution rate is proportional to the oxygen reaction current on positive electrode

$$\frac{dn_{O2}^{evl}}{dt} = \frac{1}{4F}(I_{02}^+ - I_k^+)$$

and the reduction rate is proportional to the oxygen reaction current on negative electrode

$$\frac{dn_{O2}^{rec}}{dt} = -\frac{1}{4F} I_{02}^-,$$

where
n_{O2} - number of moles of oxygen generated or reduced on a single electrode, mol,
I_{02} - oxygen reaction current for positive I_{02}^+ or negative I_{02}^- electrode, A,
I_k^+ - corrosion reaction current on positive electrode, A.

The reduction rate is proportional to the evolution rate according to steady-state recombination model (in advanced model, this could be replaced with non-constant ORE for improved accuracy)

$$\frac{dn_{O2}^{rec}}{dt} \approx k_{ore}\frac{dn_{O2}^{evl}}{dt} \text{ or } I_{02}^- \approx -k_{ore} I_{02}^+,$$

where k_{ore} - oxygen recombination efficiency, no unit.

Hydrogen evolution. The hydrogen evolution is proportional to the hydrogen reaction current on negative electrode [10]

$$\frac{dn_{H2}^{evl}}{dt} = -\frac{1}{2F} I_{H2}^- + \frac{1}{4F} I_k^+$$

where
n_{H2} - number of moles of hydrogen generated on negative electrode, mol,
I_{H2}^- - hydrogen reaction current on negative electrode, A.

The hydrogen recombination process on positive electrode is very slow and can be ignored.

The evolution and recombination processes between electrodes are irreversible by switching from discharge to recharge. The potentials for primary reactions are shifted

far from the equilibrium potentials for oxygen or hydrogen reactions. This makes reversion impossible. The gassing process during recharge is similar to discharge but more extensive because of further shifted potentials.

A possible imbalance between evolution and recombination rates will trigger the accumulation process of gasses in free space of battery. The oxygen accumulation and recombination processes are well balanced in VRLA battery.

The hydrogen evolution is progressive accumulation process but is much less extensive than evolution of oxygen:

$$\frac{dn_{O2}^{\ g}}{dt} = \frac{1}{4F}(I_{O2}^{\ +} - I_{O2}^{\ -} - I_k^{\ +}), \qquad \frac{dn_{H2}^{\ g}}{dt} = -\frac{1}{2F} I_{H2}^{\ -},$$

where $n_{O2}^{\ g}$, $n_{H2}^{\ g}$ - number of gas moles (oxygen or hydrogen) accumulated in the free space of battery, mol.

The following simplified models can be used for approximation of steady-state gassing process

$$\frac{dn_{O2}^{\ g}}{dt} = \frac{dn_{O2}^{\ evl}}{dt} - \frac{dn_{O2}^{\ rec}}{dt} \approx (1 - k_{ore})\frac{dn_{O2}^{\ evl}}{dt}.$$

The partial pressure of gases is proportional to the number of gas moles in the free space of battery accumulated under closed valve. Pressure that is any higher than the preset opening pressure of valve will trigger gas escape with rates

$$\frac{dn_{O2}^{\ esc}}{dt} = \frac{n_{O2}^{\ g}}{n_{O2}^{\ g} + n_{H2}^{\ g}} \frac{1}{4F}(I_{O2}^{\ +} - I_{O2}^{\ -} - I_k^{\ +}),$$

$$\frac{dn_{H2}^{\ esc}}{dt} = \frac{n_{H2}^{\ g}}{n_{O2}^{\ g} + n_{H2}^{\ g}} \left(\frac{1}{4F} I_k^{\ +} - \frac{1}{2F} I_{H2}^{\ -}\right).$$

The water dry-out equals to hydrogen escape through valve (the model ignores direct dry-out through the plastic box) as the gas is mostly (80 %) hydrogen

$$\frac{dn_{H2O}}{dt} = \frac{dn_{H2}^{\ esc}}{dt}.$$

Here n_{H2O} - number of water moles of dry-out, mol.

High water loss (over 10%) can drastically affect battery performance. Batteries with more than 15-20% water loss are replaced in most applications [29].

3.5. Experiment

The proposed model was tested experimentally [58]. It was first calibrated and then its accuracy evaluated against the measured data. A simple testing system was used to record measured data in the experiment. This system was the same as described in

Chapter II – see Fig. 2.1. The testing methodology used was also the same, with the exception of extended charging time (see below).

3.5.1. Experiment Description

The data presented in this chapter is relevant to the following operation of batteries [58]. A string of fully charged batteries was discharged after 1 day of rest with constant current at rate C/I = 5.6 h and then charged at rate C/I = 4.6 h for a short period until the voltage of 2.20 VPC was reached. Then, the charging current was reduced gradually to maintain voltage at approximately 2.24 VPC in all cells, making sure all batteries were charged completely.

Two sets of batteries, A and B, from the same manufacturer were used for testing.

Specification. Type: VRLA battery, gel technology. Nominal voltage: 12 V. Capacity: C = 28 Ah or more, cut-off time: 5, 10 or 20 hours at discharge current of 5.1, 2.8 or 1.6 A for cut-off voltage 1.70-1.75 VPC.

Battery design. Number of sections: 6. Number of positive plates: 4, negative plates: 3. Plate height: 11.3 cm, width: 15.4 cm. Thickness of positive plate: 0.23 cm, negative plate: 0.22 cm. Thickness of separator: 0.36 cm.

A lumped parameter model is used for data analysis in this chapter. It has the same approximation accuracy as the distributed parameter model. The charge-discharge rates of the experiment are relatively low (4-6 h). As explained in Chapter II, the electrochemical processes are in weak dependence on the location in electrode for rates that are over 1-2 h. The lumped parameter model used was obtained as a modification of the distributed parameter model approximated with a single layer per electrode.

3.5.2. Model Calibration

The calibrated model from Chapter II is used with some adjustments to electrode morphology, thickness of electrodes and separator, and charging exponent and efficiency. For details, see [P6].

In addition, the gassing process model is calibrated using similar identification method as earlier. The calibration results are shown for oxygen reaction in Table 3.1.

Table 3.1. Oxygen reaction parameters.

Parameter	Battery 1	Battery 2	Battery 3	Battery 4	Unit
$i_{0,O2}$	0.027	0.015	0.019	0.059	$\mu A/cm^2$
$\alpha_{a,O2}$	0.670	0.701	0.693	0.635	no unit

The following values were used as constants in the calculation algorithm:

Equilibrium potentials vs. SHE: $U_{O2} = 1.23$ V for oxygen, $U_{H2} = 0$ V for hydrogen.

Batteries of the same vendor are unequal. Variation of the (oxygen) apparent transfer coefficients and exchange current densities between batteries corresponds to the measured discharge curves and scattering in overcharging shown in Fig. 3.1. This

variation is relatively small: 1-10% for apparent transfer coefficients (Table 3.1) and 30-295% for exchange current densities (Table 3.1). The variation given in literature for Tafel slope (which is inverse proportional to the apparent transfer coefficient) is often several times larger: 11-22% (70, 80, 90 mV/dec referred in [31]) and for the exchange current density an order of magnitude larger: 42-3400 % (1-3, 1-5, 8, 34 μA/Ah referred in [31]). In our case, the same product from the same manufacturer is considered and this makes variation relatively small.

However, some variation exists even if batteries are produced in a short period from each other and in the same production line. It seemed that local higher acid filling/saturation [31] cannot be averaged at the same level by equal compression in manufacturing of batteries. It is difficult to prevent the acid to be unevenly administrated to the plate groups and separators (for example, the separator is shown unequally saturated: 54, 49.3, 40.8% in [1]) and in their different zones, causing unevenly distributed recombination, observable as a variation of the parameters. Also, the cracks that exist in a gelled cell further increase the uneven recombination distribution.

Whatever the origin for variation of parameters in Table 3.1, mass transport of oxygen or something else, the scattering of batteries (Fig. 3.1) can be predicted through these parameters better than through the electrode morphology and pressure parameters ([24], [25], [33]) or through the dissolution-limited electrode reaction [36].

3.5.3. Model Accuracy

To predict the charge-discharge behaviour of the batteries, the applied current for the model was chosen as close as possible to the one measured in the experiment. A special control algorithm, driving overpotential on both electrodes, was used to stabilise the applied current of the model at measured values. High tracking accuracy was obtained, with tracking error < 1 %.

Voltage. Typical charging curves are shown in Fig. 3.1. They were first measured and later predicted using the model. The prediction accuracy is high. The model can predict measured voltage in full range of charge-discharge processes including deep discharge and overcharge. The following situation is demonstrated in Fig. 3.1. Higher voltage is measured on batteries 2, 3 and lower voltage on batteries 1, 2 during overcharge (the string voltage is constant). Respectively, higher voltage is model-predicted on batteries 2, 3 and lower voltage on batteries 1, 2.

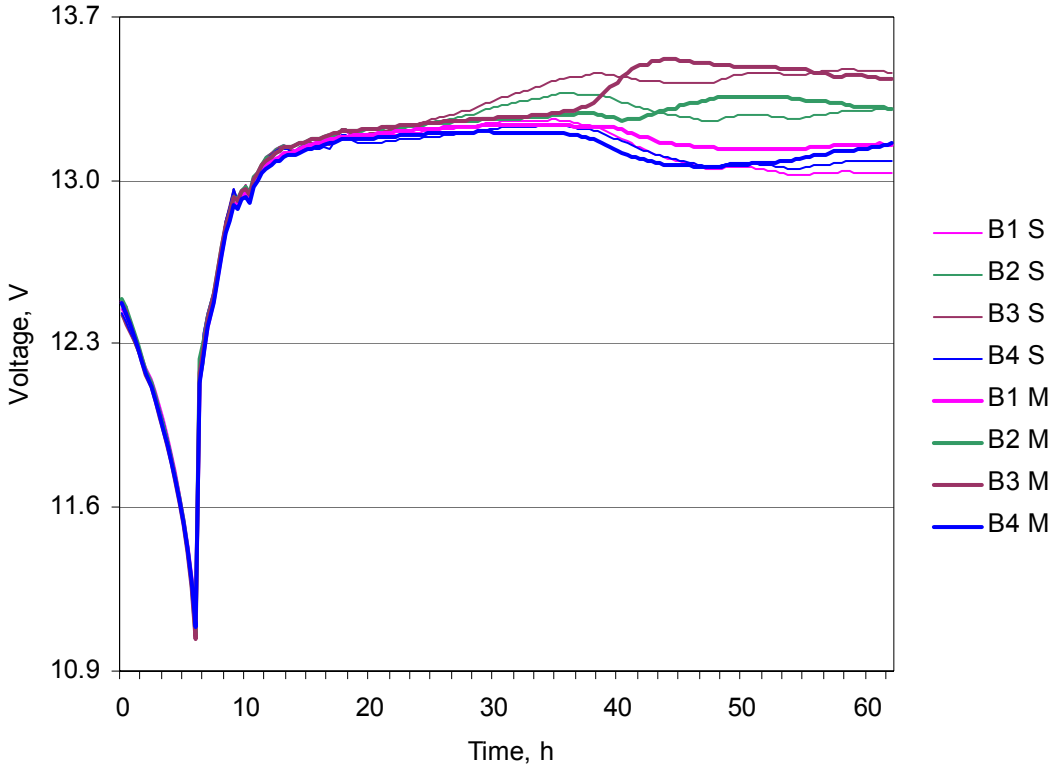

Fig. 3.1. Typical charging curves of tested batteries. Model-predicted and measured voltage is shown as a pair of fine and bold lines in the closest neighbourhood for every battery.

It should be noted that it was found in our tests that the float voltage during over-charge cannot be used as a simple indicator of SOH of a battery [P6].

SOC. When the model-predicted charge and the charge calculated by applied current were compared, it was found that the model-predicted capacity (maximum charge) of 36, 34, 34 and 36 Ah of batteries 1, 2, 3, and 4, respectively, is lower than the capacity of 37 Ah computed using applied current. This is because the applied current is higher than real charging current due to heat generation and dissipation, current loss through isolation and water decomposition in batteries.

Model improvement. The mass transport of oxygen (3.10) is considered the model at basic level. We belive that an advanced mass transport model with gas diffusion through thin liquid film [46] would be more relevant to physics and 2D model ([4], [13], [23]) relevant to local acid saturation in real battery, but it would also be more difficult to implement in calculation (involves many unobservable processes) and more difficult to implement in monitoring. From the monitoring viewpoint, it is not as important to identify the original source of scattering as it is to predict scattering, something the model does relatively well.

3.6. State Estimation

The calibrated model can be applied for the evaluation of the unobservable processes in battery using observable processes. The gas formation processes are evaluated and analysed using current-voltage and temperature measurements in this section. Their possible use in battery monitoring is discussed.

A retrospective analysis is applied. The unobservable processes are evaluated by means of (calibrated) theoretical cell model, using current-voltage and temperature measurements recorded experimentally in charge-discharge processes.

Charging efficiency. The share of applied current between primary and gassing reactions is in favour of gassing reaction during overcharge, as shown in Fig. 3.2. The charging process is ineffective during overcharge. The primary reaction current is lower for batteries 3 and 2 than for batteries 1 and 2.

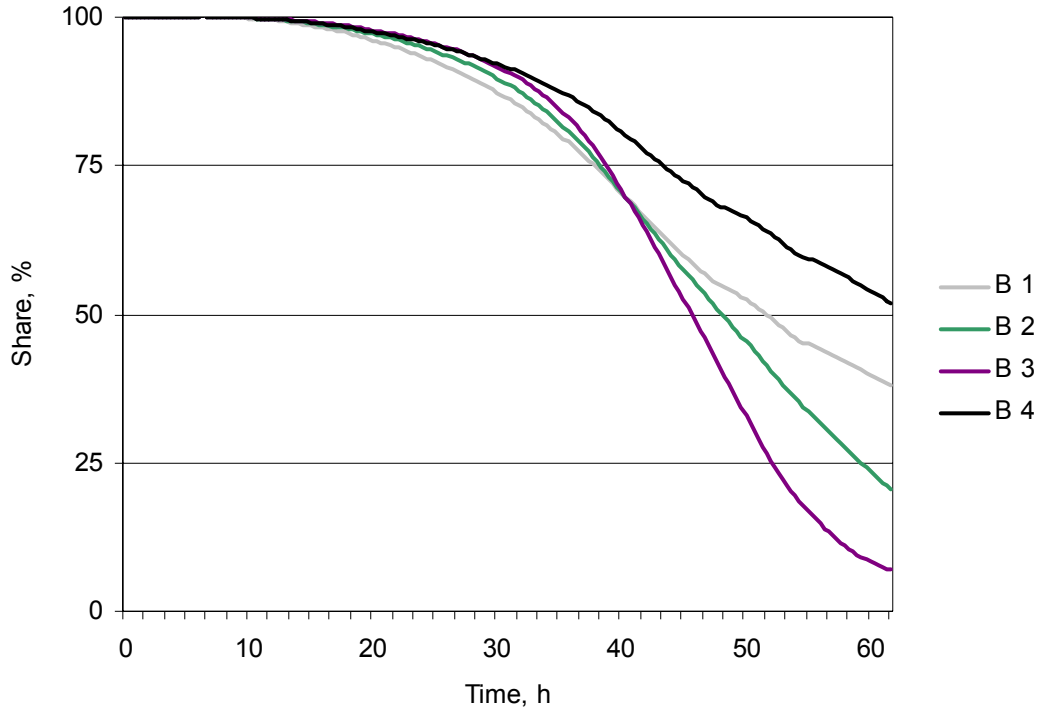

Fig. 3.2. Share of applied current between primary and gassing reactions evaluated using the model and current, voltage and temperature measurements. The charging quickly turns into extensive gassing for the batteries 2 and 3.

3.6.1. Gas Formation

Below, the terms *initial-charge period*, *float-charge period*, *overcharge period* and *voltage scattering* are used as follows.

The initial charging period when constant current is applied is the *initial-charge period*.

The limited charging period between initial-charge and overcharge periods is the *float-charge period*. A constant voltage is applied to limit current in this period.

The inflation or deflation of voltages of single batteries during overcharge is the *voltage scattering*.

The charging period after the scattering of voltages starts is the *overcharge period*.

Oxygen current. All batteries in a string were charged almost completely to reach the state of overcharge. Battery 1 was charged to 99.4 % of maximum capacity, Battery 2 to 99.9 %, Battery 3 to 99.9 %, Battery 4 to 99.4 %. The voltage scattering starts at 98 % of maximum capacity for all batteries. The applied current was nearly equal to the primary reaction current until this point (at 98 %) was reached, from there on the primary reaction current was increasingly more and more compensated by oxygen evolution and recombination current (Fig. 3.3) and, to a lesser amount, by hydrogen evolution current (Fig. 3.4). These secondary processes are less stable; they depend on gas formation and transport through separator.

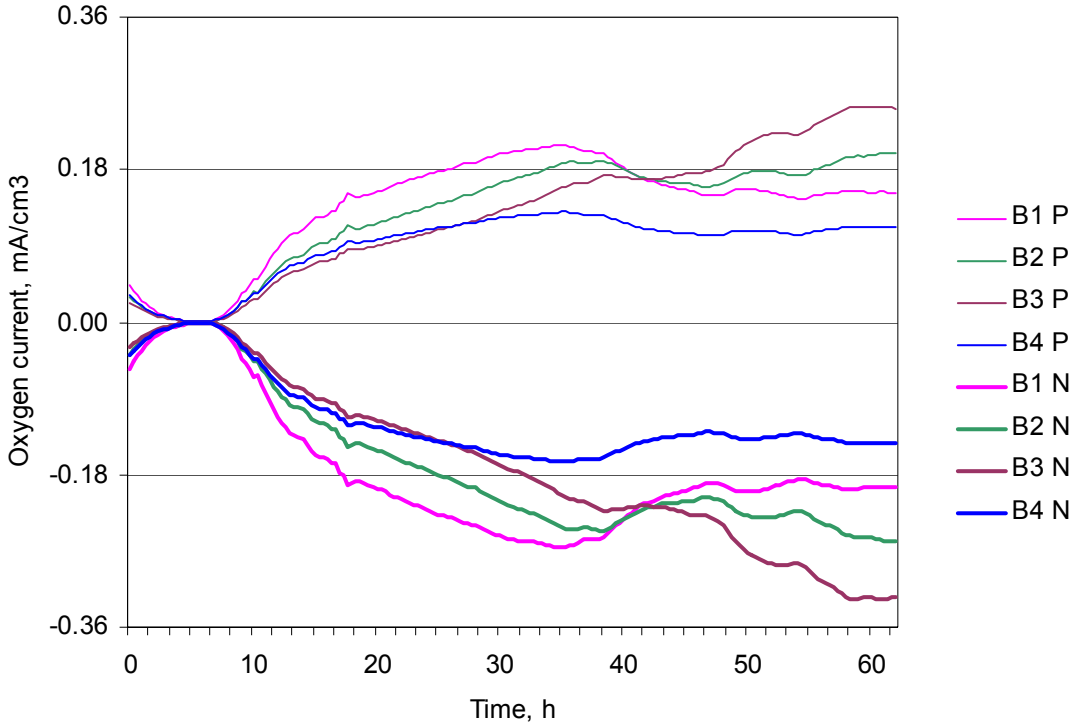

Fig. 3.3. Oxygen evolution and recombination current on positive (P) and negative (N) electrodes (equivalent to 80 – 173 mA/100 Ah at 25˚ C) evaluated using the model and the current, voltage and temperature measurements. Oxygen evolution and recombination processes are well balanced.

Float-charge period. The oxygen evolution and recombination currents are slightly higher for batteries 1 and 4 than for batteries 2 and 3 during float-charge period. This difference cannot be observed directly from measured data, it is masked by high current of the main reaction.

Overcharge period. The oxygen current for battery 3 is higher than for other batteries during overcharge; for battery 2 it has an increasing trend. Difference between the batteries is observable by oxygen current during overcharge, it is large enough for not to be masked by the current of main reaction. The oxygen current can be used for distinguishing between seemingly equal batteries under overcharging.

Hydrogen current. The hydrogen evolution current is slightly higher for batteries 1 and 4 than for batteries 2 and 3 during the float-charge period (Fig. 3.4). This difference cannot be observed directly from measured data – it is masked by high current of primary reaction and/or oxygen reaction. The hydrogen current for batteries 2 and 3 is higher than for other batteries during overcharge. In principle, the hydrogen current

could be used for distinguishing between seemingly equal batteries. However, since it is so small compared to oxygen current, it is better to use the latter for this purpose.

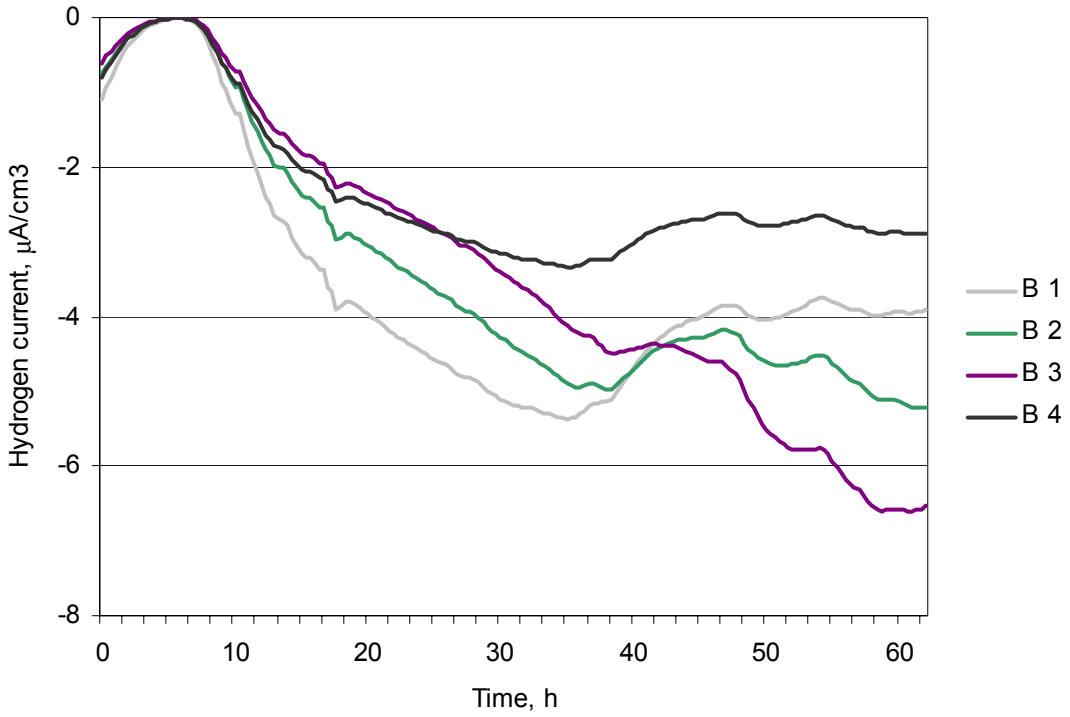

Fig. 3.4. evolution current on negative electrode (equivalent to 1.2 – 2.1 mA/100 Ah at 25˚ C) evaluated using the model and the current, voltage and temperature measurements. This current is much smaller than oxygen evolution current it is equal to the corrosion current (if ORE = 1).

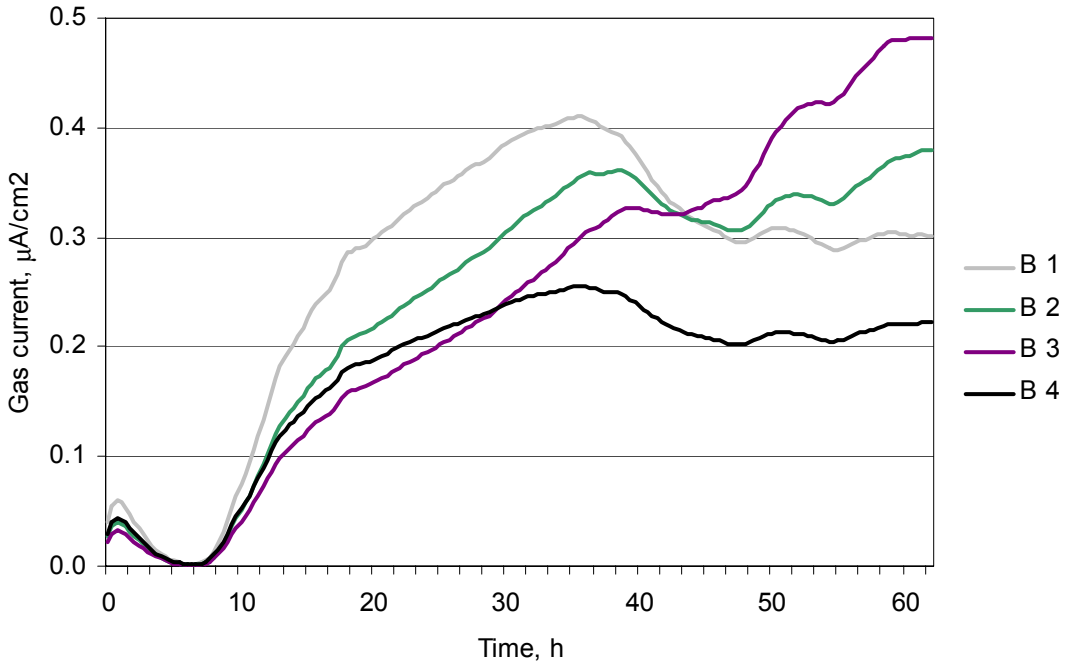

Fig. 3.5. Gas reaction current of tested batteries (equivalent to 1.4 – 2.4 mA/100 Ah at 25˚ C), evaluated using the model and the current, voltage and temperature measurements. This is influenced by difference in evolution of recombination currents.

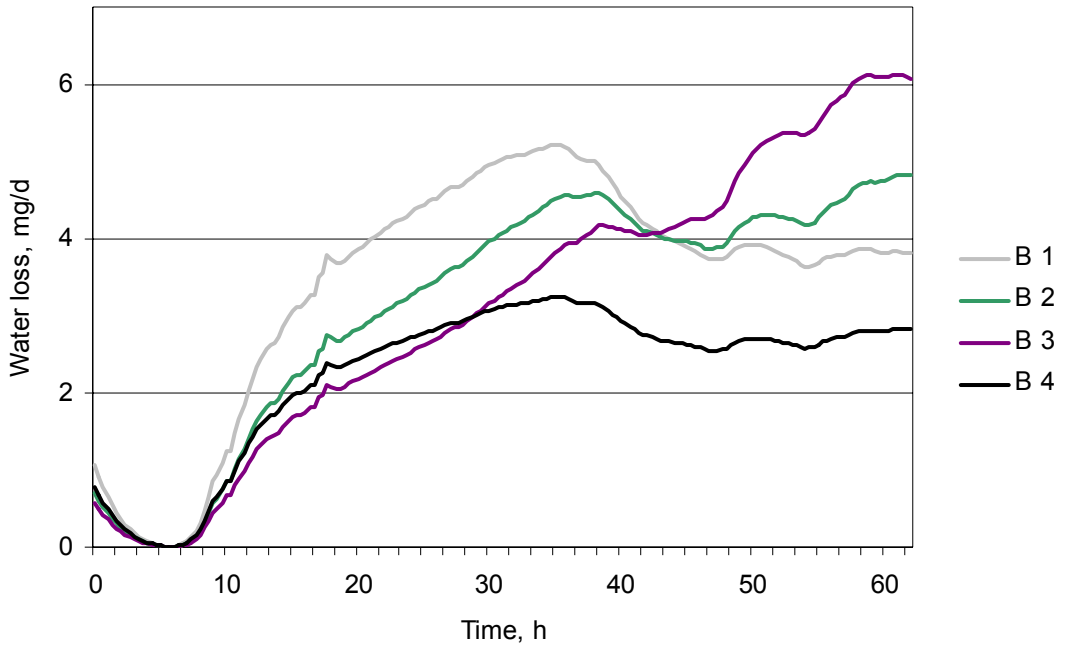

Fig. 3.6. Water dryout evaluated using the model and the current, voltage and temperature measurements (water loss 0.32 - 0.64 % per year at 25° C).

Gas escape and water loss. The gas escape and water dry-out evaluated using the observable current-voltage measurements are shown in Fig. 3.5 and Fig. 3.6. The gas escape is shown as the difference of oxygen evolution and recombination currents plus hydrogen current. The water loss is calculated from the hydrogen current in Fig. 3.6.

Initial-charge period. The gas escape is small during the initial-charge period but it increases substantially during the float-charge period and before or during the overcharge period depending on battery. A high primary reaction current can be produced with relatively low overvoltage during initial-charge period. This overvoltage is not sufficient to produce current of the secondary reactions – they are hindered by the low value of SOC.

Float-charge period. When the charging proceeds at constant voltage, it will be more difficult to produce the current of primary reaction because of reaction hindrance with increased value of SOC. As a result, higher overvoltage should be applied. This produces more current in secondary reactions than in primary reaction. Both oxygen and hydrogen currents are relatively high during the float-charge period.

Overcharge period. In the next period the oxygen evolution current is high but still in good balance with recombination current. As a result, it has little effect on overall oxygen escape, especially considering that the oxygen evolution is a more productive process than hydrogen evolution, especially for high value of SOC. The primary reaction is completely hindered during overcharge. The water loss at the end of charging process is relatively small. Aging of batteries 1 and 4 is smaller during the overcharge than it was during the main charge period.

On an interesting note, the scattering of voltages is not related to electrolyte density or conductivity during overcharge, there are no changes as shown in Fig. 3.7.

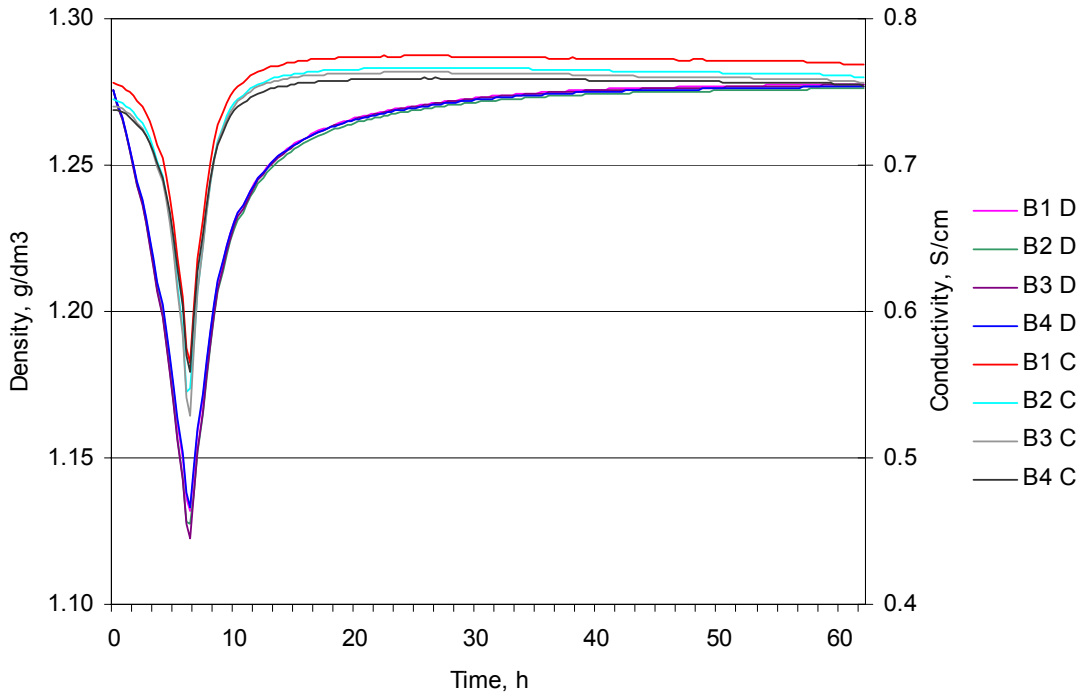

Fig. 3.7. Electrolyte density (D) and conductivity (C) evaluated using the model and the current, voltage and temperature measurements. The scattering of voltages (Fig. 3.1) is not affected by electrolyte concentration or conductivity.

3.6.2. On Relation of Capacity and Overcharge Voltage

Solution of the battery monitoring problem could be simplified if some simple indicators of the state-of-health of battery would be found. Unfortunately, it seems unlikely. In our experiments, it was found that the float voltage during overcharge or resistance cannot be used as simple indicators (for details, see [P6]). It was shown that high float voltage during overcharge can be explained with high ohmic resistance, but no direct link between battery capacity and float voltage or resistance during overcharge was found.

3.7. Conclusion

This chapter presented a modified version of the model introduced in Chapter II. The model was enhanced to take into account the gassing processes that happen in a battery during the whole charge/discharge cycle, but most notably during overcharge.

Ability to evaluate batteries during overcharge – by monitoring gassing currents – gives us the opportunity to reliably monitor the SOH without completely discharging a battery, something that cannot be easily done in UPS systems. This is especially useful considering that simple indicators like float voltage during overcharge or resistance cannot be used as simple indicators of battery health as demonstrated in [P6]. With the help of theoretical model, the unobservable processes in a battery such as

reaction rate, overpotential, current density, porosity, acid concentration, gassing, and water dry-out become visible.

Regarding simple indicators, impedance and conductance measurements have often been touted as solutions. Chapter IV provides some insight into these claims.

Chapter IV

4. Using Impedance to Characterise Battery

4.1. Introduction

When determining battery health, it is natural that methods which may be classified as non-intrusive, i.e., the battery is not discharged, are highly preferred, especially in UPS systems. One of them is the method where the battery impedance or admittance (conductance) is measured and used as a signal representing the SOC and/or SOH. Either voltage or current excitation has been used at frequencies ranging from 10 Hz to 1 kHz in the commercially available impedance/conductance meters [41]. The use of several frequencies (all usually higher than 100 Hz), has also been proposed to improve the information content of the measurements.

It has turned out (see e.g. [18], [19], [38]) that the readings obtained by using the impedance/conductance meters incorporate extensive scattering. Unfortunately, this scattering is largest in the area of SOC where the user's interest is highest, i.e., at 80-100 %. In practice this means that the same reading may equally well correspond to 80 % or 100 % of SOC, causing confusion and reduction of credibility of the method. Typically statistical analysis [19] based on a large number of test samples is needed to distinguish between failed and healthy battery cells or blocks. In reality, there is often no possibility for statistical analysis, because a typical number of battery blocks in series in a telecom UPS system is just four.

The problem lies in the used excitation frequency. It is too high for obtaining readings that would give more information on SOH and/or SOC. It has been shown in [27], [41], [42], [43], [P5] that the impedance at frequencies higher than 1 Hz only includes the impedance of the double-layer capacitor at the negative electrode, and the impedance of the current carrying parts. The impedance values are small, and therefore, highly dependent on measuring noise. This could partly explain the observed high scattering of readings. If the excitation frequency were lowered to mHz level, the contribution from the double-layer impedance at the positive electrode would be included. This would markedly improve the information content because of the decisive role of the positive electrode [11], and may also be in good correlation to SOH and SOC. This chapter will look into this, but from a markedly different point of view.

It should be noted that the explanation given in this chapter is somewhat simplified. For full details, the reader is referred to [P8].

4.2. Contribution

We have developed a method by means of which the battery impedance spectra may be quite accurately predicted based on a battery model derived from the electrochemical processes inside the battery as described in Chapters II and III. Along with the calibrated model, current, voltage and temperature data is used for impedance analysis. The method allows us to analyse both double-layer and faradic processes, visualise entire spectra and attempt to distinguish batteries based on impedance.

The method allows batteries to be modelled at extremely low frequencies, while being free of the limiting assumptions of stationarity of earlier analysis ([14], [26], [27], [41], [42], etc). It ties together the electrochemical battery model and impedance spectra (this is a new approach), allowing the latter to be interpreted as the non-stationary changing of electrochemical processes. Double-layer impedance is also derived from basic processes.

The proposed method, along with the results, is described below.

4.3. Battery Impedance

The processes in an electrochemical battery may be divided into fast and slow processes having time scales in the order of few seconds and hours, respectively. The fast processes are related to the double-layer impedance at positive and negative electrode, and the slow processes to the electrochemical or faradic processes of the same electrodes.

As a dynamic system, a battery may be described by means of an impedance-based small-signal equivalent circuit shown in Fig. 4.1 [21], [30], [41], [42], [49], [43], [50], where C_d represents the double-layer capacitor characterising the double-layer processes, and W the Warburg impedance characterising the faradic processes (note that the designations used later in this chapter are different from those in Fig. 4.1). The value of the double-layer capacitances is large, and therefore, it is obvious according to the equivalent circuit below that the overall impedance at higher frequencies (i.e., > 100 Hz) composes only of L_i and R_i due to shunting effect of C_d. The equivalent circuit parameters of Fig. 4.1 are not constant but dependent on SOH and SOC.

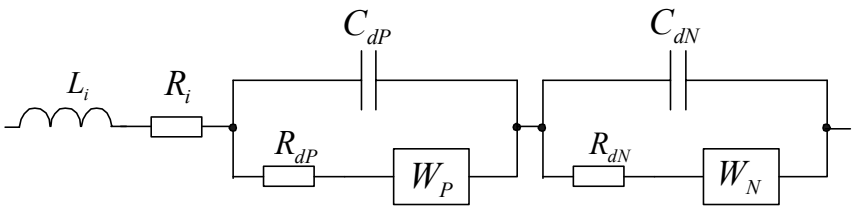

Fig. 4.1. Basic equivalent circuit of electrochemical cell including physical connections (R_i - ohmic resistance, L_i - inductance, R_d - charge-transfer resistance, C_d - double-layer capacitance, W - Warburg impedance, P - positive electrode, N - negative electrode).

The double-layer and faradic (Warburg) impedances [2], [12], [34], [45], [54] do not significantly overlap in frequency and therefore can be analyzed separately, as done in this chapter. The overall impedance may be formed using superposition of the obtained double-layer and faradic impedances.

The earlier battery-impedance analyses based on the equivalent circuit models [21], [30], [41], [42], [43], [49] or electrochemical cell model [14] were based on assumptions that could adversely affect the accuracy of predictions: 1) linear response, 2) stationarity during measurements, and 3) open-circuit condition. In papers [P5], [P7], [P8], linearity and stationarity are not required and any dc current can be applied.

4.4. Double-layer Impedance

On the interface between solid and liquid phases in a porous electrode, a mini-charge will build up that remains constant as long as the applied current is constant. This mini-charge is unrelated to the battery capacity or charge produced by the electrochemical reaction. Fast battery dynamics are induced by change of the applied current, which in turn induces a change in the mini-charge of double-layer. This change is shown as the voltage-drop response to the current pulses in Fig. 4.2. The voltage-drop is considered with respect to the thermodynamic equilibrium voltage that can be measured during zero applied current.

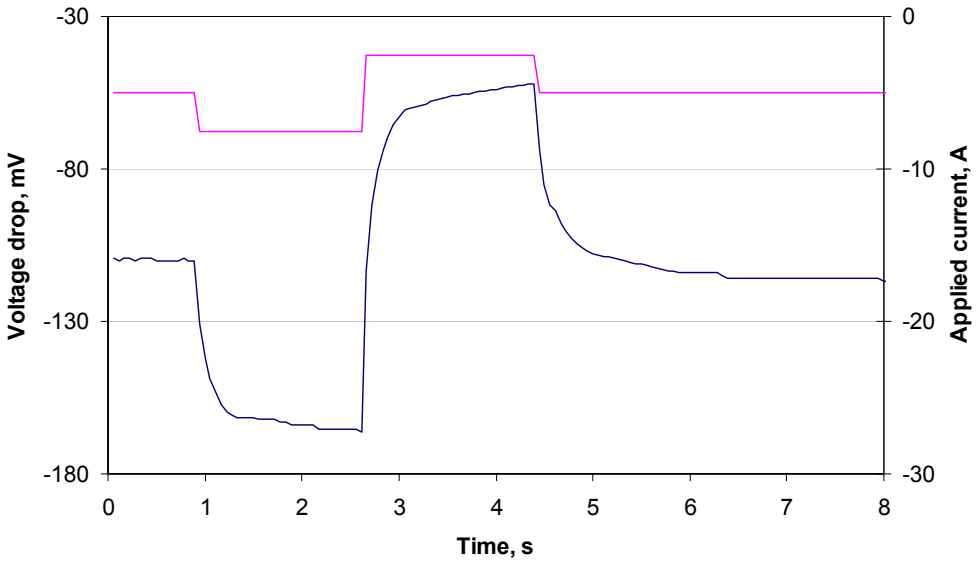

Fig. 4.2. Voltage-drop response (lower curve) to current pulses.

The ratio between voltage-drop and applied current is a dynamic process (Fig. 4.3), addressed here as the dynamic resistance of the battery. Several methods can be used to characterise a battery through its dynamic resistance using model, time response or frequency response characteristics.

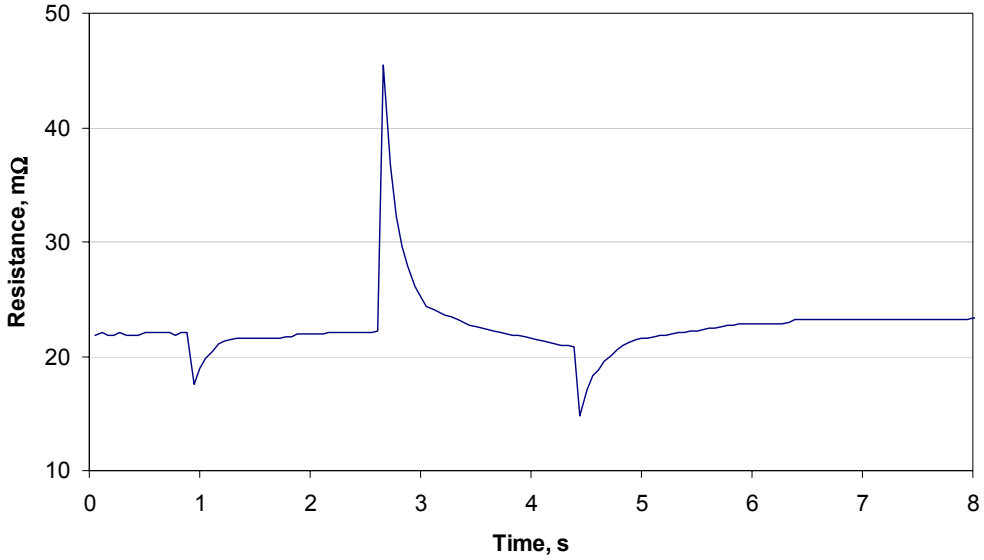

Fig. 4.3. Dynamic resistance as the ratio between voltage-drop and current pulses shown in Fig. 4.2.

1. Time response. A battery can be characterised through voltage-drop curve obtained as the response to current pulses. This characteristic can be easily measured, but is inconvenient for practical use since it requires expert knowledge in the form of reference data for comparison.

2. Model. The double-layer capacitance can be charged or discharged rapidly according to the following model (without dynamics this is Ohm's law)

$$r_{ct}c_{dl}\frac{d\eta}{dt} = w(r_0 + r_{ct}) - \eta, \quad \eta(t_0) = \eta_0, \tag{4.1}$$

where
t_0 - initial moment chosen for analysis, sec,
t - time in a few seconds range, sec,
η - surface overpotential, V,
w - applied volumetric current density, A/cm^3,

$$w = \frac{I_{app}}{hS_p}, \quad w = w_M + w_{byp},$$

I_{app} - applied current, A,
h - thickness of porous electrode, cm,
S_p - plate area, cm^2,
w_M - faradic primary reaction current: volumetric current density, $w_M = Aj_M$, A/cm^3,
w_{byp} - capacitive bypass current through capacitor, $w_{byp} = w - Aj_M$, A/cm^3,
r_{ct} - charge-transfer local resistance, $r_{ct} = r_{ct}(t_0)$, Ωcm^3; it is equal to the specific resistance of electrode material (with unit Ωcm) if divided by plate area,
r_0 - conducting elements local resistance, $r_0 = r_0(t_0)$, Ωcm^3,
c_{dl} - double-layer specific capacitance, $c_{dl} = c_{dl}(t_0)$, F/cm^3. It is defined as a volumetric charge density, i.e. electrode capacity per volume.

The faradic-current and capacitive-current can be expressed as the overall applied current, whereas specific capacitance and local resistances are expressed as overall parameters for the electrode. This simplifies model (4.1) giving

$$R_{ct}C_e\frac{d\eta}{dt} = I_{app}(R_0 + R_{ct}) - \eta, \quad \eta(t_0) = \eta_0, \tag{4.2}$$

where
R_{ct} - electrode charge-transfer resistance, $R_{ct} = r_{ct}/hS_p$, Ω,
R_0 - conducting elements resistance, $R_0 = r_0/hS_p$, Ω,
C_e - electrode capacitance, $C_e = c_{dl}hS_p$, F,
S_p - plate area, cm^2,
h - thickness of electrode, cm.

The charge-transfer resistance depends on the specific resistance of electrode material and other conducting elements. The conducting elements resistance depends on the specific conductivity of acid and other materials in current pathways. The double-layer capacitance depends on the utilization of the electrode through active surface area A as a constant dependent on the SOC: $A(\theta(t_0))$.

The surface overpotential is induced by slow and fast components, $\eta = \eta_0 + \eta_f$. The slow component η_0 is induced by electrochemical processes $\eta_0 = I_0(R_0 + R_{ct})$ and the fast component by charging or discharging of the double-layer capacitance, $\eta_f = \eta - \eta_0 = \Delta\eta$.

The charging rates of double-layer are essentially different for positive and negative electrodes. A good agreement with experimental data can be obtained on the basis of model (4.2) if it is applied as a two-rate model, differing for electrodes. The model-predicted voltage-drop is compared with measured data in Fig. 4.4. They are almost identical, as are their modifications – the dynamic resistances. The model error is small in few seconds range, but it increases significantly in the longer term due to the electrochemical reaction.

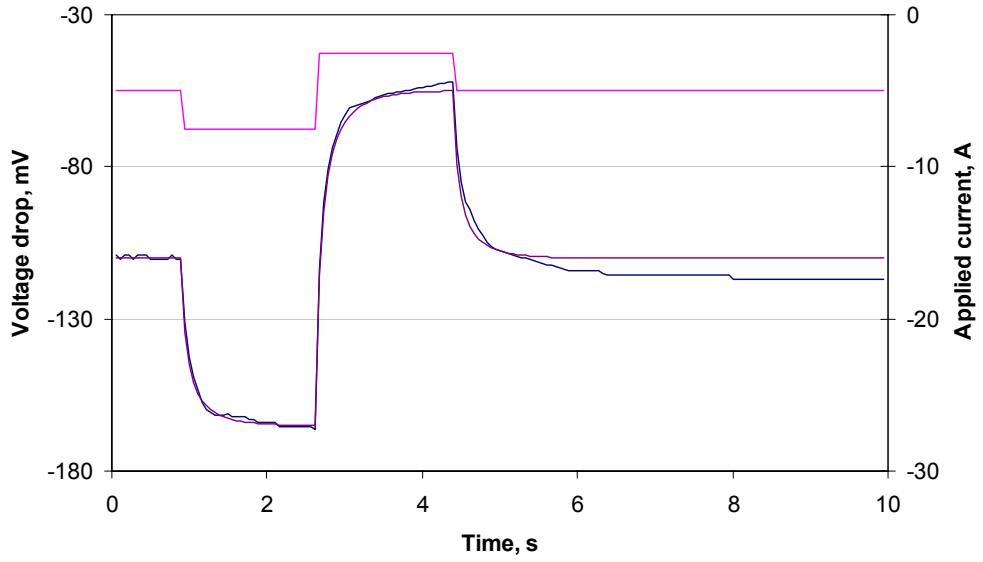

Fig. 4.4. Measured (lower curve) and model-predicted (middle curve) voltage-drop.

3. Frequency response. The double-layer frequency response can be obtained as a Fourier transform of the dynamic resistance (actually, it is somewhat more complicated [9], but convolution is left out of presentation for simplicity)

$$Z(\omega) = \frac{\mathbf{F}\ \eta(t)}{\mathbf{F}\ I_{app}(t)} = \frac{\int_{-\infty}^{\infty} \eta(t) e^{-j\omega t} dt}{\int_{-\infty}^{\infty} I_{app}(t) e^{-j\omega t} dt}, \tag{4.3}$$

where
F - Fourier transform (operator),
R(t) - battery dynamic resistance, Ω,
Z(ω) - battery complex resistance or impedance, Ω,
j - imaginary unit, $j = \sqrt{-1}$,
ω - angular velocity, rad; $\omega = 2\pi f$, f - frequency, Hz.

This transform (4.3) for both electrodes can be calculated on the basis of model (4.2) as

$$Z(\omega) = R_0 + \frac{R_1}{1 + j\omega R_1 C_1} + \frac{R_2}{1 + j\omega R_2 C_2}, \tag{4.4}$$

where
C_i - double-layer capacitance for positive $C_1 = C_e^+$ or negative $C_2 = C_e^-$ electrodes,
R_i - charge-transfer resistance for positive $R_1 = R_{ct}^+$ or negative $R_2 = R_{ct}^+$ electrodes,
R_0 - total resistance of conducting elements; it includes resistance of electrodes and separator, grid resistance, inter-cell connector resistance and battery terminals resistance.

The obtained double-layer impedance (4.4) allows interpretation of the results through the theoretical model and its adaptation to the electrochemical process changes. This type of adaptation of fast process impedance to slow process time-variable changes is is known [61] as a pseudo-stationary approach and frequently used in practice.

This formula (4.4) for equal (overall) electrodes is typical in many papers [30], [50].

The complex resistance (4.4) evaluated on tested batteries is shown as Nyquist and Bode diagrams in Fig. 4.5 and Fig. 4.6, respectively.

The double-picks shown in both diagrams were observed on tested batteries. The first arc of the curve in Fig. 4.5 is for the negative electrode and the second arc for the positive electrode. If charge-transfer resistances were equal, both arcs would be equal in size but different in distribution of the frequency points on the curve. High frequency points are more concentrated at the origin. Lower capacitance also moves them closer to the origin. The first peak of the phase-angle in Fig. 4.6 is observed at low frequency of about 1 Hz; it is for positive electrode. The second peak is observed at higher frequency of about 10 Hz; it is for negative electrode. The absolute value of the complex resistance (modulus) is rather small at higher than 10 Hz frequencies.

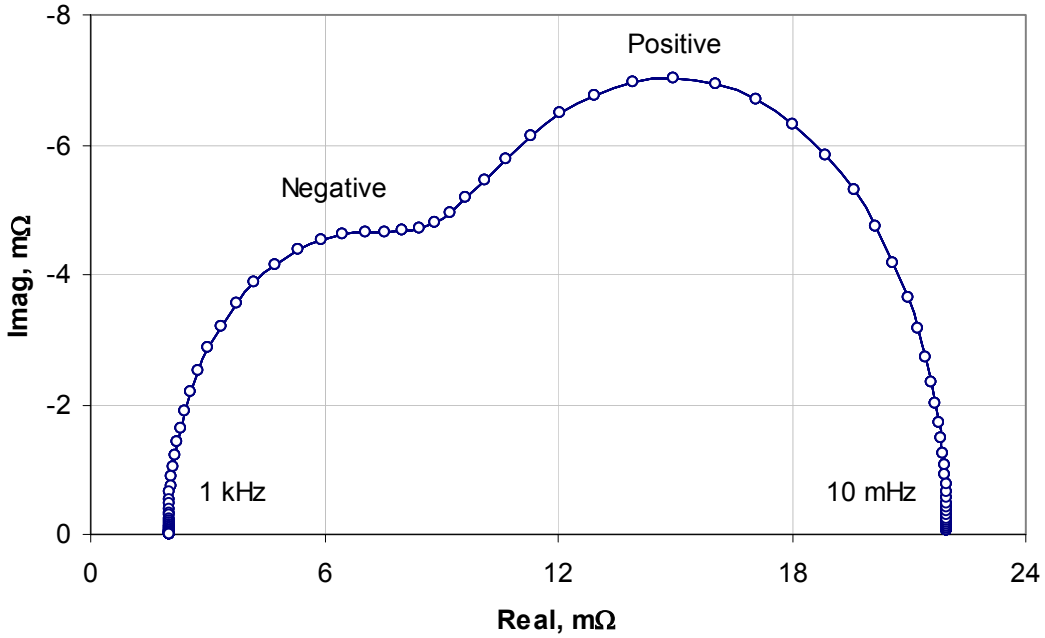

Fig. 4.5. Battery double-layer impedance.

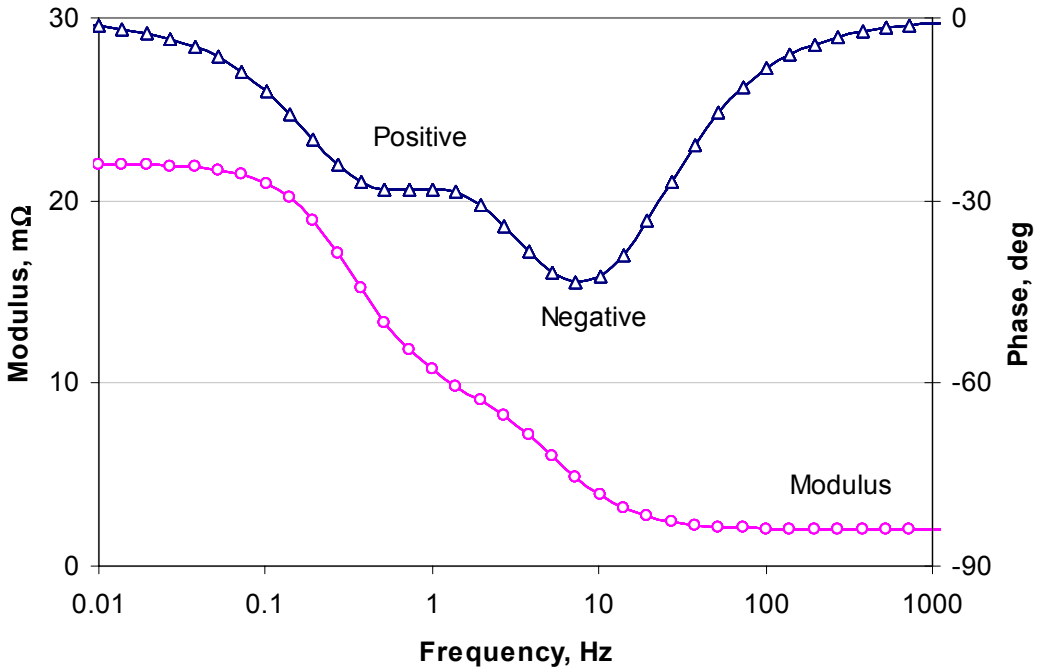

Fig. 4.6. Battery double-layer frequency response: modulus (lower curve) and phase-angle (upper curve). The left-side pick of phase-angle at lower frequency is for positive electrode and right-side pick for negative.

The double-layer impedance depends strongly on the SOC and other parameters of the electrochemical reaction. This dependence can be accounted for through adaptation of the parameters of (4.4) to more complex cell model represented in Chapters II and III. The impedance curves adapted to the state of electrochemical reaction are shown in Fig. 4.7 and the frequency response curves in Fig. 4.8. The characteristics of four batteries are shown for discharge at SOC = 99, 57, and 16 %.

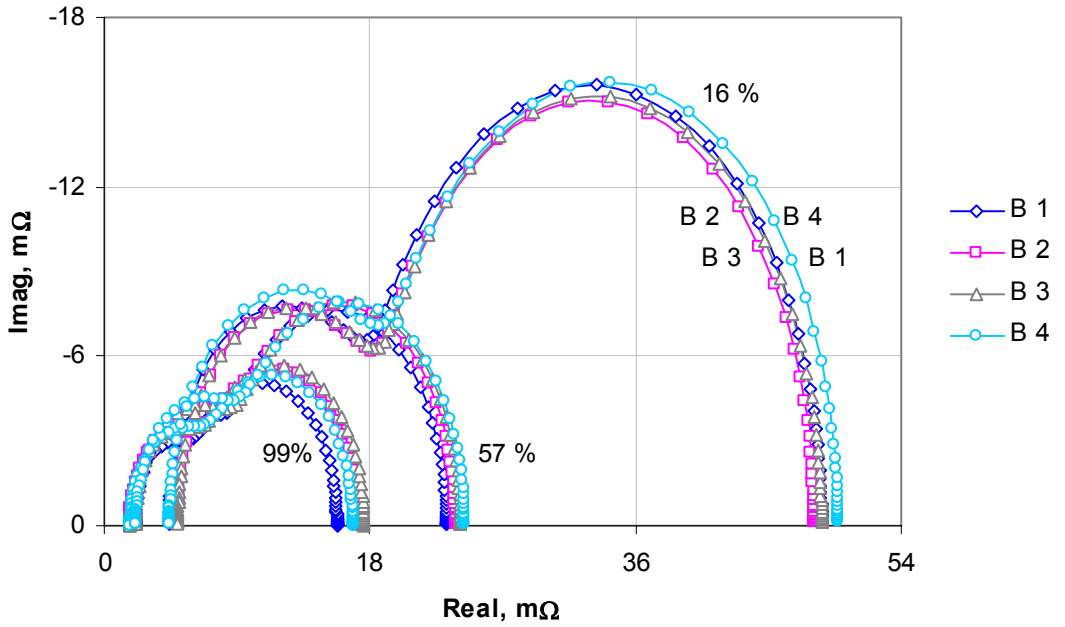

Fig. 4.7. Batteries B1-B4 double-layer impedances shown for discharge at SOC = 99, 57, and 16 % in wide range of frequencies (1 mHz-12 kHz). The double-layer impedance is affected strongly by SOC-level. Small inequalities between batteries cannot be detected by this characteristic.

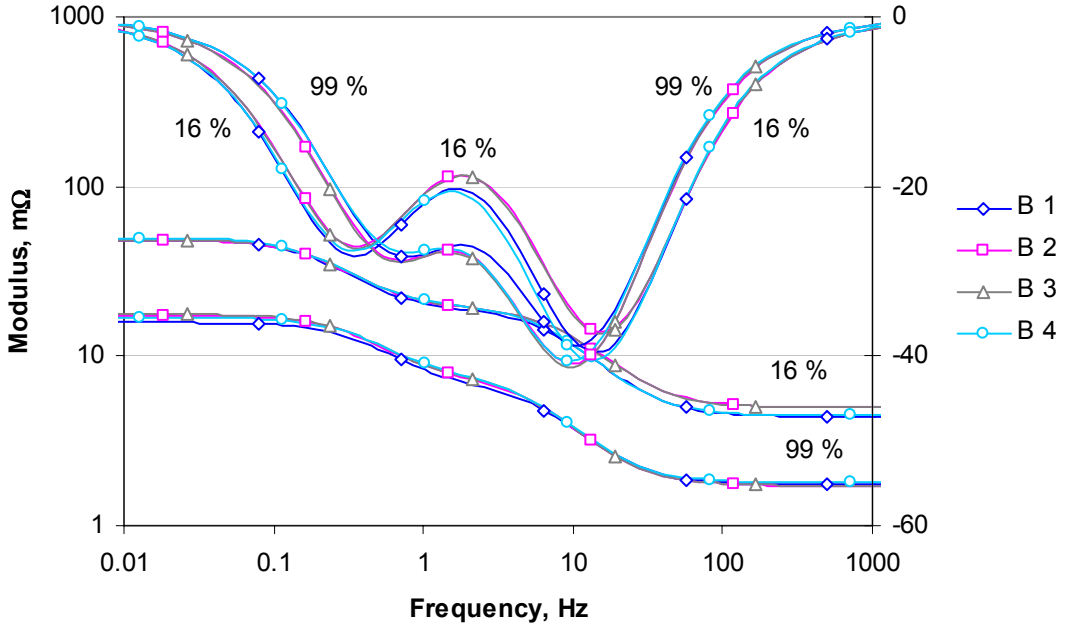

Fig. 4.8. Batteries' double-layer frequency responses for discharge, represented as equivalent characteristics to the impedances shown in Fig. 4.7 through absolute values and phase-angles. The phase-angles are less sensitive to SOC than modulus or impedance.

These characteristics are dependent on the electrochemical reaction so strongly that some constant frequency level for detection of weak batteries, by measured impedance, cannot be chosen, especially if impedance is measured in single point at high frequency. The use of multiple frequencies and simultaneous comparison with other batteries may help, but not much. In fact, the double-layer impedance is not sensitive indicator of weak batteries even if complex cell model is used to calculate battery ref-

erences. This is shown in Fig. 4.7 and Fig. 4.8 for four batteries with slightly different capacity: 36 Ah – batteries 1, 4 vs. 34 Ah – batteries 2, 3. These batteries cannot be easily distinguished by double-layer impedance at any state of the electrochemical reaction. The situation is not better during charge either – see Fig. 4.9 (overcharge is a special situation [P8] not shown in this figure).

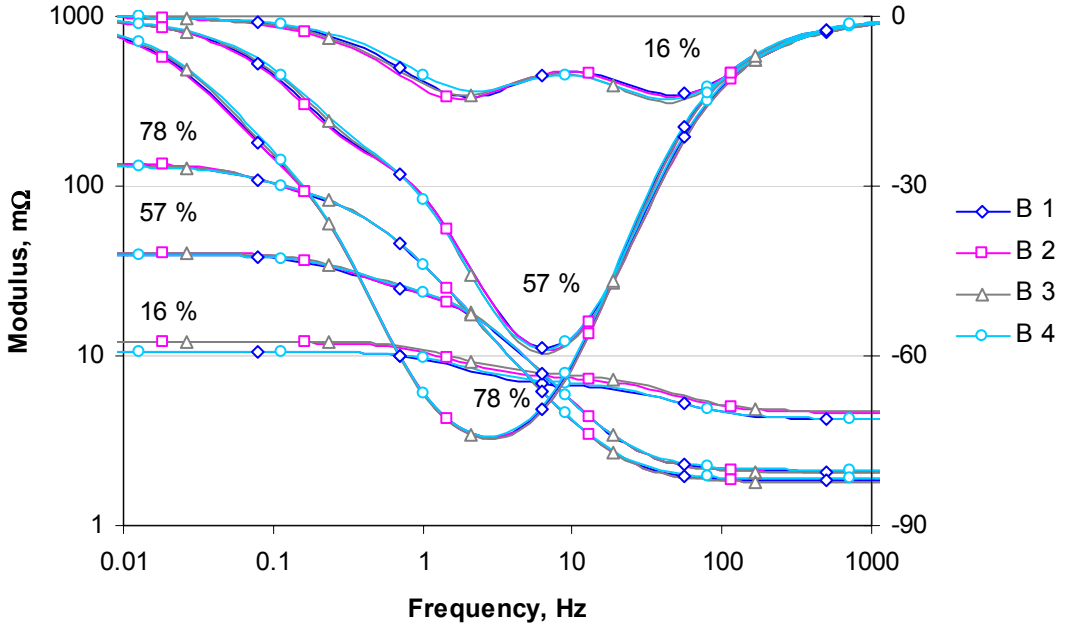

Fig. 4.9. Batteries' double-layer frequency responses for charge The phase-angles are more sensitive to SOC than modulus.

The double-layer impedance (Fig. 4.5-Fig. 4.9) evaluated on the tested batteries by current-voltage and temperature measurements using the model-based method (see Chapters II and III for information on test conditions and model calibration) is quite similar to the results obtained by other authors [21], [30], [41], [42], [43], [50] using conventional methods.

4.5. Electrochemical Impedance

The electrochemical or faradic impedance is reaction-dependent impedance that characterises slow faradic processes in a battery, typically corresponding to frequencies lower than 100 μHz.

Battery impedance and electrochemical reaction are related through Fourier transform for the complex processes described by the electrochemical cell model (see Chapters II and III). The process of deriving the model for impedance from the electrochemical reaction is outlined below.

4.5.1. Impedance Model

To evaluate battery impedance, a Fourier transform of the model described in Chapters II and III needs to be performed. For this, first, the model is solved analytically for the lumped parameter case, and then the results used to derive a formula for surface overpotential. These are then applied to derive the model for impedance.

The approach is based on the use of Fourier transforms in such a way that the battery discharge current, and the resulting voltage drop, i.e., the surface overpotential, are assumed to be single pulses for which the corresponding Fourier transforms may be defined. The electrochemical impedance or its spectra may be presented as a ratio of the voltage pulse and current pulse transforms. The discharge time is considered to be a forecast period. It is obvious that the longer the forecast period is, the better the slow processes are characterized. This is equivalent to the depth of discharge.

The typical forms of the excitation and response pulses are shown in Fig. 4.10 and Fig. 4.11.

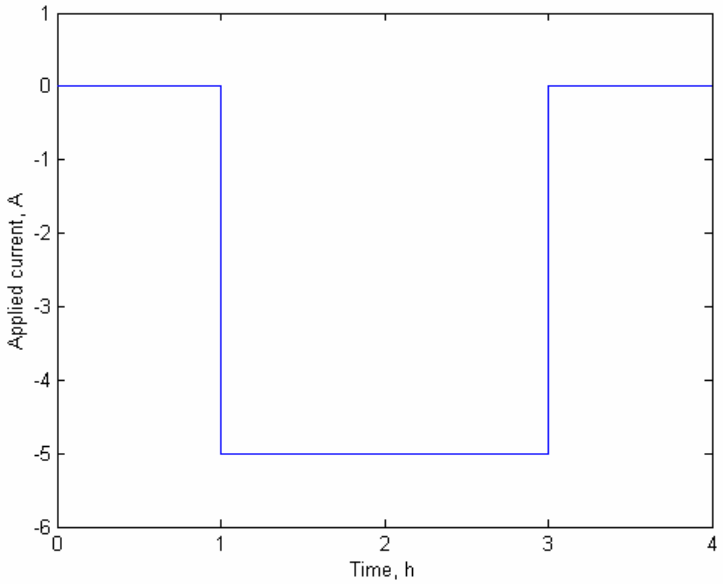

Fig. 4.10. Discharge current pulse used as an excitation at moments t_0 = 1h lasting T_0 = 2h.

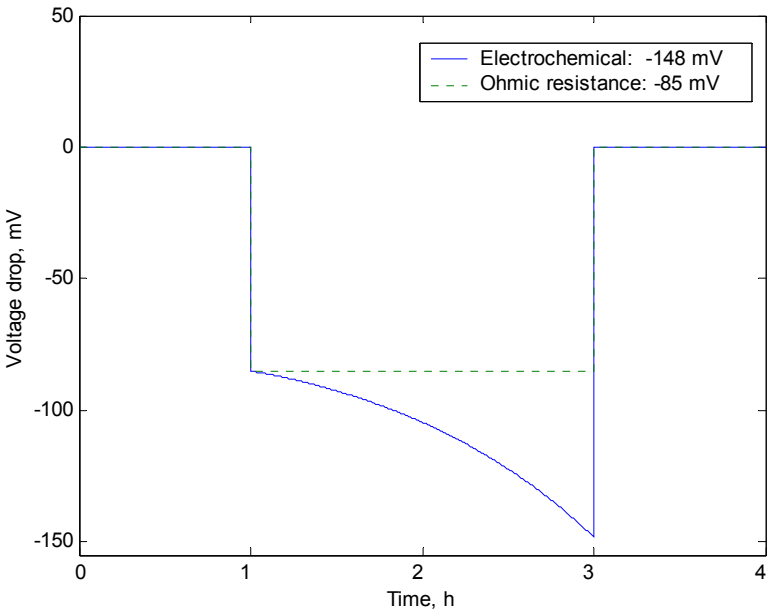

Fig. 4.11. Resulting surface overpotential.

The solution of the model is simple if the volumetric current density is distributed uniformly and expressed through the applied current, which is a simple test signal as shown above. If the volumetric current density can be assumed to be distributed uniformly (i.e., $w_M(x) = w_M$) then the applied current is directly proportional to the volumetric current density according to

$$w_M = \frac{I_{app}}{hS_p}, \tag{4.5}$$

where
w_M - volumetric current density of primary reaction, A/cm^3,
h - thickness of porous electrode (constant), cm,
S_p - plate surface area (constant), cm^2,
I_{app} - applied current (virtual test signal), A.

It is assumed that the charge/discharge rates are relatively slow. Thus the gassing in the electrodes is insignificant and the drop of acid density in the electrodes is well compensated by diffusion of fresh acid from separator. These relaxed conditions are removed in [P8].

Simplified model. Assume that the applied dc current I_0 drives the electrochemical system (2.1)-(2.10) to a state (θ_0, ε_0, c_0) at the current moment t_0. After this moment, applied current $I_{ap.0}$ drives it further in interval $t_0 \le t \le t_0 + T_0$ and dc current I_0 beyond that interval. Evolution of the system in the interval depends on the initial state (θ_0, ε_0, c_0) only. It is independent of the events before the current moment and also independent of the dc current applied. Therefore, zero dc current can be assumed, meaning that a battery is at rest outside the interval $0 \le s \le T_0$, $s = t - t_0$. The evolution process in the interval $[t_0, T_0)$ can be expressed as the lumped parameter modifications of (2.4), (2.9) and (2.10)

$$d\theta = \frac{\alpha_{Ah}}{Q_{max}} w_M \, ds, \qquad \theta(t_0) = \theta_0, \tag{4.6}$$

$$d\varepsilon = K_1 w_M \, ds, \qquad \varepsilon(t_0) = \varepsilon_0, \tag{4.7}$$

$$\varepsilon dc = (K_2 - cK_1) w_M \, ds, \quad c(t_0) = c_0, \tag{4.8}$$

where
$w_M = I_{ap.0}/hS_p$ - constant, A/cm^3,
$I_{ap.0}$ - current pulse amplitude, A,
t_0 - initial moment for analysis, sec,
T_0 - forecast period: current pulse width, sec.

This system (4.6)-(4.8) can be viewed as an electrochemical reaction description (in the case of lumped parameter model) or a single layer reaction description (in the case of distributed parameter model [P8]).

Solution. The system (4.6)-(4.8) can be solved analytically using the method of integration by the separation of variables. The solution of the system can be expressed through the time-dependent functions as

$$\theta(s) = \theta_0 + \frac{\alpha_{Ah}}{Q_{max}} w_M s, \tag{4.9}$$

$$\varepsilon(s) = \varepsilon_0 + K_1 w_M s, \tag{4.10}$$

$$c(s) = \frac{c_0\varepsilon_0 + K_2 w_M s}{\varepsilon_0 + K_1 w_M s}. \tag{4.11}$$

The functions (4.9)-(4.11) can be applied to derive another time-dependent function – surface overpotential – from simplified electrode reaction equation as follows.

Simplified electrode reaction. The exact formula of electrode reaction (2.5) can be approximated as a simple hyperbolic function

$$j_M = 2i_0^M \mu^{\beta 2} \mathrm{sh}(\alpha k \eta), \tag{4.12}$$

where
μ - dimensionless acid concentration, $\mu = c/c_{ref}$,
k - constant, $k = F/RT$.

Here, the difference of two exponential functions $e^x - e^{-ax}$ with unequal growth rates ($a \leq 1$) is approximated with a hyperbolic function $2\mathrm{sh}\, ax = e^{ax} - e^{-ax}$. This approximation is justified as follows. The sum of two exponents is close to the one whose growth rate is faster by absolute value. It is essentially supreme if the overpotential is shifted far away from the equilibrium potential. This takes place for large dc current. For zero dc current (shift zero), the approximation error is zero. These simple ideas are applied for the parameterisation of the simplified electrode reaction (4.12) as follows.

- On positive electrode, anodic apparent transfer coefficient $\alpha = \alpha_c$ should be applied for discharge reaction and cathodic coefficient $\alpha = \alpha_a$ for charge reaction.
- On negative electrode, $\alpha = \alpha_a$ can be applied for discharge reaction and $\alpha = \alpha_c$ for charge reaction.
- For battery at rest (close to the equilibrium voltage), symmetric kinetics $\alpha = 1$ should be applied.

The transfer current density (4.12), multiplied by surface area (2.2 and 2.3), and expressed as the volumetric current density (4.5) – which is constant for applied current in this work – gives the following formula

$$w_M = 2i_0^M A(\theta(s))\mu(s)^{\beta 2} \mathrm{sh}\{\alpha k \eta(s)\}. \tag{4.13}$$

The surface overpotential is an argument of function (4.13) – it depends on time through the solutions of (4.9)-(4.11) of the system (4.6)-(4.8).

Surface overpotential. The volumetric reaction rate Eq. (4.13) can be solved with respect to surface overpotential as a logarithmic function

$$\eta(s) = \frac{\ln(y + \sqrt{y^2 + 1})}{\alpha k}. \qquad (4.14)$$

Here, y is the ratio between the volumetric current density and the exchange current density, corrected with the current values of the effective surface area and acid concentration

$$2y = \frac{w_M}{A(\theta(s))i_0{}^M \mu(s)^{\beta 2}}. \qquad (4.15)$$

Formula (4.14) is an inverse hyperbolic function arsh $y = \ln(y + \sqrt{y^2 + 1})$ of (4.13).

Simple formula for overpotential. It seemed that the curve for surface overpotential is a complicated function of time by the analytical formulas (4.14), (4.15), (4.9)-(4.11), but actually, it is not. The curve drawn for constant current by numerical data is a simple function that can be approximated well (see Fig. 4.12) with the following exponential power series:

$$\eta_a(s) = a_0 \exp(a_1 s^1 + a_2 s^2 + \ldots + a_n s^n), \quad 0 < s < T_0, \qquad (4.16)$$

with coefficients (a_i) adapted to the charge or discharge curve along the evolution of SOC.

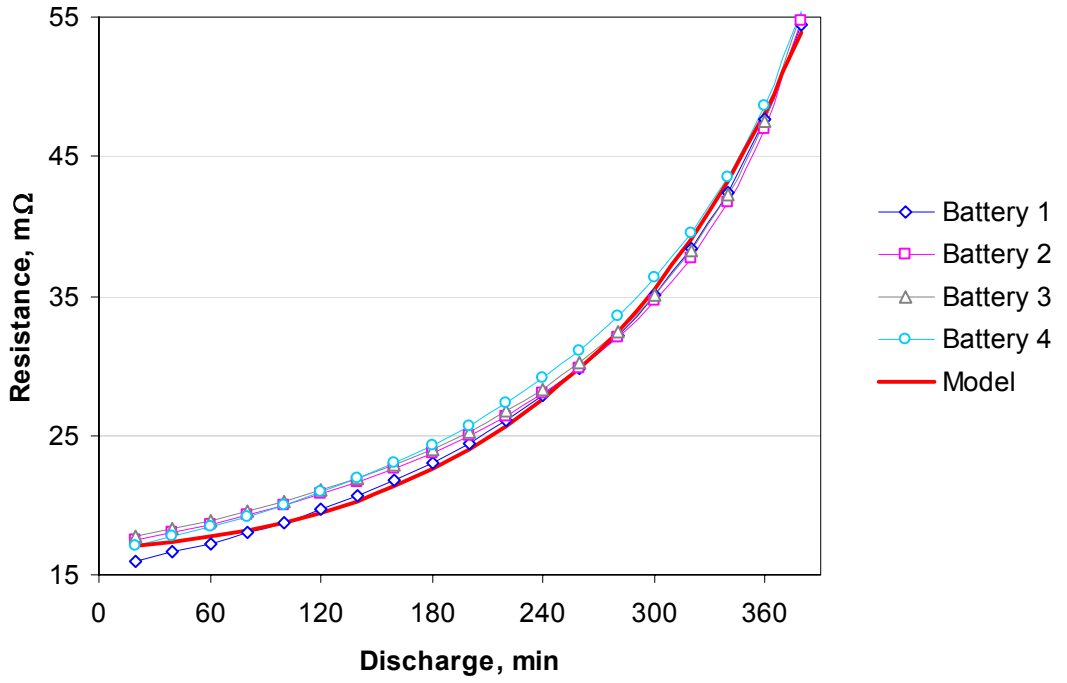

Fig. 4.12. Measured resistance on batteries 1-4, compared with resistance predicted by the second order exponential power series model with coefficients $a_1 = 0.015\ h^{-1}$, and $a_2 = 0.026\ h^{-2}$. Even for period this long (6 h), the second order power series is acceptable model; for a shorter period (2 h), it is almost ideal fit for any battery.

It was found in numerical analysis that analytical solution (4.14) could be approximated sufficiently precisely with second order power series. The approximation coefficients can be evaluated (by means of the surface overpotential calculated from the

cell model according to current, voltage and temperature measurements) from the regression (non-linear, but linear by parameters) $\ln \eta(s) = \ln(a_0) + a_1 s + a_2 s^2$ using computationally effective least square method.

It is only natural that overpotential can be represented as an exponential power series (4.16), remembering that constant applied current can be achieved by increasing overpotential slowly for well-charged battery and rapidly for discharged battery.

The approximation formula (4.16) for overpotential can be used in the case of constant current. In the case of normal constant-current/constant-voltage charging the approximation formula should be applied in both intervals of charging separately.

Calculating impedance. The electrochemical impedance can be calculated as a Fourier transform of the dynamic resistance observed during long period. Real calculations should be performed separately for overpotential and applied current to make the Fourier analysis consistent as shown below

$$Z(\omega) = \frac{\mathbf{F}\,\eta(t)}{\mathbf{F}\,I_{app}(t)}, \qquad (4.17)$$

where

η - surface overpotential, V, approximated by second order version of exponential power series (4.16)

$$\eta(t) = a_0 \exp(a_1 t + a_2 t^2), \quad 0 < t < T_0,$$

a_i - coefficients adapted to the current state of reaction $a_i = a_i(t_0)$ at moment t_0, $\sec^{-i}$,
I_{app} - applied current - long pulse of length T_0 used as test signal, A,
T_0 - forecast period, sec.

The adapted coefficients are an implicit representation of the electrochemical cell model in a compact form. They depend on almost every process in a battery – as does impedance.

The Fourier transforms for surface overpotential and impulse current (test signal) can be calculated analytically. The final result – complex resistance of electrochemical reaction – can be expressed (Table III, Section 10.10 in [48]) as the following function

$$Z(\omega) = R_0 + \left\{ \frac{a_0 \exp\{a_1 T_0 + a_2 T_0^2 - j\omega T_0\}}{a_1 + 2a_2 T_0 - j\omega} - \frac{a_0}{a_1 - j\omega} \right\} \frac{j\omega}{I_{ap.0} - I_{ap.0} \exp(-j\omega T_0)}, \qquad (4.18)$$

where

$Z(\omega)$ - impedance, Ω,
$I_{ap.0}$ - current pulse amplitude of virtual test-signal, A,
T_0 - forecast or predictive-analysis period, s; i.e. the period that Fourier analysis is set up to see the battery behaviour ahead by applied method. The longer the forecast period is, the better the slow processes are characterized. This is equivalent to the depth of discharge.

Here impedance (exponential function) is a periodic function [P8], which is a result of Gibbs phenomena (oscillation at pulse coners) [48].

4.5.2. Experiment and Calculations

As in previous chapters, the cell model was calibrated in a way that it predicts charge/discharge behaviour rather well, using current, voltage, and temperature data recorded in real-life experiment [58]. The calibrated model was applied to evaluate the surface overpotential during charge/discharge processes. The surface overpotential was used to evaluate coefficients of the exponential power series of (4.16) at any chosen moment. Using coefficients impedance calculation is a simple application of the formula (4.18). No direct measurements of impedance were made at any frequencies. The forecast period T_0 was 2 h and the current 5 A (see Fig. 4.10 and Fig. 4.11).

The electrochemical impedance for the positive and negative electrodes are shown for discharge of SOC = 99, 57, 16 % in low frequency range of 1-80 μHz in linear frequency scale in Fig. 4.13, Fig. 4.14, and Fig. 4.15. They were evaluated on four batteries in a string.

The electrochemical impedance depends strongly on SOC. Its real and imaginary parts are widely spread over the plot of complex resistance for deeply discharged battery, as shown in Fig. 4.13, Fig. 4.14, and Fig. 4.15. In addition to this effect, inequality between the batteries is well observable. The impedance curves are packed tightly in two groups: batteries 1, 4 and 2, 3 (as is their actual capacity: 36 Ah versus 34 Ah), especially for deep discharge at low frequency.

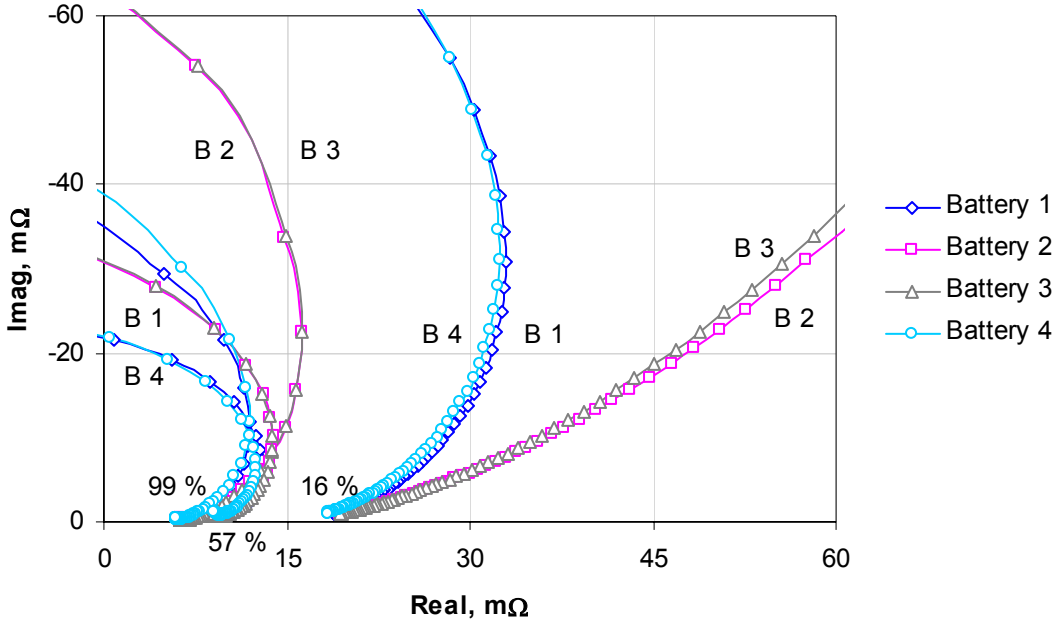

Fig. 4.13. Positive electrode impedance shown for discharge of SOC = 99, 57, and 16 %. The curves for similar batteries 1, 4 and 2, 3 are closer to each other.

The positive electrode impedance (Fig. 4.13) is several times larger than the impedance for the negative electrode (Fig. 4.14) in terms of both components: real and imaginary. The overall impedance of both the electrodes and separator, i.e. the elec-

trochemical cell (Fig. 4.15), is close to the positive electrode impedance with the exception of being more warped.

The rapid growth is generally accepted as the shape of impedance for the positive electrode: [12], [45], [30], [39], [41], [42], [43], [44]. The slope of growth varies from some degree to vertical and over, depending on a paper. A weak counter-clockwise oriented spin was measured experimentally in mHz range in [44].

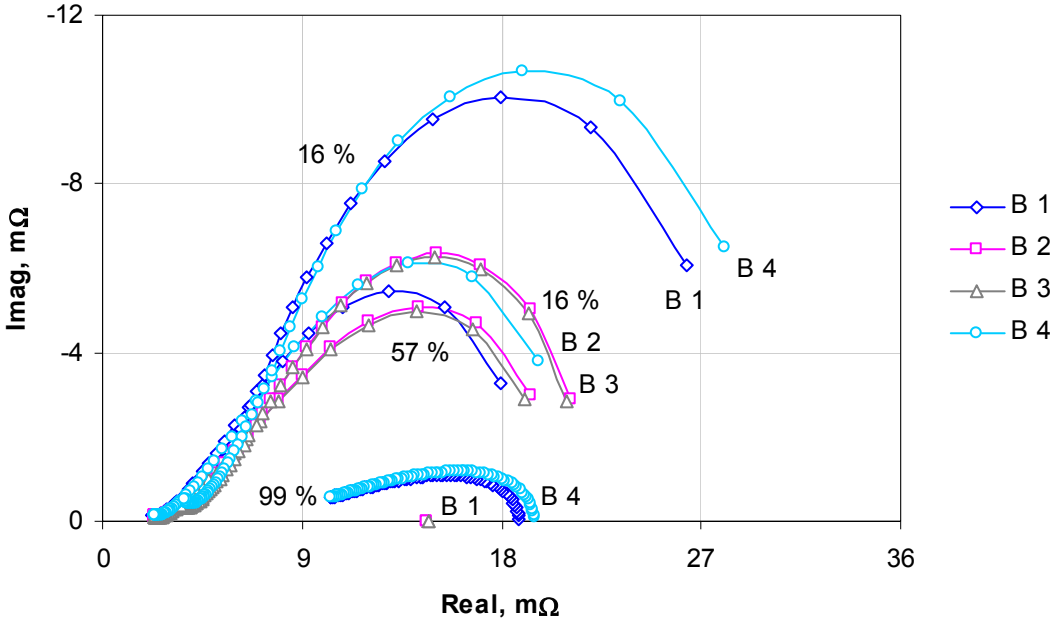

Fig. 4.14. Negative electrode impedance shown for discharge of SOC = 99, 57, 16 %. The curves for similar batteries are grouped: batteries 1, 4 – higher branches and 2, 3 – lower branches.

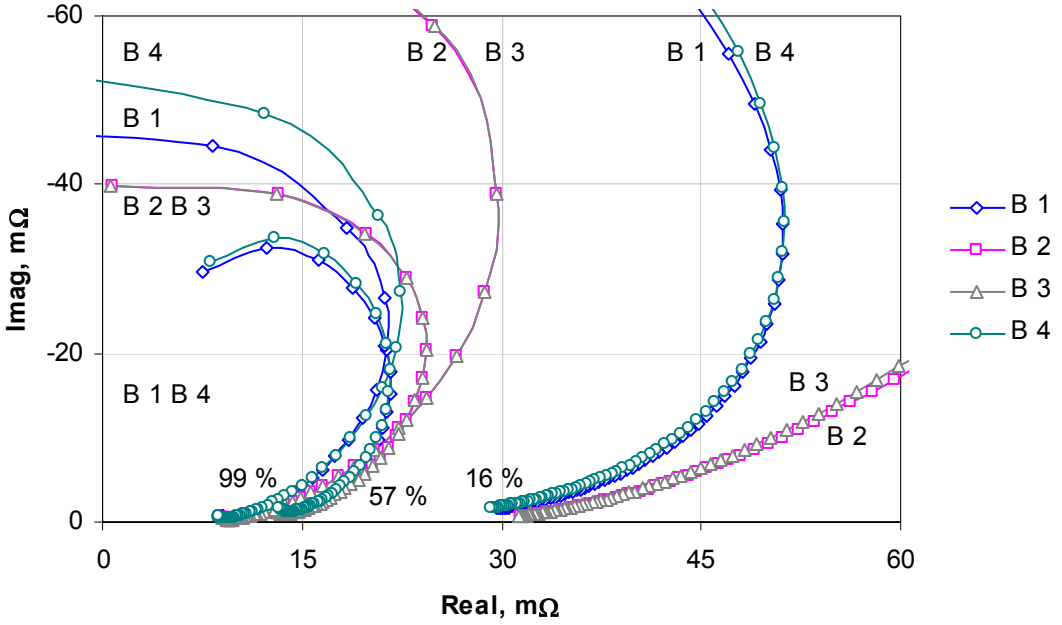

Fig. 4.15. Cell impedance shown for discharge of SOC = 99, 57, 16 %. These curves are more warped than for positive electrode. The curves for similar batteries 1, 4 and 2, 3 are closer to each other.

The Warburg impedance [34] represents data in the mHz range approximately as a line with certain slope. The slope depends on the lowest frequency used; in the mHz range it approaches the vertical or horizontal lines in dependence on type of model used. The "coth" type model (de Levie impedance [12]) is developed [34] for the non-permeable diffusion layer and the "tanh" type model for the permeable diffusion layer at boundary. The "coth" type model is more relevant to the positive electrode or cell and "tanh" type model to the negative electrode but by values they are far from actual in the mHz range.

The shape of impedance for the negative electrode is a semicircle, which agrees with the curves obtained in [2], [30] , [34], [41], [42], [43], [44], [54].

The negative electrode is less affected by acid concentration than positive electrode. Its time-varying change is flatter and characterised with slightly negative coefficient a_1 of the exponential power series. This makes for difference in the spin direction of the impedance curves. The spin of the logarithmic spiral is clockwise oriented for the positive electrode (Fig. 4.13) and cell (Fig. 4.15), and counter-clockwise oriented for the negative electrode (Fig. 4.14).

4.6. Overall Impedance

The overall impedance of electrochemical and double-layer processes can be calculated approximately by the superposition of both impedances. The constant ohmic resistances of the conducting elements and the charge-transfer resistance should be removed partially from the superposition to avoid double consideration

$$Z(\omega) = Z_{DL}(\omega) + Z_F(\omega) - R_0 - R_{ct}, \tag{4.19}$$

where
Z - overall impedance,
Z_{DL} - double-layer impedance,
Z_F - electrochemical impedance,
R_0 - resistance of conducting elements,
R_{ct} - charge-transfer resistance.

The approximation formula (4.19) is justified by the nature of slow and fast processes. They are not overlapping in frequency (see the caption of Fig. 4.16). The double-layer capacitance is an effective shunt for the faradic current at higher frequencies than 0.01-0.1 Hz. This is shown in Fig. 4.16. The electrochemical impedance, being several times larger, can characterize the discharge properties of the tested batteries more completely than double-layer impedance, allowing the small inequalities between batteries (B1, B4 vs. B2, B3) to be detected.

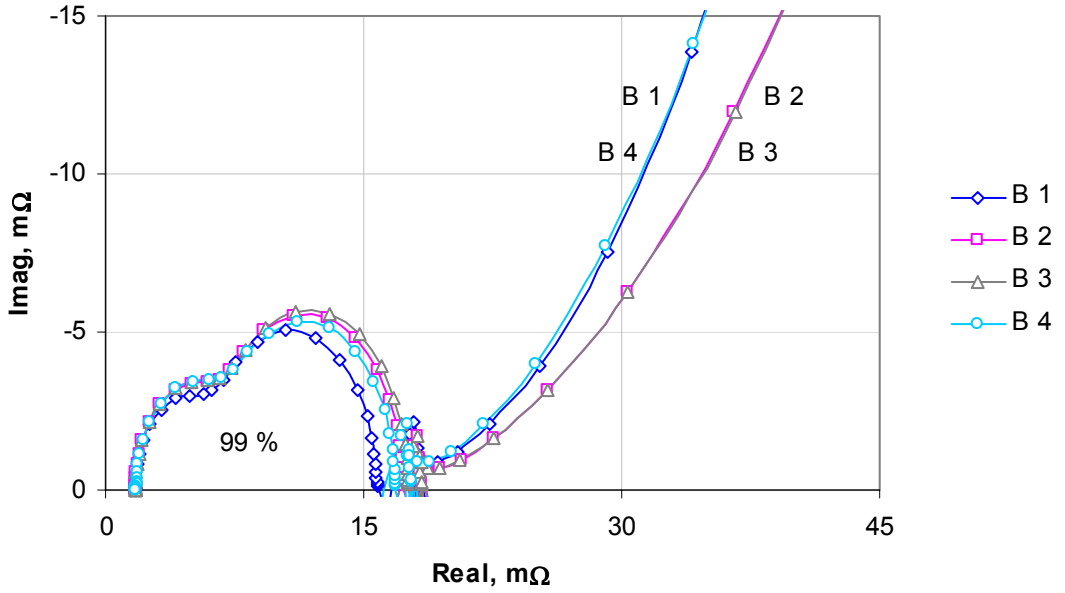

Fig. 4.16. Overall impedance shown for discharge of fully charged batteries. The first quarter arc (> 10 Hz) corresponds to the double-layer impedance at the negative electrode, the second quarter arc (≤ 10 Hz) the double-layer impedance at the positive electrode. The electrochemical impedance corresponds to the frequencies ≤ 0.1 mHz. The fuzzy area between the two processes shows the periodic components originating from the method used.

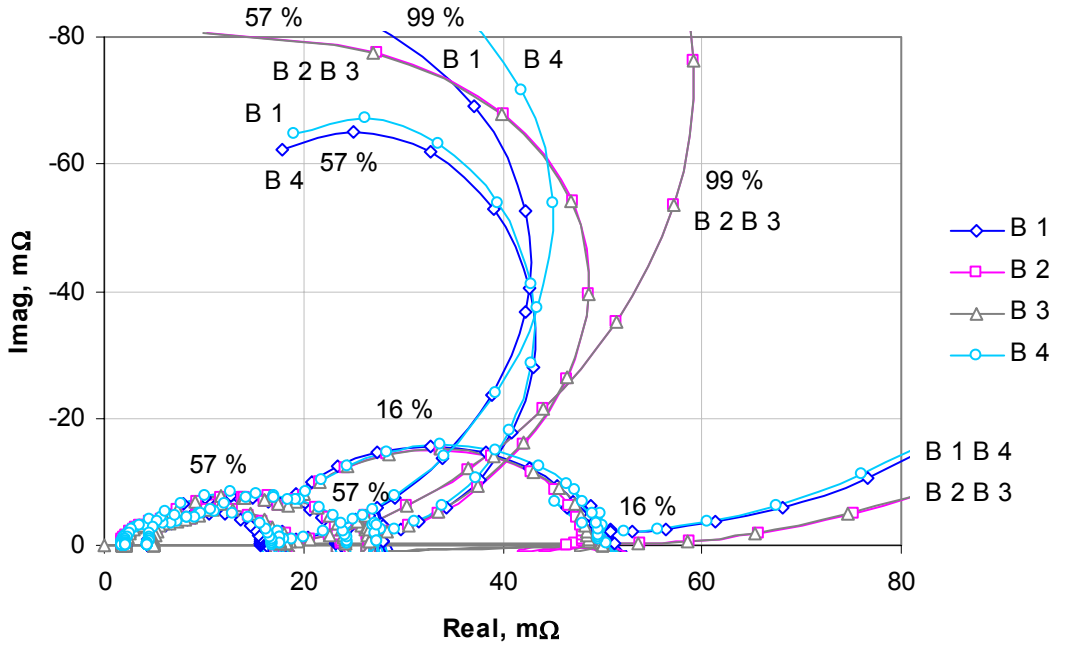

Fig. 4.17. Overall impedance shown for discharged batteries of SOC = 57, 16 % in wide range of frequencies from 1mHz to 1kHz (the periodic components are not shown).

4.6.1. Comparison with Linear Stationary Analyses

The modulus and phase angle of the overall impedance measured over eight decades of frequencies, i.e., from 1mHz to 100 kHz, on several types of batteries was reported in [26], [27] and low frequency impedance in [41], [42], [43]. These measured results

are somewhat similar to the predicted results in [P5], [P7], [P8], irrespective to the different type of batteries used.

The double-layer impedances for the positive and negative electrodes are closer to each other in [27] and less affected by the SOC [26] than in [P5], [P7], [P8].

The impedance spectrum resulting from the non-stationary analysis [P5], [P7], [P8] in μHz range is different from the corresponding spectrum of the linear stationary analysis [26], [27], [41], [42], [43] in mHz range due to the following reasons:

1. The Warburg part of the impedance curves in [26], [27], [41], [42], [43] is more depressed and shorter. This is because of the lower frequencies used. The lower limit of the frequency considered in linear analysis is about 1-5 mHz, equivalent to the forecast period T_0 = 3-17 min. In [P8] the test batteries were analysed using much longer period T_0 = 2 h. If the period had been decreased, the shape of impedance would have been more linear and shorter. For comparison, see the curves of impedance analysed on the same test batteries, but for T_0 = 1h in [P5]. The more linear and shorter curves are natural: the shorter test period includes less information on the non-stationary behaviour of a battery.
2. Higher dc current has tendency to give more depressed impedance curves [P5], [P7], [P8]. This is because of the electrode reaction is highly non-linear. Its equation (2.5) can be approximated with a linear function only if the potential is close to the equilibrium potential or in open-circuit conditions [26], [27].

4.7. Conclusion

Battery impedance is a combination of double-layer and electrochemical reaction impedances. The double-layer impedance depends on the state of electrode through the double-layer capacitance and charge-transfer resistance. The frequency response characteristics are different for positive and negative electrodes – double-layer process is slower on positive electrode. Its phase-angle has a peak at about 0.1 Hz for the positive electrode and at about 10 Hz for the negative electrode for tested batteries. From this, we can conclude that many conventional impedance meters see the negative electrode only.

The double-layer impedance depends on SOC so strongly that even large differences between batteries are masked. Hence, it is difficult to distinguish between outwardly equal batteries with different backup time by double-layer impedance.

The electrochemical impedance depends on electrode reaction through basic processes for SOC, porosity, acid concentration, and others. It characterizes these processes rather well at low frequencies in milli- and microhertz range. Batteries in this range can be analyzed using current-voltage and temperature measurements and the method proposed described in this chapter. The electrochemical impedance is a sensitive indicator: it can distinguish between outwardly equal batteries with different backup time.

Chapter V

5. Efficient Software for Battery Estimation and Analysis

5.1. Introduction

Previous chapters have introduced the battery models for main and gassing reactions, as well as impedance. The purpose of this chapter is to show how prototype software suitable for quick and effective evaluation of batteries is implemented. The software is based on fast calculation algorithm developed from the theoretical cell models presented in Chapters II-IV. The implementation of the algorithm is optimised by utilising sparse matrix technique, parallel identification of batteries, and, where possible, substitution of the distributed parameter model with reduced dimension or lumped parameter model.

In addition to the calculation algorithm and its optimised implementation, the chapter covers calibration methods and calculation speed/precision. Also, screenshots from the software (with explanations) are presented.

The material on this chapter is, for the most part, based on [P3], [P4], [P2].

It should be noted that since all battery research groups in the world are using various computational tools, similar sparse matrix-based methods for solving electrochemical systems do exist and are implemented in experimental software, including battery software [17] [23], [24]. However, due to public unavailability, these were not used as a basis for our reasonably quick and accurate approach.

5.2. Contribution

The following was carried out:

1. Fast calculation algorithm was developed from theoretical cell model, utilising specific structure of the model along with advanced calculation techniques. As a result, the required calculation time was reduced drastically in prototype battery testing software. The calculation speed of one physical second per one hour of battery time (so, for example, modelling of 12-hour process takes just 12 seconds) was achieved for lumped parameter model and one minute per one hour for distributed parameter model. Single battery or several batteries in a string can be analysed with nearly equal speed. This improvement makes application of the theoretical cell model in battery testing practical.

2. Based on the algorithm, modelling software was developed. A good fit was found between data measured in experiment and data predicted by the software for full range of charge-discharge processes including overcharge. High prediction obtained is a strong evidence for applicability of the model and its implementation in software for battery characterization. The software can evaluate unobservable processes like overpotential, reaction rate, porosity, acid concentration and other electrode parameters from measured float voltage, applied current and temperature of surrounding atmosphere. Also, outwardly equal batteries with different backup time and cut-off time can be distinguished in practice.

5.3. Calculation Method

The battery model can be in general represented as the following large-scale system

$$dz = [A_3 z - b(z)]dt, \quad z_t = z_0, \tag{5.1}$$

where

z - electrochemical state of battery; it contains the following co-ordinates:

$z = [i_l, \phi^l, \phi^s, \varepsilon, c, \theta]^T$ - current density, liquid potential, solid potential, porosity, acid concentration and SOC. Every coordinate is a space-dependent process, represented in a number layers. The sandwich of two electrodes and separator is divided into L layers, each part of sandwich has equal number of layers.

A_3 - three-diagonal matrix,

b - nonlinear vector function. It is a combination of power function, hyperbolic function and exponential function, depending on co-ordinate.

The model is dynamic for porosity, acid concentration and SOC; it is static for other components, i.e., current and potential ($dx = 0$, $x = [i_l, \phi^l]^T$).

The system (5.1) can be solved using time-iterative calculation procedure ($t = 0, \Delta t, 2\Delta t, ...$).

$$z_{t+1} = z_t + [A_3 z_t - b(z_t)]\Delta t, \quad z_t = z_0. \tag{5.2}$$

This is a two-rate system with current and potential considered as dynamic processes using a small parameter technique to introduce a slow component of the system.

Calculation engine. The system (5.2) can be solved using several methods. The algorithm (Fig. 5.1) used is outlined below. This is a simple and fast calculation method.

First, the initial state is defined using some reference values for processes: $z = z_0$. This is followed by calculation of various process values as described below.

Step 1. Calculate volumetric current density $v = A(\theta)\, j(c,\eta)$ for fixed parameters of SOC, acid concentration and overpotential, i.e. calculate profile (vector) of the active surface area $A(t,x) = A(\theta(t,x))$, $x = 0, \Delta x, \ldots, L\Delta x$ from Eq. (2.2) or (2.3) and profile of the transfer current density $j(t,x) = j(c(t,x),\eta\,(t,x))$ from Eq. (2.5) for fixed parameters $z_0 = [\theta_0, c_0, \eta_0]^T$ - SOC profile, acid concentration profile and overpotential profile correspondingly. Note that the volumetric current densities in the separator and centres of electrodes are zeros.

Step 2. Solve Eq. (2.1) as system $A_2 i_l = b(z_0)$ for the current density in liquid phase. Here i_l - current density profile (vector) in liquid phase, A_2 - double-diagonal matrix of units: -1 on diagonal and +1 on upper diagonal, $b(z_0)$ - vector function with coordinates: $b_n = v(\theta(t,n\Delta x),c(t,n\Delta x),\eta(t,n\Delta x))\Delta x$, v - volumetric current density, Δx - step of depth (space discretization), $z_0 = [\theta_0, c_0, \eta_0]^T$ - fixed parameters: SOC profile, acid concentration profile and overpotential profile correspondingly.

The current density in separator is equal to applied current. This is a boundary condition. It can be used for solution as follows. Change overpotentials $\eta_0(0)$, $\eta_0(L)$) in the centres of electrodes until the model-calculated applied current is equal to a measured value (using PID-adjustment). The resulting values are the boundary conditions for calculation of the liquid potential.

Step 3. Solve (2.6) as system $A_2\phi^s = b(z_0)$ for the solid potential. Here ϕ^s - potential profile in solid matrix, A_2 - double-diagonal matrix of units, $b(z_0)$ - vector function with coordinates: $b_n = [i_l(t,n\Delta x) - i_{app}(t)]\Delta x/\sigma\varepsilon(t,n\Delta x)^{\beta 3}$, i_l - current density in liquid phase, i_{app} - applied current and ε - porosity, $z_0 = [i_{l.0}, \varepsilon_0]^T$ - fixed parameters: current density profile in liquid phase and porosity profile correspondingly.

The starting points for calculation are zero boundary values at separator surface. A back-forward solution of Eq. (2.6) can be used for the positive electrode and forward solution for the negative electrode. There will be free boundary values in the centres of positive electrode and negative electrode.

The potential drop on solid matrix is small. To simplify, it can be ignored as well.

Step 4. Solve (2.7) as system $A_2\phi^l = b(z_0)$ for the liquid potential. Here ϕ^l - potential profile in liquide phase, A_2 - double-diagonal matrix of units, $b(z_0)$ - vector function with coordinates: $b_n = i_l(t,n\Delta x)\Delta x/\kappa\varepsilon(t,n\Delta x)^{\beta 4} + (RT/F)(1 - 2t^o_+)\, f\, [c(t,(n+1)\Delta x) - c(t,n\Delta x)]$, κ - acid conductivity, f - molar activity, t^o_+ - transference number, $z_0 = [i_{l.0}, \varepsilon_0, c_0]$ - fixed parameters: current density profile in liquid phase, porosity profile and acid concentration profile correspondingly.

Step 5. Solve (2.9). Calculate a new value for porosity by integration in time: $\varepsilon_{t+\Delta t} = \varepsilon_t + b(z_0)\Delta t$. Here ε - porosity profile, Δt - step of time, $b(z_0)$ - vector function with coordinates: $b_n = K_1\, v(\theta(t,n\Delta x),c(t,n\Delta x),\eta(t,n\Delta x))$, v - volumetric current density, $z_0 = [\theta_0, c_0, \eta_0]^T$ - fixed parameters: SOC profile, acid concentration profile and overpotential profile correspondingly.

Step 6. Solve (2.10). Calculate a new value for acid concentration by integration in time: $c_{t+\Delta t} = c_t + [(D/\Delta x^2)A_3 c_t + b(z_0)]\Delta t$. Here c - acid concentration profile, A_3 - three-diagonal matrix: -2 on diagonal and +1 on upper diagonal and lower diagonal, D - diffusion coefficient, $b(z_0)$ - vector function with coordinates: $b_n = [K_2 - c(t,n\Delta x)\, K_1]\, v(\theta(t,n\Delta x),c(t,n\Delta x),\eta(t,n\Delta x))/\varepsilon(t,n\Delta x)$, v - volumetric current density, $z_0 = [\theta_0, c_0, \varepsilon_0, \eta_0]^T$ - fixed parameters: SOC profile, acid concentration profile, porosity and overpotential profile correspondingly.

Step 7. Solve (2.4). Calculate a new value for SOC by integration in time: $\theta_{t+\Delta t} = \theta_t + b(z_0)\Delta t$. Here θ - SOC profile, $b(z_0)$ - vector function with coordinates: $b_n =$

$v(\theta(t,n\Delta x),c(t,n\Delta x),\eta(t,n\Delta x))\alpha_{Ah}/Q_{max}$, v - volumetric current density, α_{Ah} - charging efficiency, Q_{max} - theoretical capacity, $z_0 = [\theta_0, c_0, \eta_0]^T$ - fixed parameters: SOC profile, acid concentration profile and overpotential profile correspondingly.

Finally, replace z_0 with newly calculated values and return back to step 1.

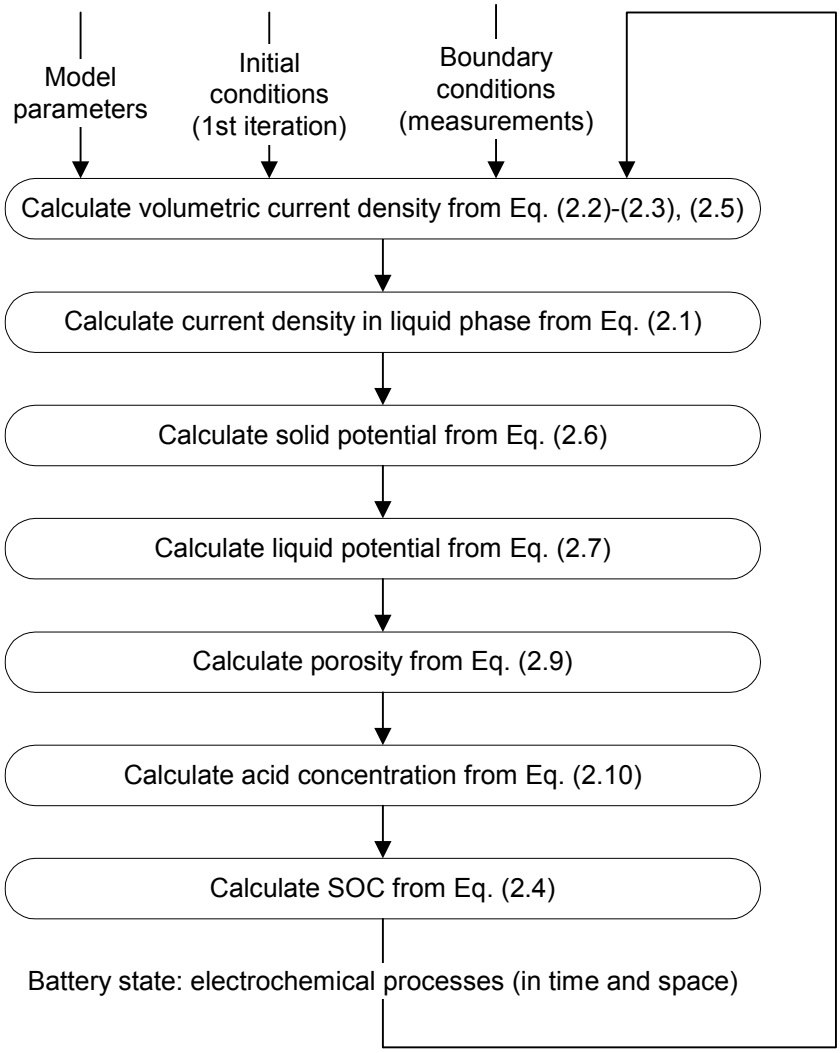

Fig. 5.1. The calculation algorithm.

Optimisations. Thickness of porous electrode is about 1 mm or less. A small sampling interval (250 ms) should be used for stable approximation of the electrode with multiple layers (6). Considering computational power that is available from today's PCs, it is a measurable challenge to approximate electrode even with 6 layers.

The need for model calibration makes this significantly harder still. The best prediction accuracy of the battery string is obtained if every battery in the string is calibrated separately. This includes running each battery repeatedly against experimental data with different model parameters, trying to match simulated current and voltage readings to the ones actually measured. For reasonable accuracy, 50-300 runs are required for each battery. With experimental data being from about half a day in length, it is clear that the calculation speed needs to be much faster than the physical speed for the system to be of any use.

The initial system achieved calculation speeds about two times slower than physical process time, making automatic model calibration impossible. Since then, four optimisations were introduced as follows.

1. The need for computational power was reduced by about 100 times using sparse matrix technique [40]. The diagonal property of the matrix A is used in this technique. Using the fact that the matrix A has three diagonals for acid concentration and two diagonals for all other processes, calculation procedure can be made faster. In general, it is complicated to apply 2- and 3-diagonals properties simultaneously. However, it is simple to apply these properties if we solve system (5.2) for every process separately, assuming that other processes are known from the last step of iteration. This separation will not produce essential inaccuracy in the case of smooth variation of process, but it does create short-term oscillation in the calculation scheme after transaction from discharge to recharge or vice versa. It should be noted that this separation method is not the most accurate, but it is the simplest and fastest one.
2. Before, sequential calibration of battery string was used, i.e., the program only identified one battery at a time, running the other batteries at their default settings. By converting this method to parallel calibration, up to tenfold speed increase was achieved, depending on the length of the battery string. Best of all, the parallel conversion introduced no significant overhead.
3. Taking advantage of the fact that large discharge rates (C/I < 1 hour) are often not used in telecommunications UPS systems, distributed parameter model used before, where each electrode was divided into 6-16 layers, could be replaced by reduced order or even lumped parameter model, where each electrode is viewed as a whole. This alone speeded up the program significantly, up to five times, but the main benefit was that it allowed the time step of iteration to be increased drastically (10-100 times) – see next optimisation.
4. Reducing the number of layers to one allowed time step to be increased most significantly. With improvement of stability, speed increase up to 900 times was achieved. For this extension, the distributed parameter model was converted to lumped parameter model for both electrodes. Large modification was made to the calculation engine for application on two models simultaneously (usually, different methods are used in the literature to solve these models). Achieving stability in singular lumped parameter case is a rather complicated task. The stability is sensitive on boundary conditions of the sandwich of cell. They must be defined even more precisely than in the case of distributed parameter model.

With these optimisations, the calculation speed of one physical second per one hour of battery time was achieved for lumped parameter model and one minute per one hour for distributed parameter model (see Section 5.6). This improvement makes application of theoretical cell model in battery testing possible.

5.4. Model Calibration

Before the evaluation of a given battery string can be carried out, the model parameters need to be matched to the physical properties of the string. Although many parameters are known from literature and some parameters are known beforehand, such

as the number of batteries in a string, number of sections per battery, and dimensions of electrodes, many are unknown and cannot be directly measured.

For these parameters, an automatic calibration procedure is applied that uses the measured current, voltage, and temperature data from a full discharge or a partial discharge and the subsequent recharge for the battery/string being calibrated. Use of full discharge information naturally gives more accurate model than the use of the partial discharge. The method uses the battery current as an excitation and predicts the battery voltage as a response as shown in Fig. 5.2. The difference between the predicted and measured voltage is minimised by adjusting the model parameters accordingly, using the simplex method described in [28].

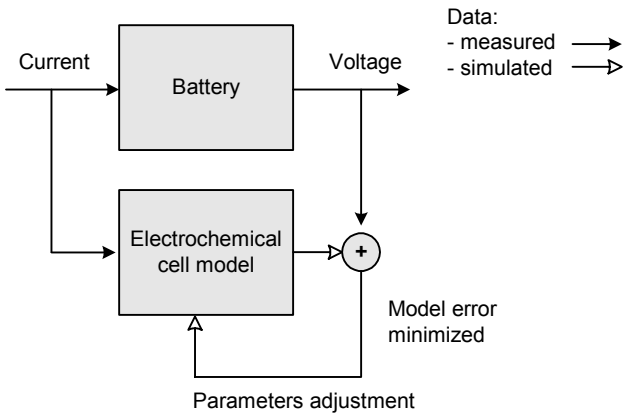

Fig. 5.2. Battery model calibration procedure.

If the required measurement data is available, the model for each block in a battery string can be calibrated individually. A typical inaccuracy is in the range of 0-50 mV for a 12 V battery block (i.e., six cells in series).

The following parameters are usually configured:

- Thickness of porous plates for both electrodes and separator.
- Exchange current density for both electrodes.
- Tortuosity exponents for SOC-related reaction rate limitation.
- Maximum active surface area and electrode morphology coefficients.

It was observed on tested batteries that these parameters affect model performance the most. However, if the need arises, different parameters can be chosen. Overall, the software currently has over 50 parameters common for all batteries in a string, plus 25 battery-specific parameters.

The software uses simplex method for calibration. This is a standard method, which is most powerful if initial values of parameters are known relatively well. The method is suitable for local optimisation; it is faster than random search (Monte Carlo) method (random search method is described in [53]), especially when optimising more than one parameter at the time. The simplex is controlled by a choice of initial area. Setting up large initial area results in wide search, whereas setting up small area results in local search. Although the method can jump over true value of parameters if the initial area is too large with the starting point close to optimum and the method is slow if

initial area is too small with the starting point far from optimum, it is fairly well suited for model calibration in this case.

The calibration process is reasonably quick (for exact figures, see Section 5.6.). Fast lumped parameter model can be used in the case of low discharging rates (C/I > 2 hours) and slow distributed parameter model in the case of high discharging rates (C/I < 1 hours).

5.5. Software Features

The software implementing the theoretical cell model is written in C++ and runs under Win32 platform (Windows 98/2000, etc). After the model has been calibrated for a given battery string, the program is able to visualise, using real-time charts, a large number of unobservable processes of the electrode by total current, terminal voltage and temperature of the surrounding atmosphere of the battery. Besides main parameters like the active material mass and morphology of electrodes, other unobservable processes can also be evaluated. These include overpotential, reaction rate, porosity, acid concentration and other electrode parameters. They can be used for more thorough battery analysis, being useful in battery diagnostics or failure detection.

Up to 10 batteries in a string can be tested simultaneously with the current version of the software; this number can be increased quite easily in future versions (the required calculation time depends on the length of battery string relatively weakly).

The features of the software are explained in more detail below.

5.5.1. Options

Selecting **File | Options** will bring up Options dialog as shown in Fig. 5.3.

From this dialog, various options can be configured. It also allows the user to modify model parameters directly (instead of calibration) is so desired. The page names should be quite self-explanatory.

In addition to parameters common to all batteries, it is possible to set battery-specific parameters from the Electrode page as shown in Fig. 5.4.

Despite the large number of available model parameters, only few of them need to be modified often; the rest have reasonable defaults.

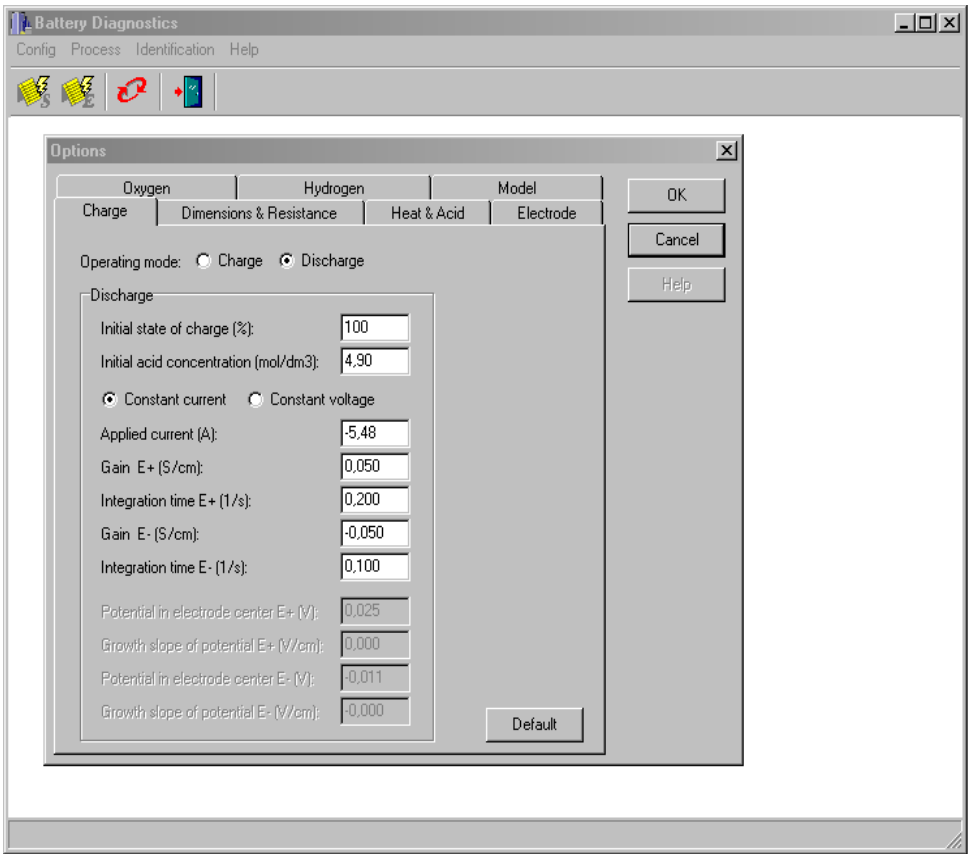

Fig. 5.3. Options dialog.

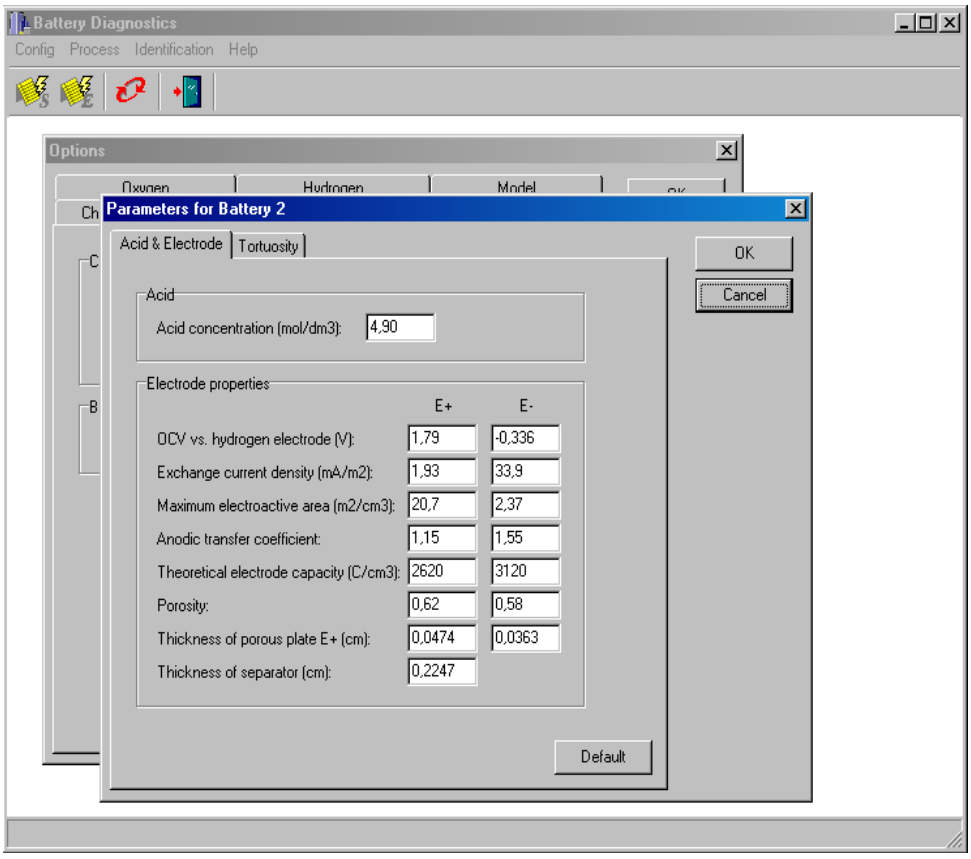

Fig. 5.4. Setting battery-specific parameters.

5.5.2. Identification (Calibration)

Choosing **Identification | Identification** will allow user to choose the parameters to be calibrated using the method described in Section 5.4. The software will do the number of cycles specified by the user, using initial area also set by the user. After the calibration process has finished, choosing **Identification | Results Sorting** will let the user review the new values for the model parameters, and, if satisfied, make them active.

5.5.3. Battery Evaluation

After the model has been calibrated, the software is able to visualise various unobservable battery processes using real-time charts. There are two options:

1. Choosing **Process | Simulation** will launch simulation of battery process, using parameters set via calibration and Options dialog, and simulated values for SOC, float voltage, charge/discharge current, battery resistance, and temperature. No data files are used.
2. Choosing **Process | Simulation + Recorded Data** will launch a process similar to option 1, only this time using previously measured values for the parameters listed above, read from a text-format data file.

Below are results from an (option 2) run with four batteries described in Section 5.7.

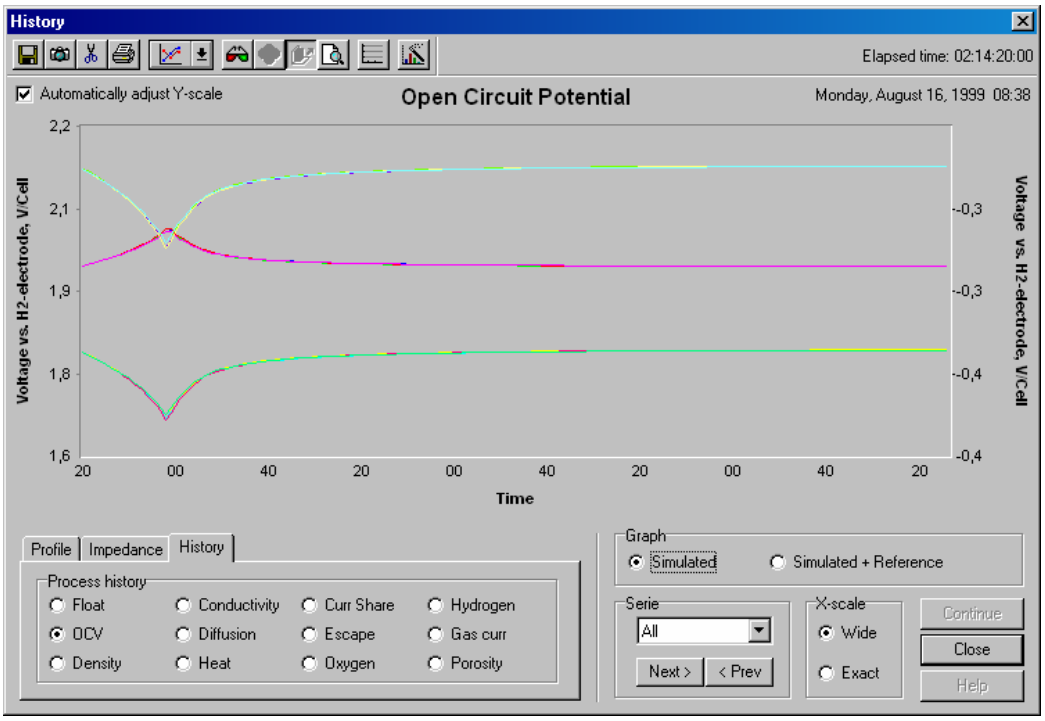

Fig. 5.5. Open circuit potential as charted by the battery testing software. Neg. electrode potential is the line in the middle, pos. at the bottom, total at the top.

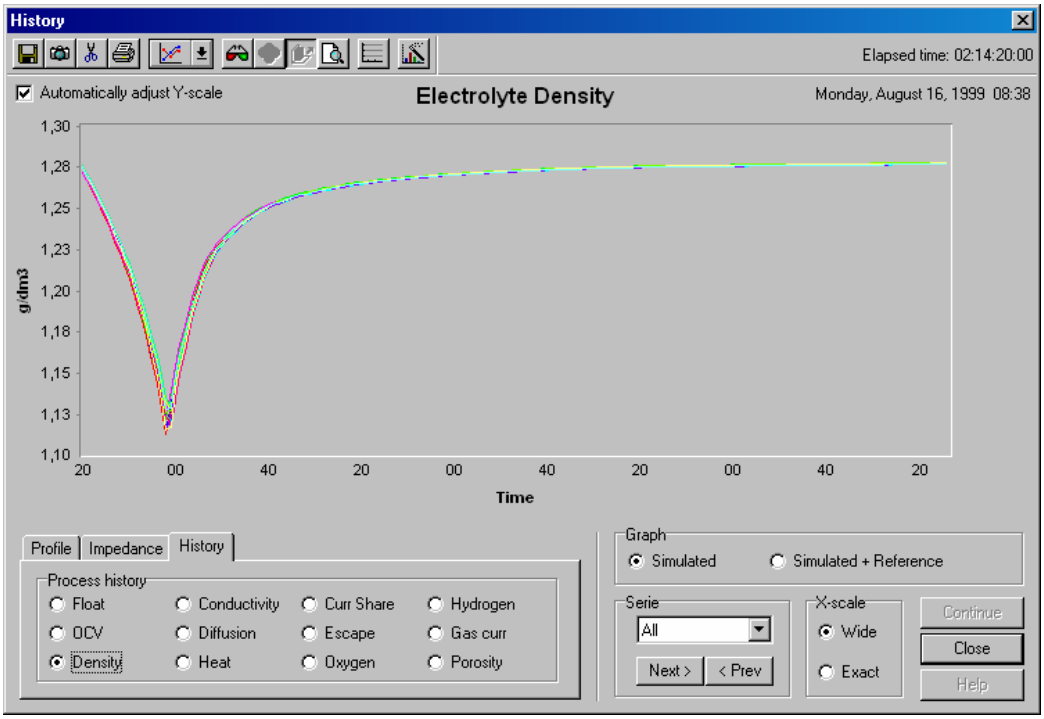

Fig. 5.6. Evolution of electrolyte density. Because of slow charge-discharge rates, the diffusion of species is fast, enough to equalise the concentrations in positive electrode, negative electrode, and separator.

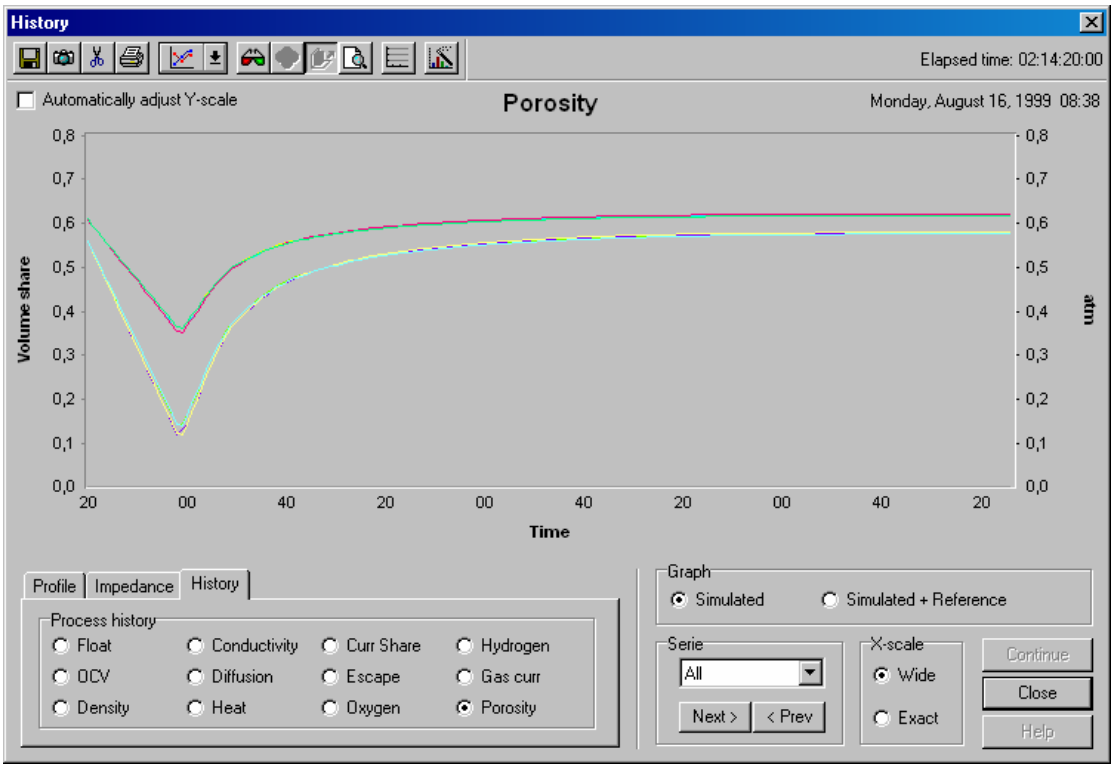

Fig. 5.7. Acid porosity. Porosity is lower in negative electrode in comparison with positive electrode.

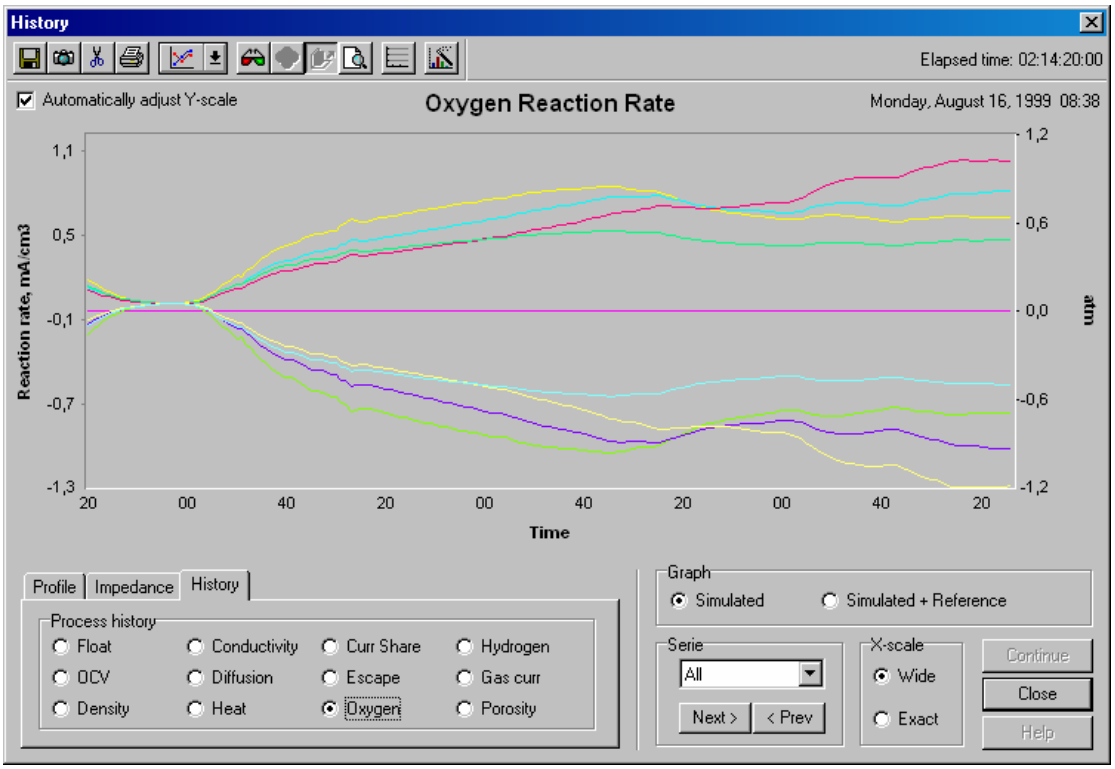

Fig. 5.8. Oxygen reaction rate. There are quite significant differences between gassing processes in batteries, especially at the end of charge.

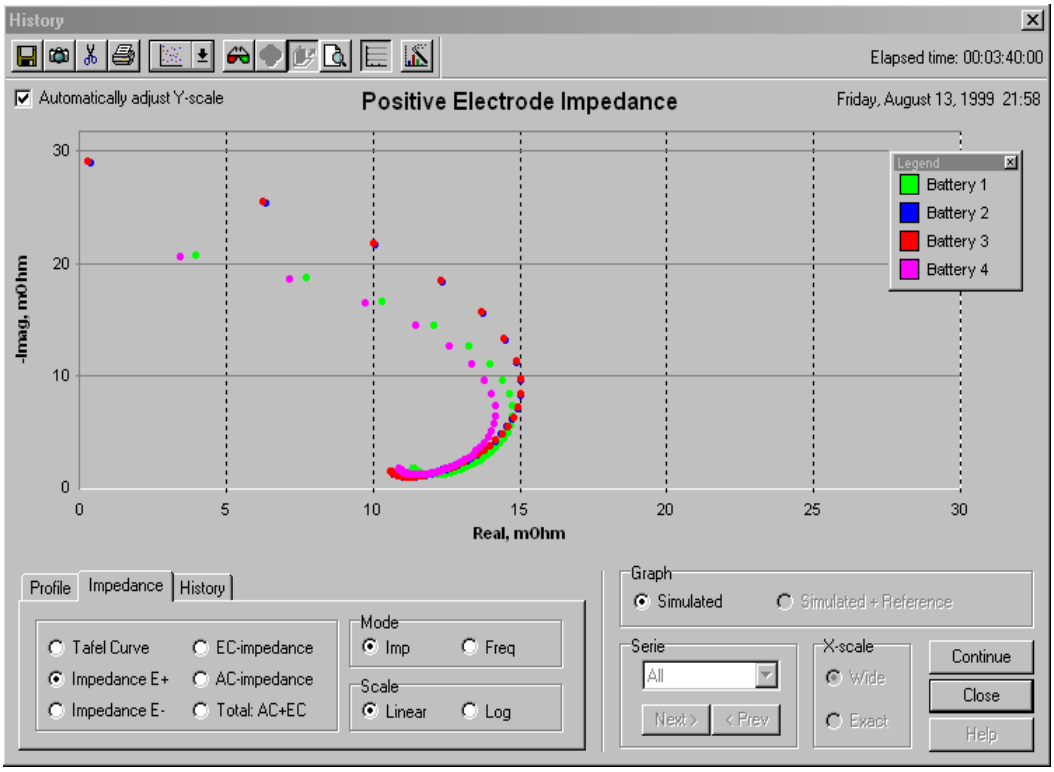

Fig. 5.9. Electrochemical impedance of positive electrode shown for frequency 1 mHz - 1 kHz at 60 % SOC.

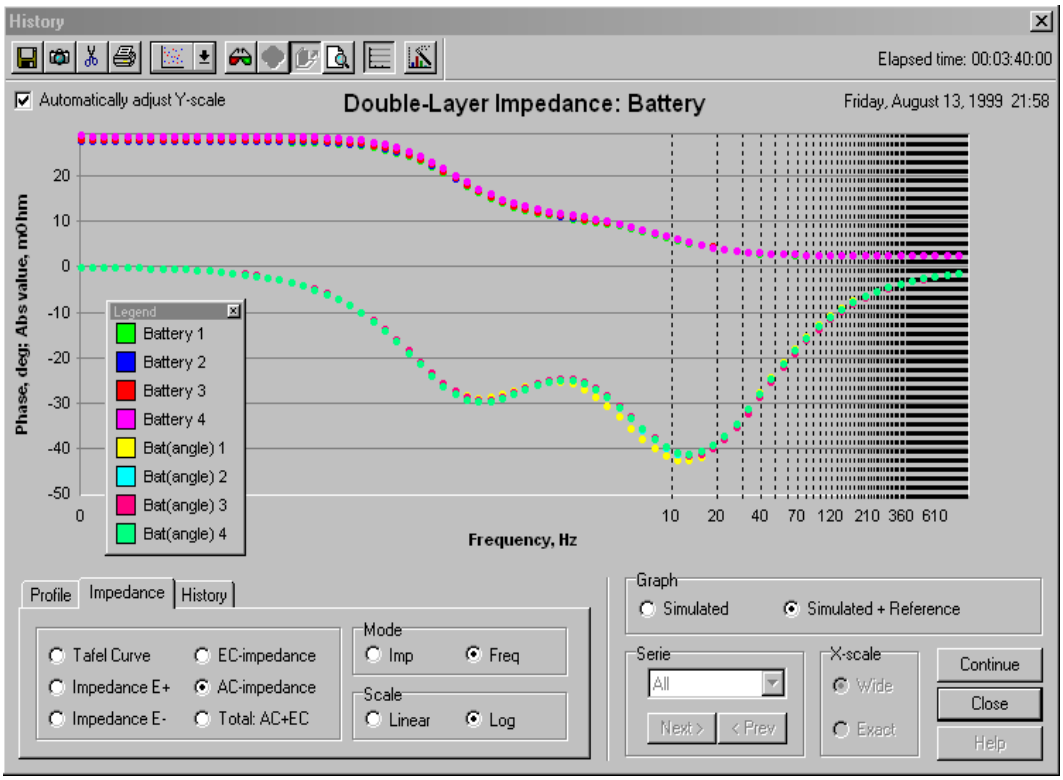

Fig. 5.10. Double-layer frequency response: modulus and phase angle at 60 % SOC.

The software is also able to draw electrodes and separator profiles at any point of the process. Sample profiles taken at 40% SOC level with distributed parameter model and discharge current of 20 A (C/I = 1.8 h) follow.

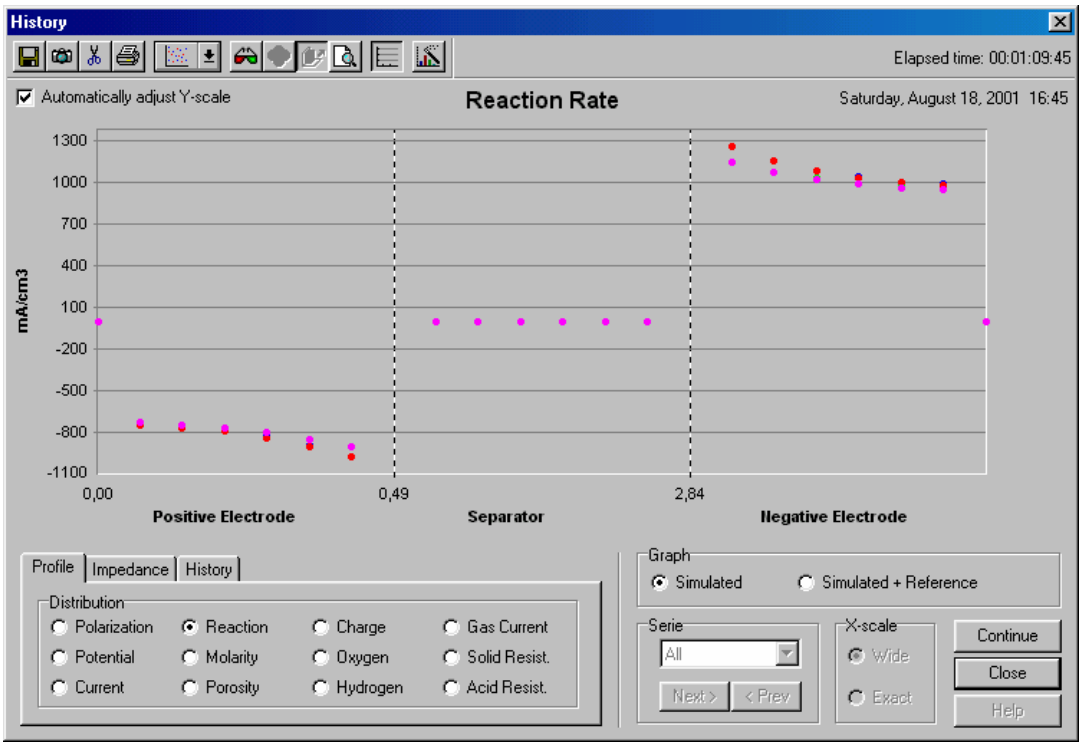

Fig. 5.11. Reaction rate depends weakly on location in electrode and strongly on discharge time.

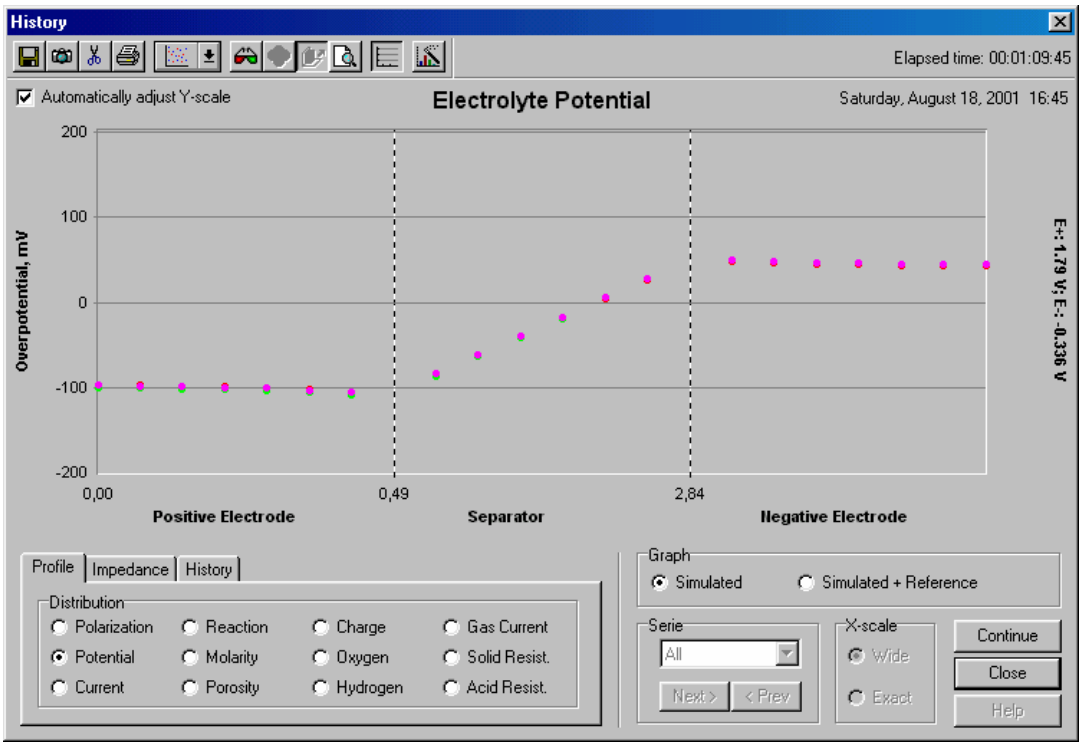

Fig. 5.12. Overpotential. Electrolyte overpotential depends weakly on location and strongly on discharge time.

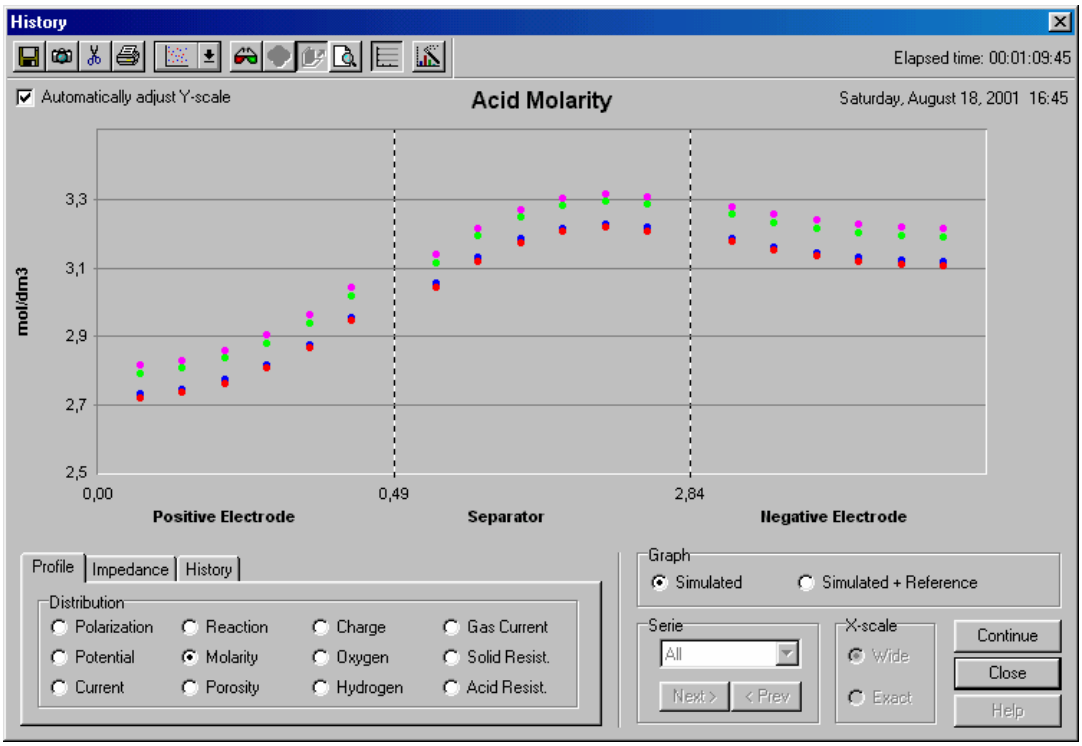

Fig. 5.13. Acid concentration in electrodes. The difference in acid concentration between batteries is visible in this figure.

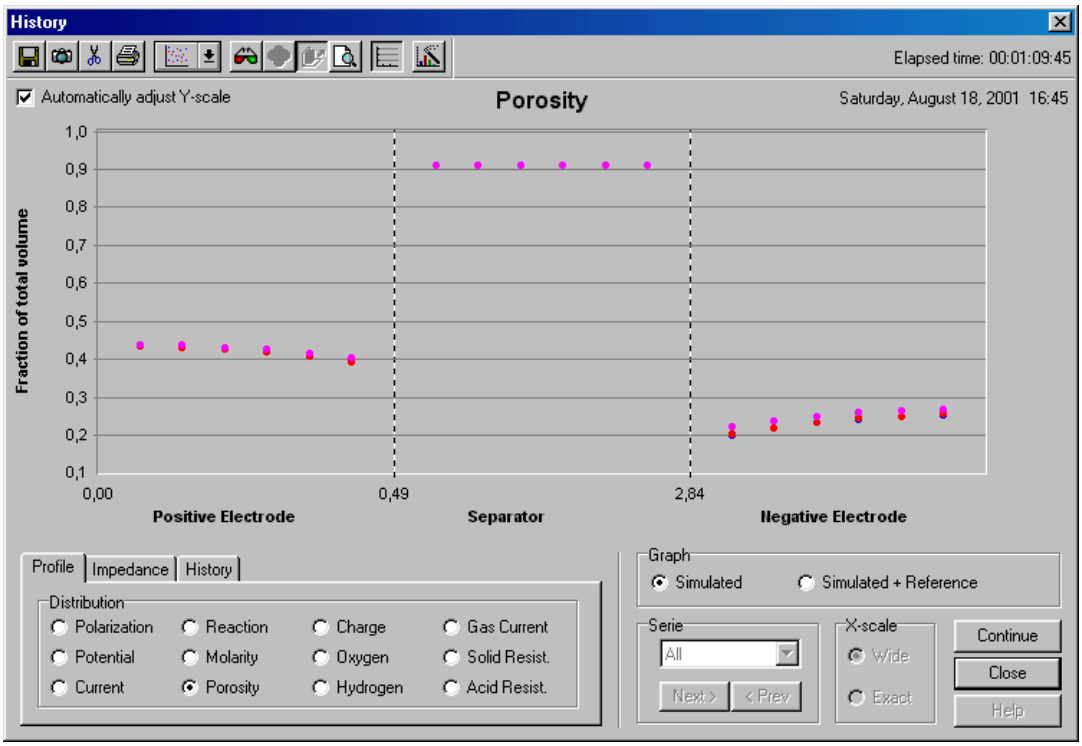

Fig. 5.14. Electrode porosity depends weakly on location in electrode and strongly on discharge time. It is lower in negative electrode in comparison with positive electrode.

5.6. Performance

The model can be calibrated using data of discharge process. There is no need for distributed parameter model if C/I > 2 h.

The performance of the calibration process was tested on a PC with 1 GHz Pentium III processor and 256 MB of RAM running Windows 2000. The measurements file was run through 300 times, ensuring good calibration of the model. Both lumped and distributed model were tested with one and four batteries, taking advantage of the fact that there is no need for distributed parameter model if discharge time (C/I) > 2 h. In distributed model, two, four, and six layers were tested. For distributed parameter model, the discharge time was 1 h; for lumped model, it was 6 h. The results are shown in Table 5.1.

Table 5.1. Required calculation time to ensure good calibration of the model using data of 1-6 h discharge process.

Model	C/I	Layers	1 battery	4 batteries
Lumped	6 h	1	6 min 17 s	9 min 12 s
Distributed	1 h	2	8 min 27 s	12 min 45 s
Distributed	1 h	4	22 min 40 s	33 min 20 s
Distributed	1 h	6	1 h 28 min	2 h 16 min

5.7. Software Validation of the Model

The prediction accuracy of the software was tested against measured data recorded in many experiments (see Fig. 5.15 and Fig. 5.16). The following experiment, similar to the ones described in earlier chapters, was typical.

Four batteries, connected in a string and placed into a container, were charged and discharged at elevated temperature of 40-50^{o} C. The batteries were discharged to under 5-10 % and then charged up to 99-100 % of their real capacity during extended charging of 52 hours. The applied current and float voltage of batteries, as well as temperature in the container, were measured and recorded continuously.

Data presented in this chapter is relevant to the following experiment. A string of fully charged batteries was discharged after 1 day of rest with constant current at rate C/I = 5.6 h and then charged at rate C/I = 4.6 h for a short period until the voltage 2.13 VPC was reached. The charging current was then manipulated to carry out increasing voltage from 2.13 to 2.21 VPC. This made sure that all batteries were charged completely (similarly to taper charging procedure).

The batteries used in software validation had the following specification:

- Type: VRLA battery, gelled (GEL) or absorbed (AGM) technology.
- Nominal voltage: 12 V, nominal capacity: C = 28 Ah.
- Cut-off time: 5, 10 or 20 hours at discharge current of 5.1, 2.8 or 1.6 A for cut-off voltage 1.70-1.75 VPC.
- Number of sections: 6; number of positive plates: 4, negative plates: 3.
- Plate height: 11.3 cm, width: 15.4 cm.
- Thickness of positive plate: 0.23 cm, negative plate: 0.22 cm. Thickness of separator: 0.36 cm.

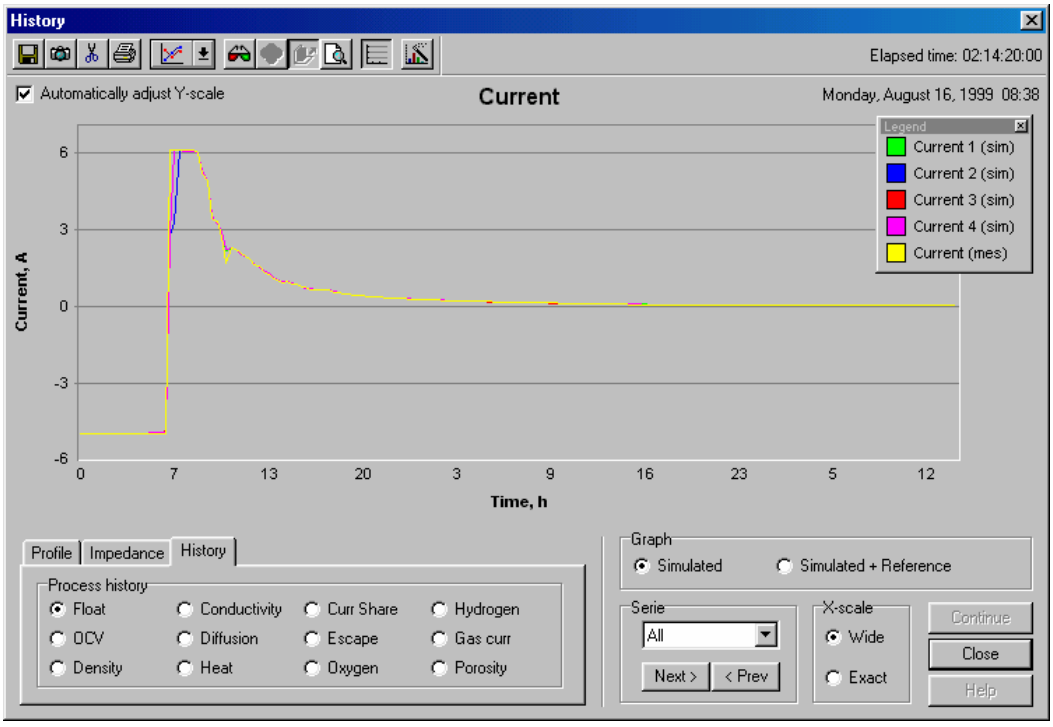

Fig. 5.15. Comparison of measured and simulated current. The software-reproduced current matches measured current rather well.

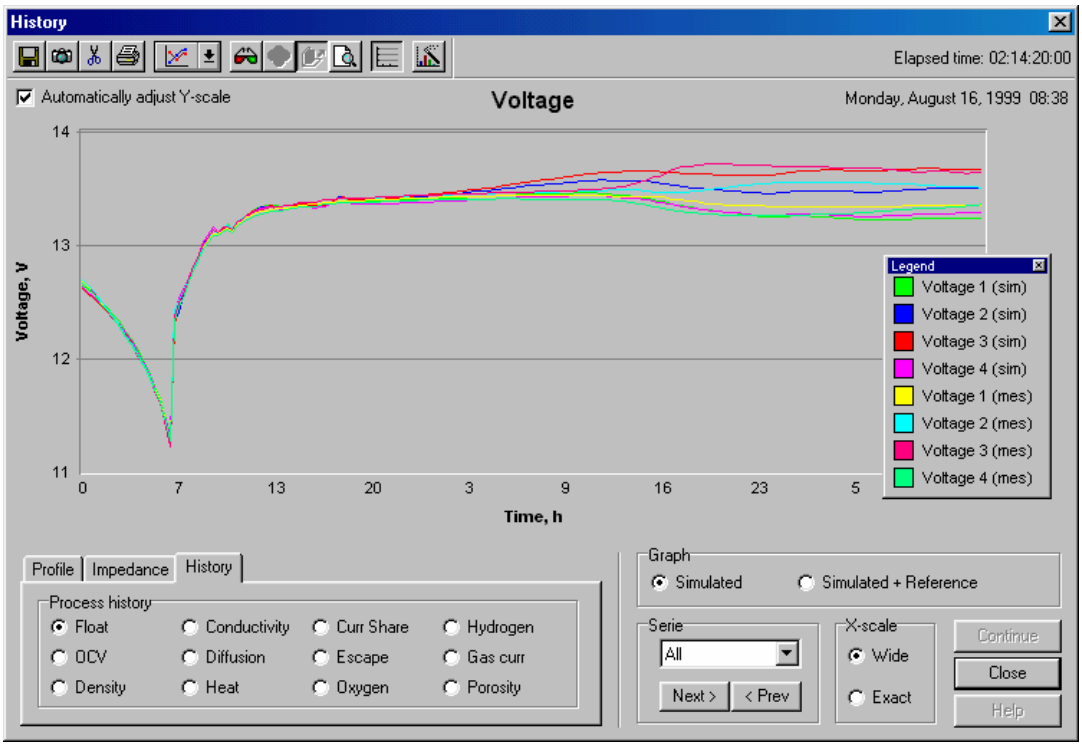

Fig. 5.16. Comparison of measured and simulated voltage. The software can predict measured voltage in full SOC range including deep discharge and overcharge.

The model current matches the measured current on test batteries in many details including the perfect charging curve and deviation of the measured current from the perfect curve.

Typical charging curve is shown in Fig. 5.16. This curve was first measured on test batteries and then predicted by software. The prediction accuracy is rather high. The lumped parameter model can predict measured voltage in full range of charge-discharge processes including deep discharge and overcharge. The following situation is demonstrated in Fig. 5.16. Higher voltage is measured on batteries 2, 3 and lower voltage on batteries 1, 4 during overcharge (the string voltage is nearly constant). Respectively, higher voltage is predicted by model on batteries 2, 3 and lower voltage on batteries 1, 4.

5.8. Conclusion

In tests, the software developed based on theoretical cell model predicted measured voltage and current of batteries rather well.

High prediction accuracy of the software is a strong evidence of its suitability for evaluation of the unobservable processes in battery by observable processes. Besides main parameters like the active material mass and morphology of electrodes, other unobservable processes can also be evaluated. These include overpotential, reaction rate, porosity, acid concentration, and other electrode parameters. Both lumped and distributed parameter models can be used.

The calculation algorithm is optimised for speed, so the required calculation time is not an obstacle for application in battery evaluation.

Chapter VI

6. Conclusions

In the following, the main results of the publications and author's contribution to them are summarised, along with some concluding remarks and plans for future work.

6.1. Concluding Remarks

The most significant result of this work is the modified theoretical electrochemical cell model and the software implementing this model. In tests, the software, when calibrated, predicted measured voltage and current of batteries rather well. This accuracy is evidence of its suitability for evaluation of the unobservable processes in battery by observable processes. Besides main parameters like the active material mass and morphology of electrodes, other unobservable processes can also be evaluated. These include overpotential, reaction rate, porosity, acid concentration, and other electrode parameters. Among others, backup time and cut-off time – important parameters for telecommunications UPS system – can be tested quite simply. Both (fast) lumped and (more precise) distributed parameter models can be used, depending on situation. The software, with its optimised calculation algorithms, is fast enough in both cases.

Also, since the model takes into account the gassing processes, it is possible to evaluate batteries during overcharge – by monitoring gassing currents – giving us the opportunity to reliably monitor the SOH without completely discharging the battery, something that cannot be easily done in UPS systems. This is especially useful considering that simple indicators like float voltage during overcharge or impedance/conductance (see below) often cannot be used as simple indicators of battery health.

Battery impedance was also studied by simulation. The results show that it is difficult to distinguish between outwardly equal batteries with different backup time by double-layer impedance. The electrochemical impedance, however, *is* a sensitive indicator: it can distinguish between outwardly equal batteries with different backup time. Unfortunately, the required frequencies are in the milli- and microhertz range, making the practical measurements (that are based on pulse analysis) very difficult.

6.2. Contents of the Publications

[P1] describes the basic process (main reaction) model and its application for battery state estimation and failure detection (gassing processes are ignored). A new morphology of electrodes is introduced and a charging factor applied. After being cali-

brated against experimental data, the model is applied for detection of the original source of differences between seemingly equal batteries.

[P2] and **[P3]** describe the (optimised) calculation algorithms and the modelling software built on the model. This software was used for obtaining all the results presented in this dissertation. [P2] is more model-centric, whereas [P3] describes the software in more detail.

[P4] provides an overview of the optimised algorithms and software and describes a possible centralized battery monitoring system utilising the battery analysis software as its core. A lumped parameter model is introduced.

[P6] extends the model presented in [P1] with support for gassing processes and hence supports more accurate deep discharge and overcharge modelling. The modified cell model is applied for evaluation of the unobservable gas formation processes by observable current-voltage and temperature measurements. Battery monitoring by resistance and gas formation processes during overcharge is analysed.

[P5], **[P7]** and **[P8]** explore, from different angles, the usability of impedance modelling for battery evaluation. [P5] and [P7] are written from a simpler, practical viewpoint, [P8] is more theoretical. A way to calculate impedance values from the main model is presented. It is applied for analysis of test batteries and shown to be accurate, enabling detection of differences in battery capacity. Both fast double-layer and slow faradic processes are covered.

6.3. Author's Contribution to the Publications

In **[P1]**, **[P2]** and **[P6]**, the author carried out the model presentation in a form suitable for numerical solution, and the implementation in software, allowing evaluation of unobservable processes by measured processes. The author also performed analysis of test batteries' data, and model calibration/verification against experimental data, resulting in model calibration feature in software. In addition, author carried out battery simulation in charge/discharge processes for SOC and SOH prediction. Initial ideas of UPS batteries monitoring were introduced by Teuvo Suntio. The general methodology of analysis, literature analysis for screening of model, model improvements, and many of the problem statements were formed in discussions with Robert Tenno and Teuvo Suntio. The author contributed most of the work.

[P3], and the software described there, was contributed by the author.

The lumped parameter model, optimisations to the model and the software, as well as the original idea of the battery monitoring system described in **[P4],** were author's and carried out by him. The publication was written together with Robert Tenno.

In **[P5]** and **[P8]**, the exact time-requency relation between electrochemical cell model (basic processes) and battery impedance is established in cooperation with Robert Tenno, with the author contributing most of the work. The original idea of modelling batteries at extremely low frequencies using single pulse belongs to the author. Robert Tenno extended the model to more complex processes (fast discharge and overcharge). Teuvo Suntio analysed the usability of commercially available analysers in

the light of the acquired results. Software implementation and battery frequency analysis is performed by the author.

The work in **[P7]** was shared with by Teuvo Suntio, based on the tools created and described in Publications [P5] and [P8]. Author contributed especially the experimental part and about half of the publication.

6.4. Future Work

More work should be done on testing and polishing the software implementing the models described in this dissertation. Model calibration should be fully automatic, currently it contains some parts where manual intervention is required. The models/software should also tested with more experimental data, and, if necessary, modified further to ensure robustness.

Following that, the application can be integrated into real-time battery monitoring system. Such as system can be either central, as explained in Chapter I, or distributed, where a copy of the application is running on each station (there is often plenty of spare processing power available, making this approach viable) and signals the need for replacement when such a situation comes up.

It is of great interest to convert the results of this study to other type of batteries (lithium-ion).

References

[1] Ball R.J., R. Kurian, R. Evans and R. Stevens. Study of valve-regulated lead/acid batteries manufactured with different separator papers. J. Power Sources, vol. 104, 2002, pp. 234-240.

[2] Beketaeva L. A., Rybalka K. V. and D. Simonsson. Structural changes in the active mass of the negative electrode of the lead/acid battery during charging. *J. Power Sources,* no. 32, 1990, pp. 143-150.

[3] Bernardi D. M. and M. K. Carpenter. A mathematical model of the oxygen-recombination lead-acid cell. *J. Electrochem. Soc.,* vol. 142, no. 8, 1995, pp. 2631-2642.

[4] Bernardi D. M., H. Gu and A.Y. Schoene. Two-dimensional mathematical model of a lead-acid cell. *J. Electrochem. Soc.,* vol. 140, no. 8, 1993, pp. 2250-2258.

[5] Berndt D. *Maintenance-Free Batteries.* Research Studies Press Ltd., John Wiley & Sons Inc. 1997, 496 p.

[6] Berndt D. Valve-regulated lead-acid batteries. *J. Power Sources*, vol. 95, 2001, pp. 2-12.

[7] Berndt D. Valve-regulated lead-acid batteries. *J. Power Sources*, vol. 100, 2001, pp. 29-46.

[8] Berndt D., R. Bräutigam and U. Teutsch. Temperature compensation of float voltage. The Special situation of VRLA batteries. in *Proc. IEEE INTELEC'95.* 1995, pp. 1-12.

[9] Berndt D., W.E.N Jones. Balanced float charging of VRLA batteries by Means of Catalysts. in *Proc. IEEE INTELEC'98*, 1998, pp. 443-451.

[10] Bose C. S. C. and G. W. Mathiesen. Gas Evolution, Recombination and Grid Corrosion in a VRLA Battery Under High Temperature Operating Conditions. in *Proc. IEEE INTELEC'97*, 1997, pp.13-17.

[11] Culpin B. D. and A. J. Rand. Failure modes of lead/acid batteries. *J. Power Sources*, vol. 36, no. 2, 1991, pp. 415-438.

[12] De Levie R. Electrochemical response of porous and rough electrodes. *Advances in electrochemistry and electrochemical engineering*. Wiley Interscience, vol. 6, 1967, pp. 329-397.

[13] Dimpault-Darcy E.C., T.V. Nguyen and R.E. White. A two-dimensional mathematical model of a porous lead dioxide electrode in a lead-acid cell. *J. Electrochem. Soc.,* vol. 135, no. 2, 1988, pp. 278-285.

[14] Doyle M., J.P. Meyers and J. Newmann. Computer simulations of the impedance response of lithium rechargeable batteries. *J. Electrochem. Soc.,* vol. 147, no. 1, 2000, pp. 99-110.

[15] Ekdunge P. and D. Simonsson. The discharge behaviour of the porous lead electrode in lead-acid battery. I Experimental investigation. *J. Applied Electrochemistry,* no. 19, 1989, pp. 127-135.

[16] Ekdunge P. and D. Simonsson. The discharge behaviour of the porous lead electrode in lead-acid battery. II Mathematical model. *J. Applied Electrochemistry,* no. 19, 1989, pp. 136-141.

[17] Fan D. and R. E. White. Modification of Newman`s BAND(J) Subroutine to multi-region systems containing interior boundaries: MBAND. *J. Electrochem. Soc.,* vol. 138, no. 6, 1991, pp. 1688-1691.

[18] Feder D.O., T.G. Croda, K.S. Champlin, S.J. McShane and M.J. Hlavac. Conductance testing compared to traditional methods of evaluating the capacity of valve-regulated lead/acid batteries and predicting state-of-health. *J. Power Sources*, vol. 40, 1992, pp. 235-250.

[19] Feder D. O., M. J. Hlavac and W. Koster. Evaluating the state-of-health of flooded and valve-regulated lead/acid batteries. A comparison of conductance testing with traditional methods. *J. Power Sources*, vol. 46, no. 2-3, 1993, pp. 391-415.

[20] W. Gaines, reliable energy – a view from the bottom, the user. Alternatives to the VRLA battery. in *Proc. IEEE INTELEC'02*, 2002, pp. 248-250.

[21] Gopikanth M.L. and S. Sathyanarayana. Impedance parameters and the state-of-charge. II Lead-acid battery. *J. Applied Electrochemistry,* no. 9, 1979, pp. 369-379.

[22] Gu H., T.V. Nguyen and R.E. White. A mathematical model of a lead-acid cell: Discharge, rest and charge. *J. Electrochem. Soc.,* vol. 134, no. 12, 1987, pp. 2953-2960.

[23] Gu H., C.Y.Wang and B.Y. Liaw. Numerical modeling of coupled electrochemical and transport processes in lead-acid cell. *J. Electrochem. Soc.,* vol. 144, no. 6, 1997, pp. 2053-2061.

[24] Gu W.B., G.O. Wang and C.Y. Wang. Modeling the overcharge process of VRLA batteries. in *Proc. 16th Annual Battery Conf. on Application and Advantages*. 2001, pp. 181-186.

[25] Gu W.B., G.Q. Wang and C.Y. Wang. Modelling the overcharge process of VRLA batteries. *J. Power Sources,* vol. 108, 2002, pp. 174-184.

[26] Hawkins J. M. and L.O. Barling. Some aspects of battery impedance characteristics. in *Proc. IEEE INTELEC'95*. 1995, pp. 271-276.

[27] Hawkins J. M. and R. G. Hand. AC impedance spectra of field-aged VRLA batteries. in *Proc. IEEE INTELEC'96*. 1996, pp. 640-644.

[28] Himmelblau, D. M., *Applied Nonlinear Programming*. McGraw Hill, New York, 1972.

[29] Huang H. and T.V. Ngyen. A two-dimensional transient thermal model for valve-regulated lead-acid batteries under overcharge. *J. Electrochem. Soc.,* vol. 144, no. 6, 1997, pp. 2062-2068.

[30] Huet F. A review of impedance measurements for determination of the state-of-charge or state-of-health of secondary batteries. *J. Power Sources,* no. 70, 1998, pp. 59-69.

[31] Karlsson G. Simple model for the overcharge reaction in valve regulated lead/acid batteries under fuly stationary conditions. J. Power Sources, vol. 58, 1996, pp. 79-85.

[32] Landfors J., D. Simonsson and A. Sokirko. Mathematical modelling of a lead-acid cell with immobilized electrolyte. *J. Power Sources,* vol. 55, 1995, pp. 217-230.

[33] Liaw B.Y. and K. Bethune. On Validation of the Modeling of overcharge process in VRLA cells. in *Proc. 16th Annual Battery Conf. on Application and Advantages.* 2001, pp. 187-192.

[34] Macdonald J.R. Impedance spectroscopy, emphasizing solid materials and systems. John Wiley & Sons. 1987.

[35] Newman J. and W.H. Tiedemann. Porous-electrode theory with battery applications. *AIChE J.,* no 21, 1975, pp. 25-41.

[36] Newman J. and W. Tiedemann. Simulation of recombination lead-acid batteries. *J. Electrochem. Soc.,* vol. 144, no. 9, 1997, pp. 3081-3091.

[37] Nguyen T.V., R.E. White and H. Gu. The effects of separator design on the discharge performance of a starved lead-acid cell. *J. Electrochem. Soc.,* vol. 137, no. 10, 1990, pp. 2998-3004.

[38] Noworolski Z. and U. Reskov. Can a battery ohmic tester distinguish a good cell from the pool of better ones? in *Proc. IEEE INTELEC'02,* 2002, pp. 221-226.

[39] Osaka T., S. Nakade, M. Rajamäki and T. Momma. Influence of capacity fading on commercial lithium-ion battery impedance. *J. Power Sources.* vol. 119-121, 2003, pp. 929-933.

[40] Pissanetzky S. *Sparse matrix technology.* Academic Press. 1984.

[41] Karden E. Using low-frequency impedance spectroscopy for characterization, monitoring and modeling of industrial batteries. Ph.D. Thesis. RWTH. Aachen, 2001, 137 p.

[42] Karden E., S. Buller and R.W. De Doncker. A method for measurement and interpretation of impedance spectra for industrial batteries. *J. Power Sources*, vol. 85, 2000, pp. 72-78.

[43] Karden E. and R.W. De Doncker. The non-linear low-frequency impedance of lead/acid batteries during discharge, charge and float operation. in *Proc. INTELEC'01*. 2001, pp. 65-72.

[44] Keddam M., Z. Stoynov and H. Takenouti. Impedance measurements on Pb/H_2SO_4 batteries. *J. Applied Electrochemistry,* no. 7, 1977, pp. 539-544.

[45] Keiser H., D. Beccu and M.A. Gutjahr. Abschätzung der porwnstruktur poröser elektroden aus impedanzmeeeungen. *J. Electrochimica Acta*, no. 21, 1976, pp. 539-543.

[46] Kirchev A., D. Pavlov and B. Monahov. Gas-diffusion approach to the kinetics of oxygen recombination in lead-acid batteries. J. Power Sources, vol. 113, 2003, pp. 245-254.

[47] Krein P.T. and R.S. Balog. Life extension through charge equalization of lead-acid batteries. in *Proc. IEEE INTELEC'02*. 2002, pp. 516-523.

[48] Kreyszig E. *Advanced Engineering Mathematics.* John Wiley & Sons Inc. 1999, 1156 p.

[49] Randles J.E.B. Kinetics of rapid electrode reactions. Discuss. Faraday Soc., no. 1, 1947, pp. 11-19.

[50] Robinson R.S. On-line battery testing: a reliable method for determining battery health. in *Proc. IEEE INTELEC'96*, no. 4, 1996, pp. 654-661.

[51] Rossinot E., C. Lefrou and J. P. Cun. Study of scattering of VRLA batteries characteristics and its influence for UPS applications. in *Proc. IEEE INTELEC'02.* 2002, pp. 128-133.

[52] Rossinot E., C. Lefrou and J.P. Cun. A study of the scattering of valve-egulated lead acid battery characteristics. *J. Power Sources*, no. 114, 2003, pp. 160-169.

[53] Rubinstein, R.Y., *Simulation and the Monte Carlo Methods*, John Wiley and Sons, Inc., 1981.

[54] Rybalka K.V. and L.A. Beketaeva. Impedance determination of pore-structure parameters of the active mass of lead-acid battery negatives. *J. Elektrokhimija,* no. 23., 1987, pp. 419-423.

[55] Simonsson D., P. Ekdunge and M. Lindgren. Kinetics of the porous lead electrode in the lead-acid cell. *J. Electrochem. Soc.,* vol. 135, no. 7, 1988, pp. 1614-1618.

[56] Suntio T. and A. Glad. The batteries as a principal component in DC UPS systems, in *Proc. IEEE INTELEC'90*, 1990, pp. 400-411.

[57] Suntio T., L. Jonsson and A. Kujala. Battery system reliability and availability determine UPS performance, *Power Quality Magazine*, vol. 1, no. 4, 1990, pp. 234-240.

[58] Suntio T., P. Waltari, A. Tenno and R. Tenno. The effects of intermittent charging on VRLA battery life expectancy in telecom applications. in *Proc. 24th INTELEC Conf.*, 2002, pp. 121-127.

[59] Tiedemann W. H. and J. Newman. *Battery Design and Optimization.* Editor: S. Gross. The Electrochemical Society Softbound Proceeding Series Princeton, New York. 1979, 23 p.

[60] Waltari P. and T. Suntio. Survey and evaluation of battery monitoring methods and results from user's viewpoint, in *Proc. IEEE INTELEC'99*, 1999, paper 21-2.

[61] Yin Q., G.H. Kelsall, D.J. Vaughan and N.P. Brandon. Mathematical models for time-dependent impedance of passive electrodes. J. *Electrochem. Soc.,* vol. 148, No. 3. 2001. P. A200-A208.

HELSINKI UNIVERSITY OF TECHNOLOGY CONTROL ENGINEERING LABORATORY

Editor: H. Koivo

Report 130 Pöyhönen, S., Negrea, M., Arkkio, A., Hyötyniemi, H.
Comparison of Reconstruction Schemes of Multiple SVM's Applied to Fault Classification of a Cage Induction Motor. August 2002.

Report 131 Pöyhönen, S.
Support Vector Machines in Fault Diagnostics of Electrical Motors. September 2002.

Report 132 Gadoura, I. A.
Design of Robust Controllers for Telecom Power Supplies. September 2002.

Report 133 Hyötyniemi, H.
On the Universality and Undecidability in Dynamic Systems. December 2002.

Report 134 Elmusrati, M. S., Koivo, H. N.
Radio Resource Scheduling in Wireless Communication Systems. January 2003.

Report 135 Blomqvist, E.
Security in Sensor Networks. February 2003.

Report 136 Zenger, K.
Modelling, Analysis and Controller Design of Time-Variable Flow Processes. March 2003.

Report 137 Hasu, V.
Adaptive Beamforming and Power Control in Wireless Communication Systems. August 2003.

Report 138 Haavisto, O., Hyötyniemi, H.
Simulation Tool of a Biped Walking Robot Model. March 2004.

Report 139 Halmevaara, K., Hyötyniemi, H.
Process Performance Optimization Using Iterative Regression Tuning. April 2004.

Report 140 Viitamäki, P.
Hybrid Modeling of Paper Machine Grade Changes. May 2004.

Report 141 Pöyhönen, S.
Support Vector Machine Based Classification in Condition Monitoring of Induction Motors. June 2004.

Report 142 Elmusrati, M. S.
Radio Resource Scheduling and Smart Antennas in Cellular CDMA Communication Systems. August 2004.

Report 143 Tenno, A.
Modelling and Evaluation of Valve-Regulated Lead-Acid Batteries. September 2004.

ISBN 951-22-7325-X

ISSN 0356-0872

Picaset Oy, Helsinki 2004